

**Novel Creep-resistant Ferritic Alloy Designed by the
Concept of Precipitation Hardening with Two Types of
Precipitates**

A Dissertation Presented for the

Doctor of Philosophy

Degree

The University of Tennessee, Knoxville

Shao-Yu Wang

August 2019

Copyright © 2019 by Shao-Yu Wang

All rights reserved.

ACKNOWLEDGEMENT

I'm grateful for whoever helped me in any forms within this five-year journey toward PhD degree. I would like to thank for my advisor Peter K. Liaw, and my project sponsors Department of Energy and National Science Foundation, for supporting me financially. I would like to as well grant my gratitude to my committee members Kurt E. Sickafus, Yanfei Gao, and Brett G. Compton for their comments and suggestions on my thesis, which greatly improve the completeness of this research. I would like to thank Dr. Jon Poplawsky and Dr. Ke An in Oak Ridge National Laboratory, for helping me out for the atom probe and neutron diffraction experiments. I would also like to thank for several professors in the Department of Sciences and Engineering, UTK, for their classes really inspired me for this research. Prof. T. G. Nieh's creep class provides a lot of knowledge to me for the study on the creep behavior of metals. Prof. M. Fitzsimmons's class showed me various of techniques on analyzing diffraction data. Prof. D. Keffer's class inspired me on developing a viable code for my research. All these helps I would forever keep them in my heart.

This five-year journey was extremely tough and difficult, totally changed my mindset and value on life, and permanently rebuilt me as another person. Without friends, I would never be able to go to the very end. Chanho and Peiyong were my best friends and the best comrades in the UTK, for we were in the same group and went through everything together. We had a strong comradeship between us, that even in an extremely oppressive environment, it was the very essence that keeps us fighting through. I would grant my most sincere gratitude to them, and I would cherish this relationship forever. I would also like to

thank for Peijun Hou, although he was not in the same group with me, he helped me a lot in both synchrotron experiments and life issues. Taiwanese seniors Curtis Chen and Yu-Che Hsiao, as well as juniors Sean Kuo and Hui-Chen Wang, they all helped me a lot for my life in Knoxville. I cannot express enough gratitude toward them, and they are all very welcome if they need my help in the future.

My family, especially my brother, Shao-An Wang, supported me a lot with his own experience and sincere opinions, they really helped me significantly when I was in the pit of despair. My friends in Taiwan, although we've probably only met once per year, their friendship with me always refreshes my gloomy mind. Words cannot describe how hard this experience was, cannot depict how precious these supports meant to me. I could only hope everyone, either you are mentioned here or not, helped me going through this journey, might receive whatever you wish to obtain.

ABSTRACT

Based on the concept of precipitation hardening, novel ferritic alloys FBB8 + 2 wt.% Hf, FBB8 + 2 wt.% Zr, and FBB13 + 3.5 wt.% W alloys were developed and investigated, in order to introduce additional particles for further strengthening of the current alloy FBB8. Scanning electron microscopy (SEM), atom probe tomography (APT), neutron/synchrotron diffraction were employed in order to characterize the microstructural features, combined with mechanical tests on strength, as well as creep tests, for a better understanding on the microstructure-mechanical properties connection. The results show that although these alloys possess two or more kinds of precipitates, the major strengthener is still B2-NiAl. Other types of particles either have too low volume fraction, or are too large to provide sufficient strengthening. Results reveal that volume fraction of secondary phases is proportional to the particle size, if the volume fraction of certain phase goes higher, its particle size goes larger as well. Therefore, in order to optimize the strengthening effect, the amount of the additive elements is needed to be carefully adjusted, in order to reach a balance between volume fraction and particle size. The calculation for the strength of the alloys supports the microstructural discoveries from the FBB8 + 2 wt.% Hf, FBB8 + 2 wt.% Zr, and FBB13 + 3.5 wt.% W alloys, where the FBB13 + 3.5 wt.% W alloy has the worst strength among these three alloys, majorly due to low volume fraction of particles and smaller particle size. Minor discrepancies between the experimental data and the calculation might be due to inaccurate measurement on the microstructural parameters. The creep results as well as the modeling for the FBB13 + 3.5 wt.% W alloy shows that the extremely small B2-NiAl precipitate leads to the major discrepancy between the experimental data and the modeling results, where the actual creep rate

is much faster than the modeling results. Such discrepancy lies on the fact of utilizing the wrong strengthening mechanism for the back stress calculation, and a better equation that scales with creep strain is required to reflect the actual back stress contributed from the small, coherent precipitates.

TABLE OF CONTENTS

Chapter One Introduction	1
High-Temperature Materials.....	1
Metals.....	1
Ceramics	2
Composites.....	3
Strengthening Mechanisms at High Temperatures.....	4
Precipitation Strengthening.....	5
Solid Solution Strengthening	10
Factors to be Concerned.....	12
Chapter Two Literature Review and Alloy Design	14
Current Progress and Problems.....	14
Alloy Design	21
FBB8 + Hf alloy	23
FBB8 + Zr alloy	31
FBB13 + W alloy.....	36
Brief Summary on the Prediction of Precipitations	39
Chapter Three Materials and Methods.....	43
Microstructural Characterizations.....	45
Scanning Electron Microscopy (SEM).....	45
Neutron/Synchrotron Diffraction.....	46
Atom Probe Tomography (APT)	46

Mechanical Tests	47
Tension/Compression Tests	47
Creep Tests.....	48
Numerical Calculations.....	48
Yield Strength	49
Creep Model.....	58
Chapter Four Microstructure.....	65
Scanning Electron Microscopy (SEM)	65
Atom Probe Tomography (APT)	70
Neutron/Synchrotron Diffraction.....	75
Discussion on Microstructures.....	82
Chapter Five Strength Tests and Calculations	90
Compression Tests at Room Temperature	90
Tension Tests at 700 °C	92
Calculation for Strength.....	94
Discussion on Strength	97
Chapter Six Creep Tests and Calculations.....	98
Tensile Creep Tests at 700 °C.....	98
Modeling for Creep.....	102
Discussion on Creep	115
Chapter Seven Conclusions and Recommendations.....	117

List of References	120
Appendix.....	131
Vita.....	150

LIST OF TABLES

Table 1. The nominal compositions of the FBB8 + Hf, FBB8 + Zr, and FBB8 + W alloys in weight percent (in atomic percent).	27
Table 2. Predicted precipitations for the proposed alloy systems, and other possible phases.....	42
Table 3. Nomenclatures for the parameters served in the equations in this research	44
Table 4. General parameters for creep calculations.....	64
Table 5. Diamters and volume fractions for particles observed using SEM technique.....	68
Table 6. Elemental distributions on each phases within FBB8 + 2 wt.% Hf and FBB8 + 2 wt.% Zr alloys.....	73
Table 7. Phases characterized from the fitting of diffraction patterns and their respective lattice constants and volume fractions.....	81
Table 8. Microstructural parameters combined with both SEM and diffraction analysis	89
Table 9. Mechanical properties obtained from the 700 °C tension tests.....	92
Table 10. Contributions of different mechanisms in strength increment.....	96
Table 11. Applied stress and the corresponding creep rate for FBB13 + 3.5 wt.% W alloy creep at 700 °C	102
Table 12. Parameters and their values for FBB13 + 3.5 wt.% W alloy.....	139

LIST OF FIGURES

- Figure 1. A schematic illustrated the concept of precipitation hardening. At certain composition and temperature, there is only single phase exists, cooling down from the single phase regimes yields in precipitation of secondary phase particles..... 6
- Figure 2. A schematic for a general heat-treatment on precipitation hardening materials. Solution process helps in dissolving solutes into the solvent with single phase, and then quench to maintain the microstructure. In the aging process the secondary phase particles start to precipitate out and impede the dislocations from movement. 7
- Figure 3. A schematic for the strengthening effect on precipitation hardening mechanisms. There is a critical particles size for optimization of the strength, usually the size is around 20-50 nm. 9
- Figure 4. A schematic on (a) types of solid solution, and (b) the solute atom's location affects to the dislocation movement. Since solute atom tend to locate in a relatively wide space, usually dislocation is a proper spot for them, therefore when dislocation moves, the solute atoms move as well, increases dislocation's difficulties on moving. 11
- Figure 5. The creep resistance of FBB8 + 2 wt. % Ti (hierarchical structure B2 + L₂₁ precipitate) and FBB8 + 4 wt. % Ti (L₂₁ phase precipitate) alloys in comparison with FBB8, P92, and P122 [11]. 17
- Figure 6. A schematic on the concept of the proposed research. By adding additional element into the FBB8 system, it is possible to form a different secondary phase other than existing B2 phase, and increase the total volume fraction of the particles. 20

Figure 7. A flow-chart for the proposed research, starts with the alloy design based on the phase diagrams, and then followed with microstructural characterization and mechanical tests, in order to obtain necessary parameters and properties. In the end, all these numbers will be deployed for the modification and verification of the numerical equations. 22

Figure 8. The Hf-Fe binary phase diagram [25]. As shown in the very left side, the solubility of Hf within Fe is really limited. 25

Figure 9. A well-dispersed Fe₂Hf precipitate within Fe-9Cr matrix [27]. The size of the Fe₂Hf precipitates is roughly 20 - 50 nm, indicating that these particles can be a very strong strengthener for the precipitation hardening mechanism..... 26

Figure 10. Hf-Ni binary phase diagram [28]. For the composition shown in Table 1, there is ~ 17 wt. % Hf within Ni, indicating there will be a eutectic reaction forming Ni₅Hf intermetallic compound. 28

Figure 11. Hf-Al binary phase diagram [28]. For the composition shown in Table 1, there is ~ 25 wt. % Hf within Al, indicating there will be a eutectic reaction forming Al₃Hf intermetallic compound. 29

Figure 12. Hf-Ni-Al ternary phase diagram at 800 °C [28]. Based on the respective atomic ratio of the Hf, Ni, and Al within the alloy system, in the ternary phase diagram, there will be B2-NiAl and α -Ni₃Hf presented. 30

Figure 13. Zr-Fe binary phase diagram [25]. Compared with the Hf-Fe phase diagram shown in Figure 8, the solubility of Zr within Fe is even more limited, suggesting that homogeneously dispersed secondary phases formed with Fe and Zr might not present.32

Figure 14. Zr-Ni binary phase diagram [30]. For the composition shown in Table 1, there is ~ 17 wt. % Zr within Ni, indicating there will be a eutectic reaction forming Ni₅Zr intermetallic compound. 33

Figure 15. Zr-Al binary phase diagram [30]. For the composition shown in Table 1, there is ~ 25 wt. % Zr within Al, indicating there will be a eutectic reaction forming Al₃Zr intermetallic compound. 34

Figure 16. Zr-Ni-Al ternary phase diagram at 800 °C [30]. Based on the respective atomic ratio of the Zr, Ni, and Al within the alloy system, in the ternary phase diagram, there will be Al₃Ni₂ and Al₂Ni_{1.2}Zr_{0.8} presented..... 35

Figure 17. Calphad calculation for the specific composition Fe-6.5Al-10Cr-10Ni-2Zr-3.4Mo-0.025B (wt. %). In the Calphad prediction at 700 °C, there is ~ 8% of C14-Fe₂Zr presented in the alloy system, and ~ 50% FCC phase (should be Fe for such high fraction) present. These predictions do not agree with what are shown in the phase diagrams. 38

Figure 18. W-Fe binary phase diagram [25]. W has ~ 3.7 at. % (~10 wt.%) solubility in Fe at temperature high than 1060 °C, and drops to ~ 1.3 at. % at 800 °C, making it an ideal candidate for precipitation hardening. The precipitation could be λ-Fe₂W, which is a MnZn₂ type Laves phase (C14) crystal structure. 41

Figure 19. The sample geometry for tensile samples, including samples for creep tests 44

Figure 20. The sample geometry for compression test samples. 44

Figure 21. A schematic on the assumption of an alloy system composed of two different kinds of particles, where it assumes that both particles are both spherical, and each of them has their respective numbers, sizes, and volume fractions. 53

Figure 22. A schematic on the particle sizes between (a) without a distribution, where same type of particles has the same size, and (b) with a distribution, where two different types of particles have various of sizes and corresponding volume fraction. 56

Figure 23. SEM images for a general and detailed view of the microstructure of (a) (d) FBB8 + 2 wt.% Hf, (b) (e) FBB8 + 2 wt.% Zr, and (c) (f) FBB13 + 3.5 wt.% W alloys. Three distinct areas can be identified within the microstructures, which are the matrix, the B2 phase particles, and white agglomerates. 67

Figure 24. A closer view on the white agglomerate on FBB8 + 2 wt.% Zr exposes that the white agglomerate is composed of numerous white particles. 69

Figure 25. APT measurements on the different areas within FBB8 + 2 wt.% Hf, FBB8 + 2 wt.% Zr, and FBB13 + 3.5 wt.% W alloys. The areas are identified and selected under SEM, and later prepared into APT samples by FIB. For FBB13 + 3.5 wt.% W alloy, one can notice that there's many tiny B2 phase particles distributed within the matrix, which are ~5 nm in diameter. 72

Figure 26. The neutron diffraction pattern for FBB8 + 2 wt.% Hf and FBB8 + 2 wt.% Zr at room temperature, where (a) the whole diffraction pattern, (b) the diffraction pattern from the 2θ of 15.2° to 16.6° , (c) the diffraction pattern from the 2θ of 19.4° to 23.6° , and (d) the diffraction pattern from the 2θ of 24° to 33° . The dashed line is the actual data collected

from the diffraction experiment, and the solid line is the fitting. Major peaks with high intensities are overlap of the BCC and B2 peaks, which are the matrix (α -Fe) and the major strengtheners (B2-NiAl) of the alloys. Minor peaks are identified and labeled for the crystal structure of the white agglomerates in the alloys, which are C15-Ni₂Hf, HCP-Hf, and C14-Fe₂Hf in the FBB8 + 2 wt.% Hf alloy, and D8₄-Fe₂₃Zr₆ and HCP-Zr in the FBB8 + 2 wt.% Zr alloy. 77

Figure 27. The synchrotron XRD pattern of FBB13 + 3.5 wt.% W alloy. Due to transmission measurement setup the 2θ range is only to $\sim 8^\circ$, however it is already enough for phase characterization. The major phases that can be identified are α -Fe, B2-NiAl, C14-Fe₂W, and C14-Fe₂Mo..... 80

Figure 28. Schematic illustrating the formation of the microstructure of the FBB8 + 2 wt.% Hf and FBB8 + 2 wt.% Zr alloys. Since the majority of the Hf, Zr, and their respective intermetallic compounds are insoluble within the α -Fe matrix. During the solidification of the matrix these insoluble clusters are deposited at grain boundaries, and/or enveloped within grains as a large agglomerate. 86

Figure 29. The compression test for FBB8 + 2 wt.% Hf, FBB8 + 2 wt.% Zr, and FBB13 + 3.5 wt.% W alloys, performed at room temperature. The FBB13 + 3.5 wt.% W alloy has relatively lower yield strength compared to the other two alloys, but slightly better ductility. Surprisingly, FBB8 + 2 wt.% Hf alloy has lower yield strength than the FBB8 + 2 wt.% Zr alloy. 91

Figure 30. The tensile test for FBB8 + 2 wt.% Hf and FBB13 + 3.5 wt.% W alloys, performed at 700 °C. The FBB13 + 3.5 wt.% W alloy has relatively lower yield strength compared to FBB8 + 2 wt.% Hf alloy, but much greater elongation (or ductility) at 700 °C..... 93

Figure 31. Creep curve for FBB13 + 3.5 wt.% W alloy, tested with applied stress 70 MPa, at 700 °C. The creep curve shows clear three creep stages, takes roughly 1000 seconds to steady-state, and another 5000 seconds to the third stage of creep where the creep rate starts to increase over time. 99

Figure 32. The creep curve for creep jump test on FBB13 + 3.5 wt.% W alloy, tested with applied stress 30 MPa, 37 MPa, and 50 MPa at 700 °C. 100

Figure 33. The plot of $\ln \varepsilon$ vs. $\ln(\sigma - \sigma_{th})$, where the $n = 4$ is assigned for the fitting of the threshold stress σ_{th} . The σ_{th} is 16.38 MPa. The point of 30 MPa is actually not follow well with neither the fitting line nor the straight line formed by the other three data points, indicating another creep mechanism might be dominating the creep at 30 MPa. 101

Figure 34. The comparison between the creep curve for FBB13 + 3.5 wt.% W alloy, tested with applied stress 70 MPa at 700 °C, with the prediction from the model. Due to the nano-sized B2-NiAl precipitates, the inter-particle spacing is extremely small, largely slowing down the creep rate. 103

Figure 35. The comparison between the creep rate for FBB13 + 3.5 wt.% W alloy, tested with applied stress 70 MPa at 700 °C, with the prediction from the model. The prediction on the primary stage (the first 5 minutes where the creep rate hasn't drop to the lowest point)

is roughly 2 times slower than the experimental data, which is due to the extremely small inter-particle spacing. 106

Figure 36. The three stresses related to the dislocation-precipitate interaction in the calculation of the creep. For the creep test at 70 MPa, the effective stress is always higher than the sum of the rest of two stresses, therefore the dislocation-precipitate mechanism has always activated during the whole creep process. Back stresses for precipitates contribute depending on their respective volume fraction, where B2-NiAl contribute the most amount three kinds of particles. 107

Figure 37. The respective creep rate components for all 4 creep tests on (a) 70 MPa, (b) 50 MPa, (c) 37 MPa, and (d) 30 MPa. The dislocation component keeps dropping until 37 MPa, it suddenly disappeared, majorly due to the effective stress starts to be lower than the sum of back stresses and dislocation stress. At 30 MPa this same situation happens much faster than at 37 MPa. 110

Figure 38. The coarsening of both B2 phase precipitate and Laves phase precipitate, where the Laves phase precipitate coarsening kinetic parameters are estimated. The coarsening B2-NiAl is much faster Laves phase precipitate, where within 250 mins, the size doubles. 111

Figure 39. The comparison between the experimental data and calculated data for both four applied stresses. The data points at 30 MPa fits the most, majorly due to at 30 MPa, almost the whole creep process is dominated by diffusional creep, but this diffusional creep rate

cannot be doubled when the applied stress goes to 37 MPa. Data point at 50 MPa also fit relatively well, but at 70 MPa the discrepancy on creep rate is roughly 2 times. 114

Figure 40. Flow chart of the constitutive creep model. 138

CHAPTER ONE

INTRODUCTION

High-Temperature Materials

Followed by the development of human civilization, the demand on better material grows higher and higher, and after the Industrial Revolution, materials that can be served at high temperature becomes the key component of development, for the applications of engine, power generation, military...etc., all require materials that can be served at higher temperature, and even with higher strength or other mechanical properties, because it equals to higher efficiency. Nowadays, the high-temperature materials can be generally categorized as three different categories, which are (1) metals, (2) ceramics, and (3) composites (mostly carbon composites), and among them, metals are still the most widely applied material for high-temperature applications, due to its great workability, and cost efficiency.

Metals

Metals or alloys are formed by metallic bond, which is the bonding that has the least limitations. Unlike covalent bond and ionic bond, metallic bond does not care about directionality and electric neutrality. This feature makes metals easily deformed without fractured, significantly improves metallic materials' service life. The major drawback of metallic materials in high temperature application is that metals cannot sustain under very high temperature, compared to ceramics and composites. At high temperature, mobility of dislocations becomes high and for metals it quickly loses its strength. Therefore, lots of researches focus on improving the high-temperature

mechanical properties of metallic materials, ex: creep resistance, phase stability...etc., in order to further improve the performance of metals at higher temperatures. In modern society the most widely applied metal materials at high temperature are aluminum alloys, steels, and nickel alloys, and each of them has their unique feature [1-3]. Aluminum alloys are light and ductile, they can be the major component for the aircraft construction material, however most of aluminum alloys cannot work over 350 °C, due to the low melting point of aluminum [52]. Steels are the most studied and common material in modern world, therefore, its strength is cost efficient. Steels or ferritic alloys can work at around 650 °C with great mechanical properties [53]. Nickel alloys, or nickel-based superalloys are the best metal material working at high temperature. Nickel alloys nowadays can work over 700 °C, with good thermal stability and proper workability, it becomes the primary material for building jet engine parts [54]. Though it has the best performance, nickel alloys are expensive, which greatly limits its applications.

Almost all these high temperature metal materials are strengthened by the precipitation strengthening mechanism, which will be further addressed on the next sub-chapter Strengthening Mechanism at High Temperature.

Ceramics

Ceramics are a type of materials that possesses very high strength and high temperature durability. Most of ceramic materials are composed of ionic bonds (some of them are covalent bonds), and while plastic deformation occurred, dislocations are difficult to move since after dislocation moves, atoms need to maintain the local electric neutrality, which for ceramic materials, requires only limited slip planes, as well as a great distance to move. Therefore, most of ceramic materials are

strong, but brittle, because they lack of enough slip planes and take high energy for plastic deformation. Due to the above feature, the major drawback of ceramic materials is low workability. Ceramic materials cannot be machined into complicated shapes as metals do. Also, lack of plastic deformation capability leads to relatively low service life, that cavities and defects easily formed and propagate and soon cause the whole material fractured. In summary, the best working environment for ceramic materials is with low stress (so it hardly deformed) and high temperature. Therefore, except for applications under extremely high temperature that metals cannot sustain their performance, ceramic materials are rarely the choice of the material, because many of the parts made for high temperature applications are moving parts (ex: engine parts), which are constantly under certain stresses.

Many of the ceramic materials have been commercialized and widely applied in modern world, such as oxides (Al_2O_3 , MgO , Y_2O_3), silicon carbide (SiC), and silicon nitride (Si_3N_4) [1-3]. Oxides like Al_2O_3 can be cost efficient and heat resistant for purely high-temperature applications without stress, such as liner of furnaces. Silicon carbide has outstanding hardness and low coefficient of thermal expansion, make it great material for many applications, such as: abrasive and cutting tools, automobile parts, heating elements...etc. Silicon nitride, unlike the previous ceramic materials, has better fracture toughness, make it a better ceramic materials working under stress. Its applications include: automobile engine parts, bearings, abrasive and cutting tools...etc.

Composites

Composites are a type of material that composed of two or more types of materials (metal, ceramic, polymer...etc.), usually have respective advantages from their constituent materials. In high

temperature applications, usually the composites are made of carbon. Due to its outstanding heat resistance, carbon (graphite) or carbon composites had long utilized as refractory materials, such as inner chamber of furnace. [1-3] The major disadvantage of composites for high temperature applications is its relatively high cost. Most of the composites are made of complicated fabrication process, such as fibre placements, moulding, and sometimes post processing. Therefore, in modern world, composite materials are usually only employed in critical parts, such as rocket nozzles, in order to reduce the overall cost for products.

Strengthening Mechanisms at High Temperatures

Plastic deformation is a deformation occurred by the movement of the embedded dislocation within the material. Therefore, in order to enhance the strength of the material, the goal is to stop dislocation from moving easily. Generally, there are 4 primary strengthening mechanisms for metals, which are (1) work-hardening, (2) grain-boundary strengthening, (3) solid-solution strengthening, and (4) precipitation strengthening [4]. For high-temperature applications however, only precipitation strengthening and solid-solution strengthening serve well for their purposes. For work-hardening at high temperature, dislocations are annealed (thus the dislocation density drops) and no longer able to serve as a dislocation movement/formation obstacle. For grain-boundary strengthening, instead of being a barrier for dislocation movement, the grain boundaries can be a better slip plane for plastic deformation at high temperature. Therefore, usually in the development of high-strength high-temperature materials, the major strengthening mechanisms are the precipitation strengthening and solid-solution strengthening, and in most cases these two

strengthening mechanisms are utilized at the same time. In the following paragraphs these two mechanisms will be discussed respectively.

Precipitation Strengthening

Precipitation strengthening (a.k.a. age hardening, particle hardening, and dispersion strengthening) is a major strengthening mechanism for high temperature applications, due to its feature of increasing strength over time during the service at high temperature [5]. The general idea is via introducing precipitates within the material, these precipitates serve as an obstacle for the movement of dislocation. The concept of making precipitation strengthen materials is via proper heat treatment conditions on a solid-solution. Figure 1 shows a schematic to illustrate how the solubility affects the precipitation hardening. Usually for a binary system, there is a certain amount of solubility on the A element dissolved within the B matrix, especially at high temperatures, the solubility becomes higher. Therefore, with proper composition, at certain high temperature every A element dissolves within the B matrix and there is only one phase exists. When the temperature drops down to lower temperatures, apparently the solubility of A in B is not high enough to dissolve every A element, and the A element tries to precipitate out and make intermetallic phases. The intermetallic phases formed in this way usually homogeneously distributed within the matrix with a tiny size. Kinetic-wisely, this process needs to occur above certain temperature, so the formation and coarsening rate is high enough for the precipitates. Figure 2 shows a typical heat-treatment profile on a precipitation strengthen materials. After fabricating the material, the material has to go through a solution process, in order to dissolve every solute within the solvent and make the whole material single phase. Afterward, the material goes through an aging process, to let the

secondary phase precipitates out from the original phase. If the temperature and duration are well adjusted, the material is able to form homogeneously distributed precipitates (or particles) with proper size (usually around 50 nm), and the strength of the material is optimized.

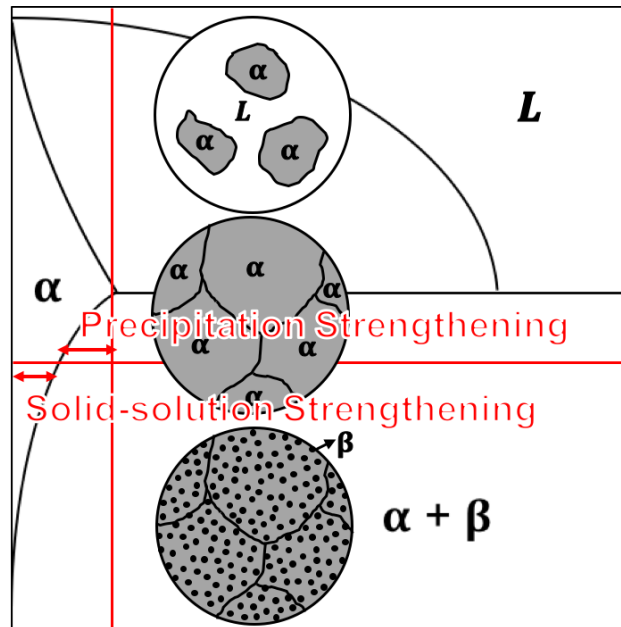


Figure 1. A schematic illustrated the concept of precipitation hardening. At certain composition and temperature, there is only single phase exists, cooling down from the single phase regimes yields in precipitation of secondary phase particles.

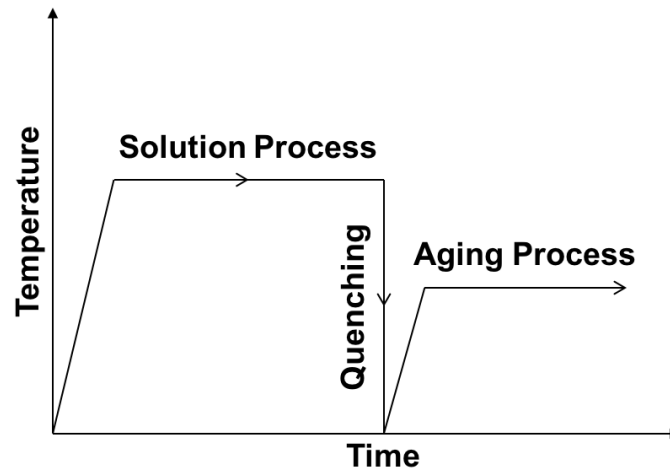


Figure 2. A schematic for a general heat-treatment on precipitation hardening materials. Solution process helps in dissolving solutes into the solvent with single phase, and then quench to maintain the microstructure. In the aging process the secondary phase particles start to precipitate out and impede the dislocations from movement.

For the strength of a precipitation strengthened materials, depends on the coherency of the precipitates, there are two major equations (Eq. (1) and Eq. (2)) describing the strengthening mechanisms of precipitation hardening, which are dislocation-shearing and dislocation-climbing [5, 6]. Their strengthening vs. particle size is shown as a schematic in Figure 3.

$$\Delta\sigma_{shear} = \frac{2\pi}{b} \left(\frac{r}{L}\right) \gamma_s = \frac{2\pi}{b} \left(\frac{3f_v}{4\pi}\right)^{\frac{1}{3}} \gamma_s \quad (1)$$

$$\Delta\sigma_{climb} = \frac{Gb}{L - 2r} = \frac{Gb}{r \left[\left(\frac{3f_v}{2\pi}\right)^{\frac{-1}{3}} - 2 \right]} \quad (2)$$

where r is the radius of the precipitate (particle), L is the spacing between precipitates (particles), b is burger's vector of the matrix material, G is the shear modulus of the matrix material, f_v is the volume fraction of the precipitate, and γ_s is the surface energy. From the above equations, it is clear that the effect of the precipitation strengthening majorly depends on the particle size and the particle volume fraction. Notably, there's no crystal structure dependence on the strengthening equations, indicating that as long as there are secondary phase particles exist in the microstructure, there is reinforcement. Among both factors of the strengthening (size and volume fraction), usually the particle size is not a parameter we can fully control, since no matter what during the service at high temperature, the particles inevitably coarsen. On the other hand, the volume fraction of the secondary phase particles is a factor that we can modified by alloy design. Since there is no crystal structure dependence in the equations, it doesn't matter that how many different phases exist as particles. Therefore, introducing as many particles as possible is a reasonable approach on alloy design for better strength.

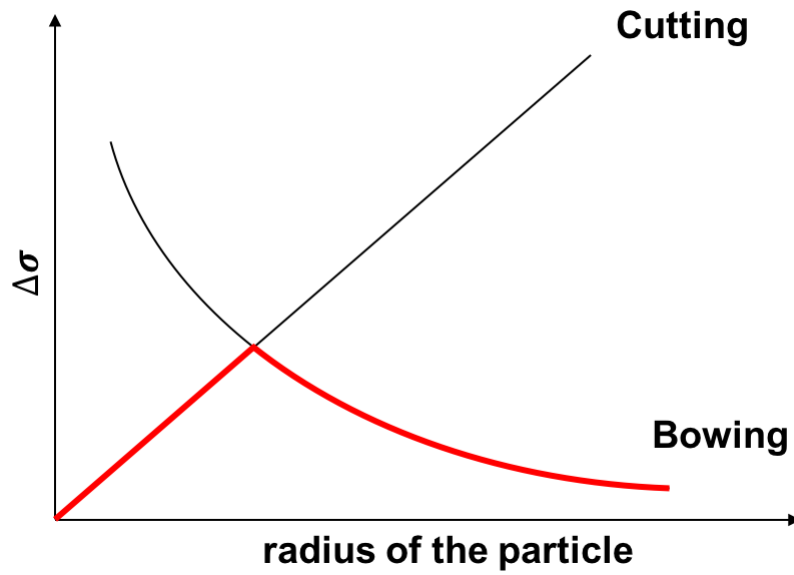


Figure 3. A schematic for the strengthening effect on precipitation hardening mechanisms. There is a critical particles size for optimization of the strength, usually the size is around 20-50 nm.

Solid Solution Strengthening

As described in Figure 1, at high temperature most of alloys are strengthened by solid-solution strengthening mechanism more or less, due to a higher solubility at elevated temperatures. Therefore, solid-solution strengthening is a strengthening mechanism that almost always play a role. Solid-solution strengthening majorly caused by lattice distortion, since usually solute atoms differ in atomic radius than the solvent atoms, when forming a single phase, the solute atoms might either occupy a lattice site or sit within the interstice, depend on the solute atomic radius. Figure 4(a) demonstrate a schematic illustrating the how solute atoms affect the original lattice in a solid solution, and as it depicts, in both ways the original lattice distorts, additional effort for a dislocation to move over is required. Figure 4(b) demonstrates how solute atoms impede the dislocation movement. Since dislocation creates a relatively wide space within the lattice, usually solute atoms tend to segregate beneath the dislocation, and while the dislocation moves, solute atoms sit beneath the dislocation follow. Rearranging local atoms in order to move the dislocation, combined with relocation of the solute atoms, are the basis of the solid-solution strengthening.

Eq. (3) is a general governing equation describes the solid-solution strengthening:

$$\Delta\sigma = Gb \left(\frac{\Delta a}{a\Delta c} - \beta \frac{\Delta G}{G\Delta c} \right)^{\frac{3}{2}} \sqrt{c} \quad (3)$$

Where G is shear modulus, a is lattice parameter, c is the concentration of the solute, and β is a constant depends on the solute atoms. The term $\frac{\Delta a}{a\Delta c}$ depicts the lattice distortion, and $\frac{\Delta G}{G\Delta c}$ depicts the modulus distortion, where the difference between the modulus of the solute and solvent also

contribute to the strength of a solid-solution strengthened material. Generally, the difference of the atomic radius and shear modulus contribute significantly to the enhancement of strength, but once

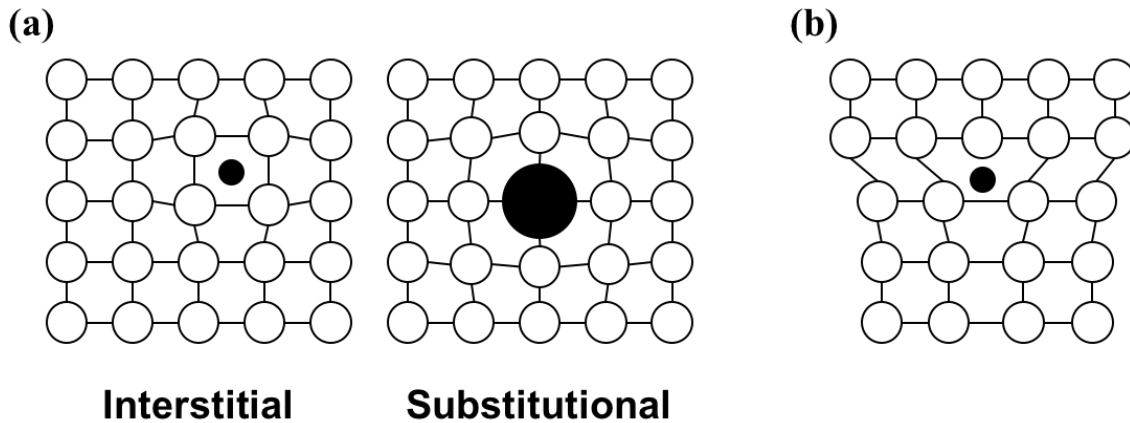


Figure 4. A schematic on (a) types of solid solution, and (b) the solute atom's location affects to the dislocation movement. Since solute atoms tend to locate in a relatively wide space, usually dislocation is a proper spot for them, therefore when dislocation moves, the solute atoms move as well, increases dislocation's difficulties on moving.

the solute species is determined, those two terms are pretty much constants. Therefore, the concentration of the solute plays a more important role in the solid-solution strengthening, since it is an adjustable parameter for engineers.

Factors to be Concerned

Three major factors to be concerned for developing high temperature materials are listed here, which are (1) cost, (2) ductility, and (3) strength. Among them, ductility and strength are actually a trade-off, usually materials with great ductility lack of strength, or vice versa. Toughness is a factor that summarizes both ductility and strength, providing a better index for the evaluation on material's durability.

First of all, cost of a material drastically affects its popularity of application. As described in previous paragraphs, among metal materials, Ni-based superalloy has the best overall mechanical properties for high temperature applications. However, its price is about 10 times of conventional steels [55, 56], making its application only limited on parts of turbine engines (especially for aircraft). Therefore, the cost is a major concern on the development of materials. Among all the current superalloys, Fe-based superalloys are by far the most cost-efficient, due to the lower price of its matrix, iron. In some aspect of properties, the Fe-based superalloys are having similar performance as Ni-based superalloys, making it an appealing alternative.

Ductility means the capability on material plastically deforms before fractured. It might be similar as the definition of toughness, but ductility refers to the percent elongation or cross-section reduction, in other words, the change in the material dimension. Toughness on the other hand refers to energy absorbed during the deformation. A ductile material does not necessarily to have good

toughness, therefore these two terms are not identical. In practical applications, ductility refers to how easily a material can be processed into the desirable shapes, which sometimes brings economic advantages to users, since a ductile material can be directly formed into specific shapes but non-ductile materials such as ceramics usually require specific molds for specific shape without building molds or losing additional materials.

Strength on the other hand is probably the most concerned property of a material, almost every application requires certain strength criterion as well as other requirements. Usually a high strength material can be obtained from making the microstructure complicated, such as introducing more dislocations, more grain boundaries, more particles...etc. Strength and ductility for most of the materials are a trade-off, where you have higher strength, you lose the ductility. Therefore, for optimization of a material, a perfect balance between strength and ductility is necessary.

Overall, it is desirable to develop a material with low cost, good ductility at room temperature, and great strength at high temperature. In this research, the ferritic alloy FBB8 has been chosen as a foundation of such development, due to its much lower cost and great creep resistance at high temperature. However, FBB8 has its drawback on poor room temperature ductility and toughness, as well as lack of enough strength at temperature over 700 °C. The goal of this research is trying to improve the above disadvantages of FBB8, by adding additional elements into the alloy system, in order to manipulate its microstructure.

CHAPTER TWO

LITERATURE REVIEW AND ALLOY DESIGN

Current Progress and Problems

In order to reach the balance of the cost and the mechanical performance, ferritic alloys of FBB8 series had been developed. FBB8 is a ferritic alloy that is composed of the body center cubic (BCC, α phase) matrix and B2 phase precipitates [7-10, 58-67]. These B2 phase precipitates are tiny (~100 nm), coherent, and homogeneously dispersed into the BCC matrix, with a volume fraction of ~16 - 18%. The microstructure of FBB8 ensures its high temperature performance. In the creep tests at 700 °C, FBB8 had found its threshold stress as 46 MPa [57], which has surpassed the working condition of a supercritical fossil energy power plant (above 600 °C, 28 MPa). The major disadvantages for FBB8 is (1) the insufficient strength at higher working temperatures, such as 760 °C, for ultra-supercritical boilers, and (2) poor room-temperature formability. Therefore, for the improvement of the high temperature strength, Song *et al.* [11-15] found that with an addition of Ti into the FBB8 alloy system, the B2-phase NiAl precipitates are combined with Ti and converts into a Heusler phase of Ni₂TiAl (L2₁ phase), which has a capability of further improving the creep resistance of the alloy. His research exposes that when FBB8 is added with more than 4 wt.% Ti, all B2 phase precipitates convert into the L2₁ phase. However, when FBB8 is added with only 2 wt.% Ti, it forms precipitates that are composed of both the B2 phase of NiAl and L2₁ phase of Ni₂TiAl, which is also called hierarchical structure precipitates. At 700 °C, FBB8 + 2% Ti has threshold stress of 186 MPa, which is much higher than the original FBB8. Song *et al.* compared the creep resistance between FBB8 + 2% Ti (strengthened by hierarchical-structure precipitates)

and FBB8 + 4% Ti (strengthened by only L₂₁ phase precipitates), and the alloy that is strengthened by hierarchical-structure precipitates apparently has better creep resistance. Figure 5 shows the outstanding creep resistance for both the FBB8 + 2% Ti and FBB8 + 4% Ti alloys, compared with commercial alloys [11]. Continued with Song's discovery, Baik *et al.* conducted a more detailed research on the FBB8 + Ti alloy system [16], and found that the FBB8 + 3.5 wt.% Ti with optimal creep resistance and hardness at 700 °C. He concluded that the greater the incoherency between the matrix and the precipitates, the higher yield strength the alloy will have. Therefore, by manipulating the coherency between the precipitates and the matrix, ideal mechanical properties (especially strength) can be achieved, and the hierarchical structure precipitates possess the key to implement such manipulations. The trick to enhance the incoherency of the precipitates and the matrix is to adjust the ratio of L₂₁ and B2 phases within one particle. The more the L₂₁ phase is present within a particle, the more incoherent the particle is to the matrix. Therefore, the higher strength and creep resistance can be achieved.

Following the current understanding on the FBB8 + Ti alloys, adding elements that have larger atomic sizes than Ti, in order to create the L₂₁ phase that more mismatched with the matrix, could lead to an even higher strength. Jung *et al.* [17, 18] published the research related to the solubility of Hf and Zr into B2-TiNi and L₂₁-Ni₂TiAl, and considered that Hf and Zr, because of larger atomic radii, have the potential of lowering the lattice misfit between the B2 and L₂₁ phases, and therefore enhancing mechanical properties. He claims that Hf and Zr are able to substitute Ti in both B2 and L₂₁ unit cells. Some research on the NiAl–Cr(Mo) eutectic alloy with Hf also shows that the Heusler phase Ni₂HfAl can be formed and coexist with the B2-NiAl precipitate [19-21].

In the above research, the Heusler phase forms mainly on the interfaces and grain boundaries of NiAl, and only a limited amount of the Ni₂HfAl precipitated within the Cr(Mo) phase. These

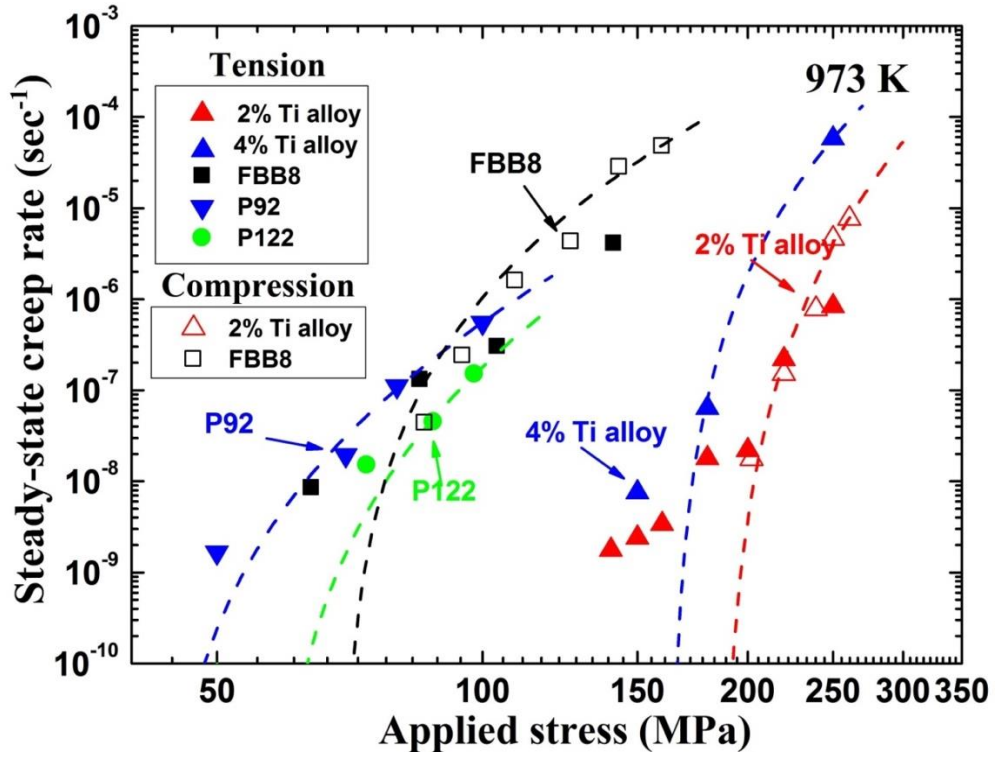


Figure 5. The creep resistance of FBB8 + 2 wt. % Ti (hierarchical structure B2 + L₂₁ precipitate) and FBB8 + 4 wt. % Ti (L₂₁ phase precipitate) alloys in comparison with FBB8, P92, and P122 [11].

observations strengthen the feasibility of the concept of replacing Ti with Hf/Zr in order to further improve the high-temperature strength of the alloy. However, recent research has shown that the addition of Hf into a FBB8 + 1.5 wt.% Ti alloy does not help in enhancing the incoherency of the precipitates and the matrix. Instead, the Hf addition tends to accumulate at grain boundaries, rather than dissolved within the matrix or within existing B2 phase particles [22].

In order to further improve the mechanical properties, nowadays novel Ni-based superalloys had tried to introduce more secondary phases within the microstructure, forming phases like γ'' phase (a body center tetragonal phase Ni_3Nb), carbides (M_7C_3 , M_6C , and M_{23}C_6), or even notorious σ phase that is brittle and reduce the strength of the materials. By this approach the overall volume fraction of the particles can be improved and the strength can be further enhanced [23].

For this research, the approach on improving the creep resistance is increasing the volume fraction of the precipitates, therefore, the goal is introducing another secondary phase other than B2 phase into the alloy system, and these two secondary phases should be separated and both homogeneously distributed within the matrix, as shown in the schematic Figure 6. Sun *et al.* demonstrated a successful practice on the maraging steel strengthened by both B2-NiAl and Laves phase $\text{Fe}_2(\text{Mo}, \text{W})$ precipitates, and significant mechanical properties had achieved, with yield strength of 1,800 MPa, ultimate tensile strength (UTS) over 2,000 MPa, creep rupture life > 2000 hours under 700 MPa at 500 °C, and the most surprised, ductility ~8% [24]. This research showed a great example that such precipitation hardening approach is achievable, although the mechanical property-wisely, it depends not only on the particles within the microstructure, but also the crystal

structure of the matrix (which is martensite) and additive solute elements (~10 at. % of Co in their alloy system, which is not presented in our alloy system). Therefore, with much confidence on the

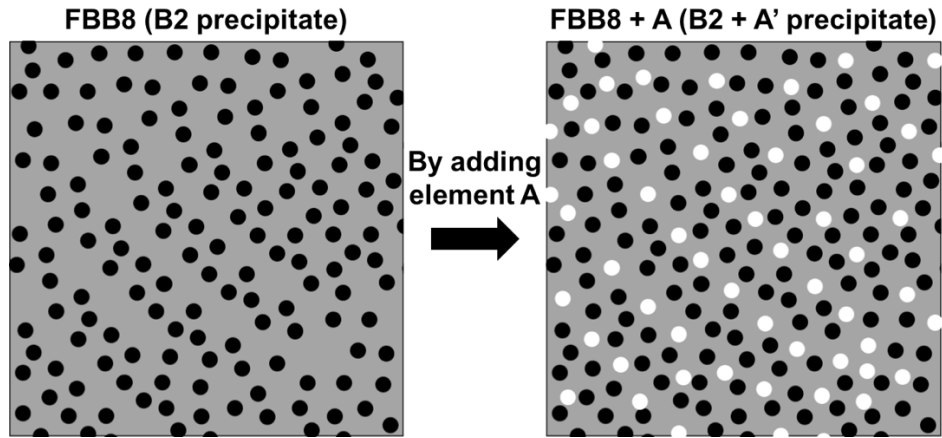


Figure 6. A schematic on the concept of the proposed research. By adding additional element into the FBB8 system, it is possible to form a different secondary phase other than existing B2 phase, and increase the total volume fraction of the particles.

success of the two types of precipitates within a ferritic alloy system, careful thermodynamic studies have to be done for alloy design, which is described in the following paragraphs. Figure 7 demonstrated a brief flow-chart on the basic structure of the research. It starts with alloy design, basically achieved by phase diagram studies, and then through the sample fabrication and heat-treatment, the alloys will be readily prepared for the following microstructural characterization and mechanical tests. After obtaining all the required parameters and properties, these numbers will be input into modified equations, and compared to the calculated numbers, in order to verify the modified equations. The details will be further described and discussed in the following paragraphs.

Alloy Design

Based upon the outcomes of FBB8 + Ti alloys, in order to design an alloy that fully align with the concept of forming particles with multiple phases, the addition of other elements should follow the two following criteria: (1) The element should have decent solubility in Fe, and (2) the element should not form intermetallics with B2-NiAl.

Thus, phase diagrams of the specific element with Fe, Ni, and Al should be considered. By reviewing all the binary phase diagrams with Fe, the following three elements have been chosen for validation of the concept, which are Hf, Zr, and W. The compositions of the designed alloy are shown in Table 1, and in the following paragraphs there will be explanations on the reasons of the designed compositions. For the W, the design is based on the FBB13 within the FBB8-series alloys, emphasizing on lower volume fraction of B2-NiAl precipitate, and the reason is because of the poor ductility of FBB8. FBB13 has much higher room temperature ductility compared to FBB8

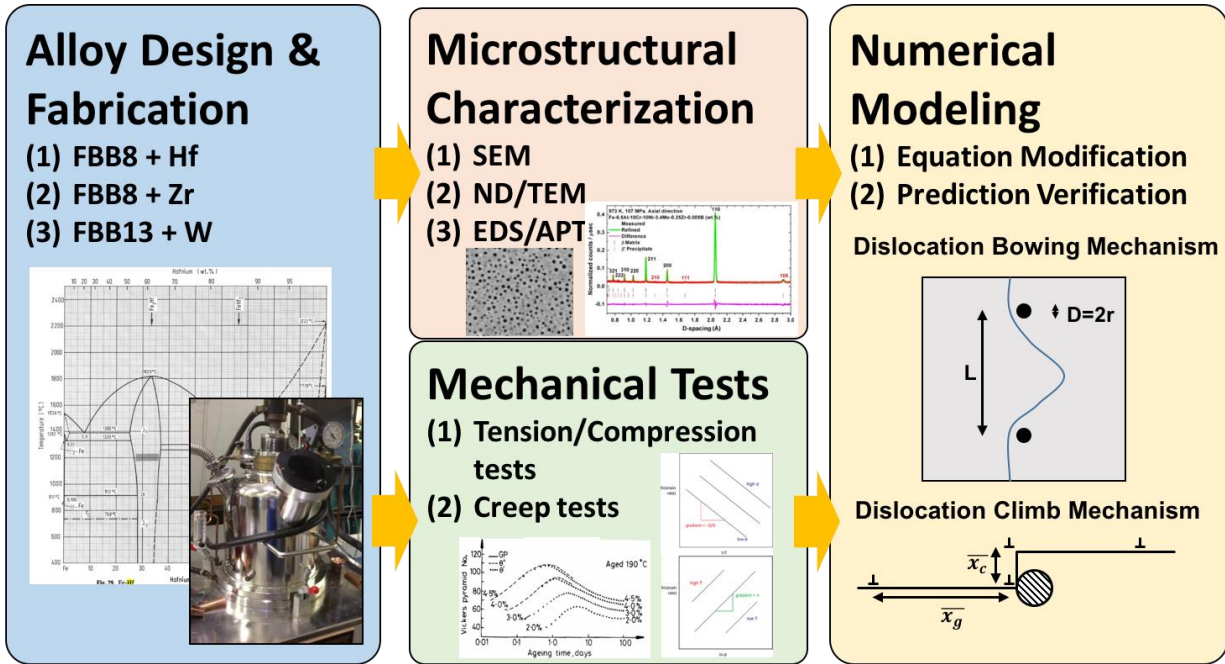


Figure 7. A flow-chart for the proposed research, starts with the alloy design based on the phase diagrams, and then followed with microstructural characterization and mechanical tests, in order to obtain necessary parameters and properties. In the end, all these numbers will be deployed for the modification and verification of the numerical equations.

(bending ductility 5% vs. 1%) and ~8 vol. % of B2-NiAl precipitate, make it wider range for the formation of the Laves phase precipitate.

FBB8 + Hf alloy

Figure 8 shows the Hf-Fe binary phase diagram [25]. As shown in the very left side of Figure 8, the solubility of Hf in Fe is pretty low, only 0.51 at. % at ~1350 °C. Therefore, the optimized volume fraction for the Fe₂Hf precipitation can be pretty low. Due to the purpose of comparing with FBB8 + 2% Ti, 2 wt. % of Hf has been introduced into the FBB8 system and termed FBB8 + 2 wt.% Hf alloy. For the crystal structure of the precipitate, the transition temperature of C14-Fe₂Hf and C15-Fe₂Hf is not clear on the phase diagram, suggesting that either structure could be possibly formed at temperatures higher than 1200 °C. However, since the working temperature of the proposed alloy is ~700 °C, the expecting crystal structure of the Fe₂Hf precipitate should be C15-Fe₂Hf without a doubt. For the precipitation hardening of the Fe₂Hf within Fe/Cr matrix, Kobayashi *et al.* [26, 27] presented that in a ferritic matrix with 9 wt. % of Cr, Hf tends to form Laves phase interfacial precipitates, which forms rows of fine precipitates that periodically distributed within the matrix, as shown in Figure 9. Phase diagram shown in Kobayashi *et al.*'s [26, 27] research exposed that when the Hf content is over 0.66 wt. % and cools down from 1,400 °C, the Fe-9Cr-Hf alloy system goes through $\delta + \text{Fe}_2\text{Hf}$, $\gamma + \text{Fe}_2\text{Hf}$, and $\alpha + \text{Fe}_2\text{Hf}$, and three modes of kinetics had been explained based on the cooling rate. For the high temperature application, the ideal mode of transformation should be the interphase mode, which brings fine (20-50 nm diameter) and periodically distributed particles that homogeneously dispersed within the matrix. This

research provides a hint that under correct homogenization and aging conditions, Fe_2Hf could be well dispersed as strengthener within the ferritic matrix. That being said, if Hf does not form any

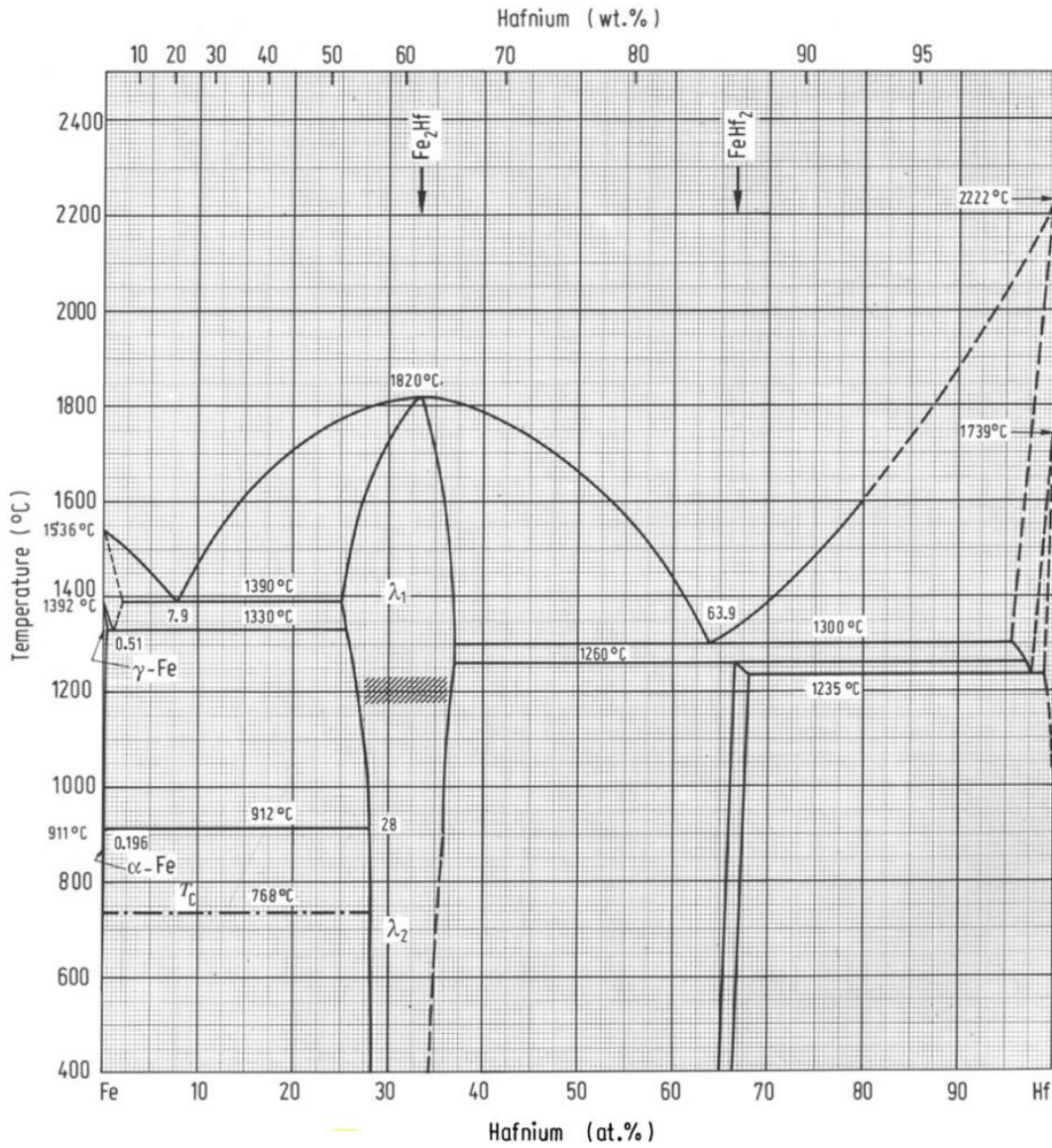


Figure 8. The Hf-Fe binary phase diagram [25]. As shown in the very left side, the solubility of Hf within Fe is really limited.

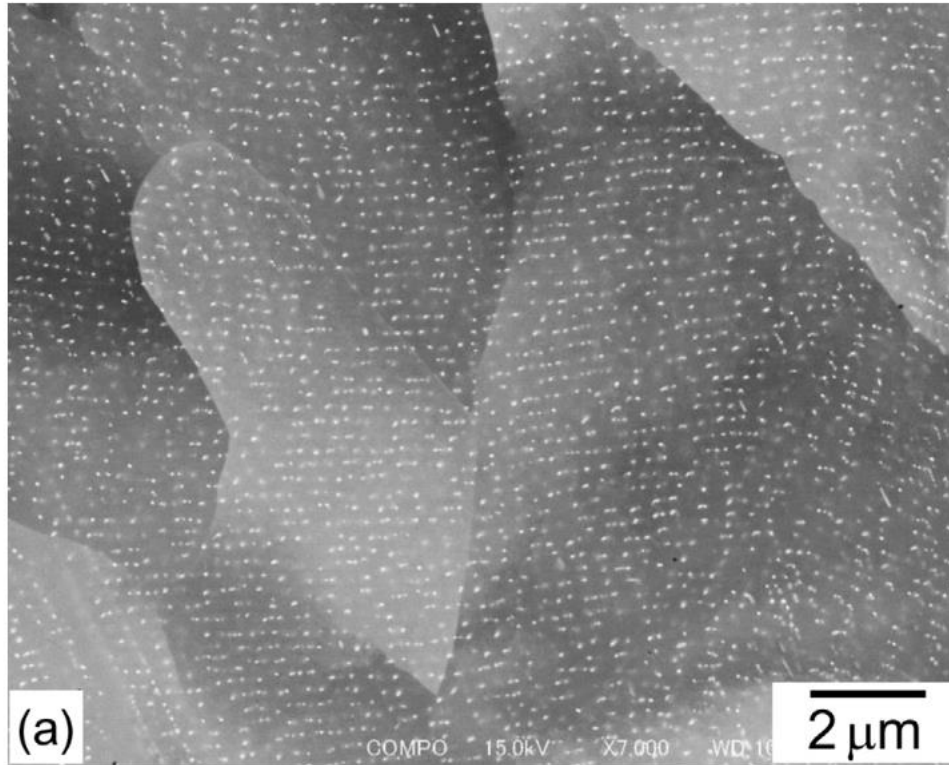


Figure 9. A well-dispersed Fe_2Hf precipitate within Fe-9Cr matrix [27]. The size of the Fe_2Hf precipitates is roughly 20 - 50 nm, indicating that these particles can be a very strong strengthener for the precipitation hardening mechanism.

intermetallics with B2-NiAl, and only dispersed separately with the B2 precipitates, then the overall volume fractions of particles (precipitates) can be increased and the high temperature strength can be further reinforced.

For the interactions between Hf and either Ni, Al, or NiAl, there are no clear discussion on this specific topic in literatures. Figure 10 and Figure 11 are the Hf-Ni and Hf-Al [28] binary phase diagrams respectively, and Figure 12 shows a Hf-Ni-Al ternary phase diagram at 800 °C [28]. From the composition shown in Table 1, it is ~17 wt. % Hf in Ni and ~24 wt. % Hf in Al, indicating that there could be eutectic Ni₅Hf and Al₃Hf intermetallic compounds formed, and refers to Figure 10 with 50% of Ni and Al, it shows that at 800 °C, three phases could be found within the Hf-Ni-Al ternary system, which are B2-NiAl, and α -Ni₃Hf. As a result, the interactions between Hf, Ni, and Al does not seem to be formation of large quantity of intermetallic compounds, due to lack of sufficient Hf dissolves within Fe to interact with Ni and Al. The primary intermetallic compounds will be B2-NiAl, very limited amount of Ni₅Hf, Al₃Hf, as well as Ni₃Hf could be presented. Therefore, the expecting precipitates will be B2-NiAl and small amount of C15-Fe₂Hf.

Table 1. The nominal compositions of the FBB8 + Hf, FBB8 + Zr, and FBB8 + W alloys in weight percent (in atomic percent).

	Fe	Al	Cr	Ni	Mo	Zr	Hf	W	B
FBB8 + 2 wt.% Hf	Bal.	6.5 (12.88)	10 (10.29)	10 (9.11)	3.4 (1.90)	0.25 (0.15)	2 (0.60)	0 (0)	0.025 (0.12)
FBB8 + 2 wt.% Zr	Bal.	6.5 (12.79)	10 (10.22)	10 (9.05)	3.4 (1.88)	2 (1.16)	0 (0)	0 (0)	0.025 (0.12)

FBB13 +
3.5 wt.%
W

Bal.

6.5
(12.79)

10
(10.22)

3
(2.72)

3.4
(1.88)

0.25
(0.15)

0
(0)

3.5
(1.01)

0.025
(0.12)

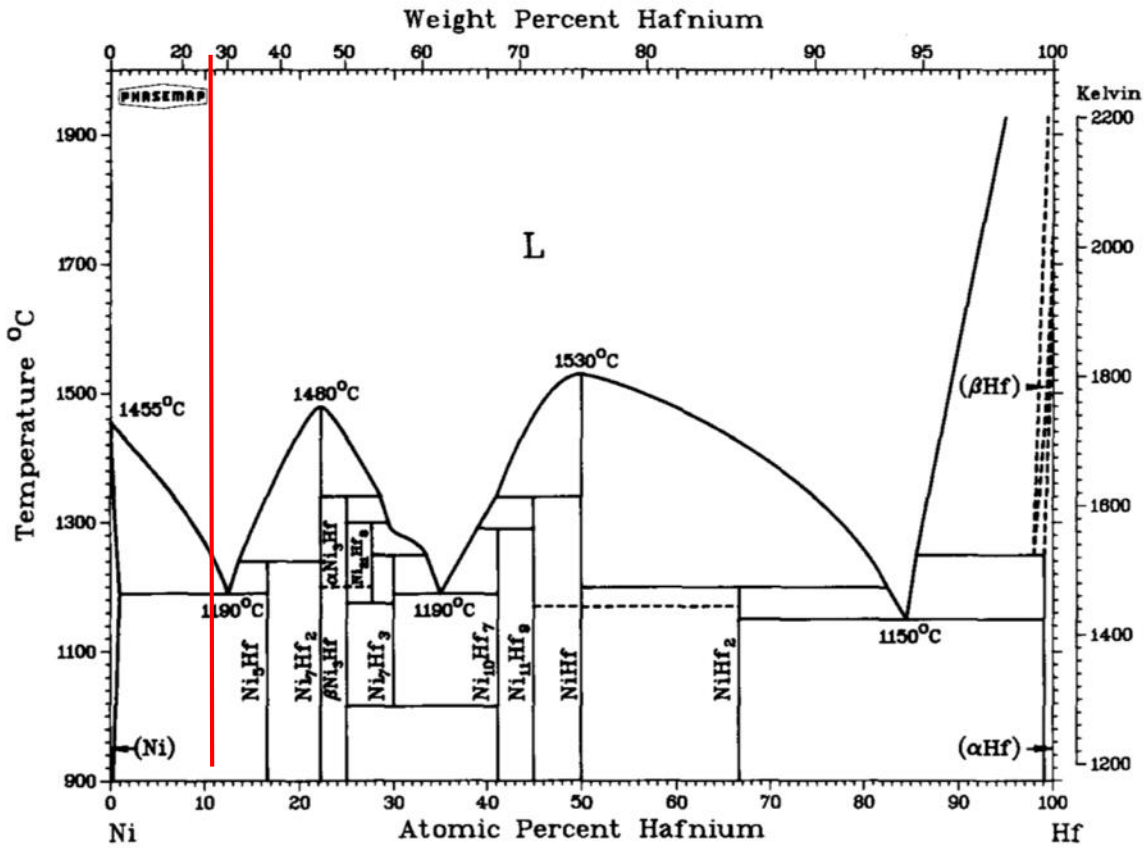


Figure 10. Hf-Ni binary phase diagram [28]. For the composition shown in, there is ~ 17 wt. % Hf within Ni, indicating there will be a eutectic reaction forming Ni₅Hf intermetallic compound.

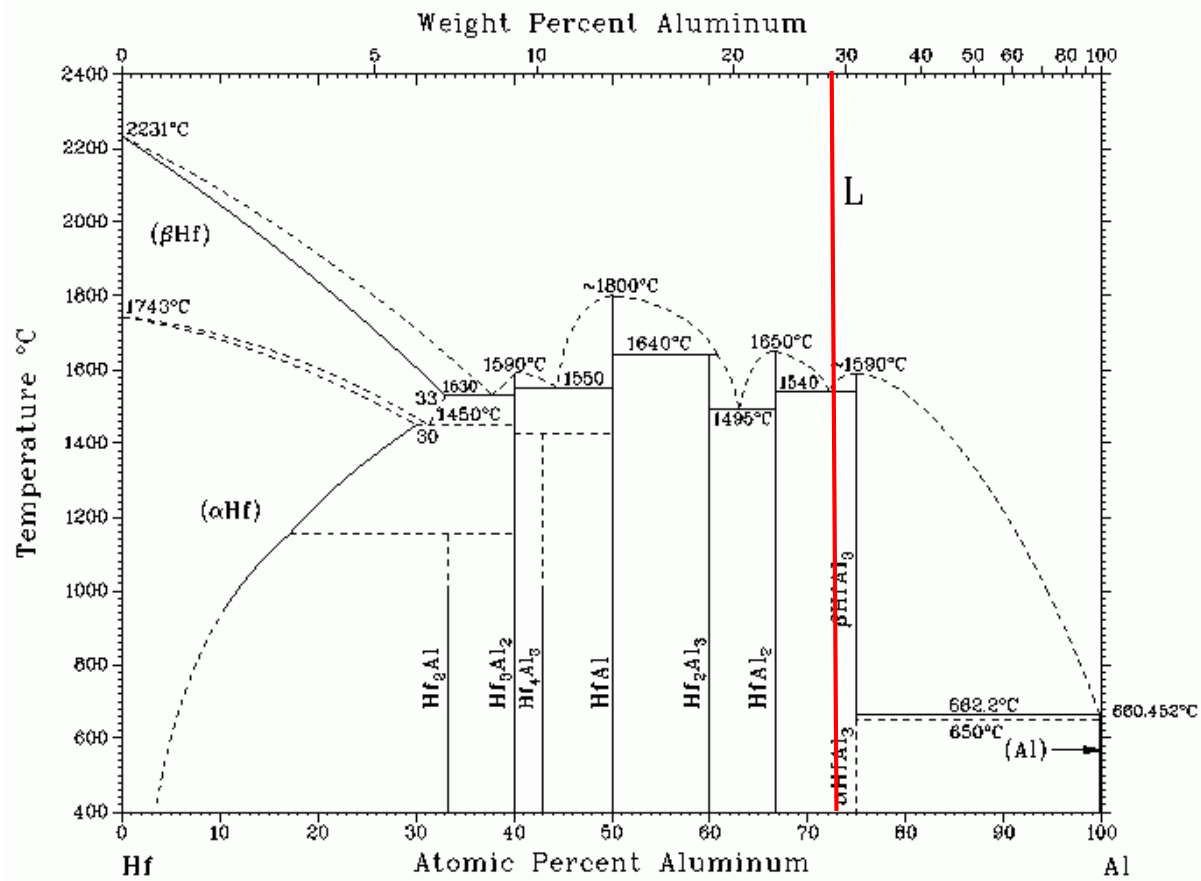


Figure 11. Hf-Al binary phase diagram [28]. For the composition shown in Table 1, there is ~ 25 wt. % Hf within Al, indicating there will be a eutectic reaction forming Al₃Hf intermetallic compound.

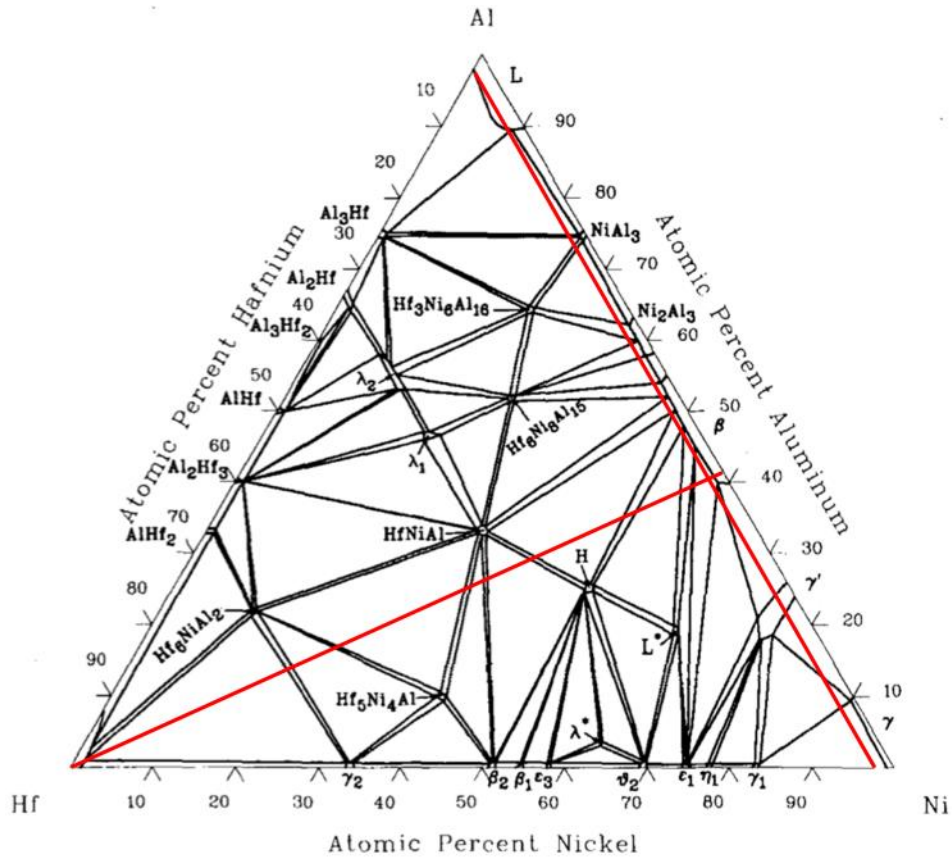


Figure 12. Hf-Ni-Al ternary phase diagram at 800 °C [28]. Based on the respective atomic ratio of the Hf, Ni, and Al within the alloy system, in the ternary phase diagram, there will be B2-NiAl and α -Ni₃Hf presented.

FBB8 + Zr alloy

Following the concept of FBB8 + Hf alloy, several phase diagrams are carefully examined for predicting the general phases within the FBB8 + Zr alloy. Figure 13 shows the Zr-Fe binary phase diagram, and as shown in the very left side of the diagram, the solubility of Zr within Fe is very limited, indicating that the formation of homogeneously dispersed Fe-Zr intermetallic compounds might not occur. According to Figure 13, the secondary phase that might be formed within the FBB8 + Zr alloy system, with the composition shown in Table 1, is Fe₃Zr, with a cubic crystal structure D8a. However, some researches show that, at higher temperature and relatively higher Zr content, the Fe-Zr system goes through a process of $L + \text{Fe}_2\text{Zr} \rightarrow \text{Fe}_3\text{Zr}$ [29], indicating that if the under certain heat treatment conditions, there might be C15-Fe₂Zr phase presented. Note that no matter Fe₃Zr or Fe₂Zr is formed, both intermetallic compounds are FCC-based cubic structures. Figure 14 and Figure 15 show Zr-Ni and Zr-Al [30] binary phase diagram respectively, and Figure 16 shows Zr-Ni-Al ternary phase diagram at 800 °C. Based on the composition shown in Table 1, there are ~ 17 wt. % Zr in Ni and ~ 25 wt. % Zr in Al, indicating the expected intermetallic compounds should be Ni₅Zr and Al₃Zr, which is similar in the Hf-Ni-Al system. In Figure 16, according to the respective ratio of Zr, Ni, and Al, in the ternary phase diagram at 800 °C, there are two intermetallics formed, which are Al₃Ni₂ and Al₂Ni_{1.2}Zr_{0.8}. Both intermetallics are not often seen in the publications, and with the low solubility of Zr in Fe, there wouldn't be enough Zr interacts with Ni and Al. As a result, the most possible particles are still B2-NiAl. Fe₃Zr or Fe₂Zr could be formed and distributed along the grain boundaries.

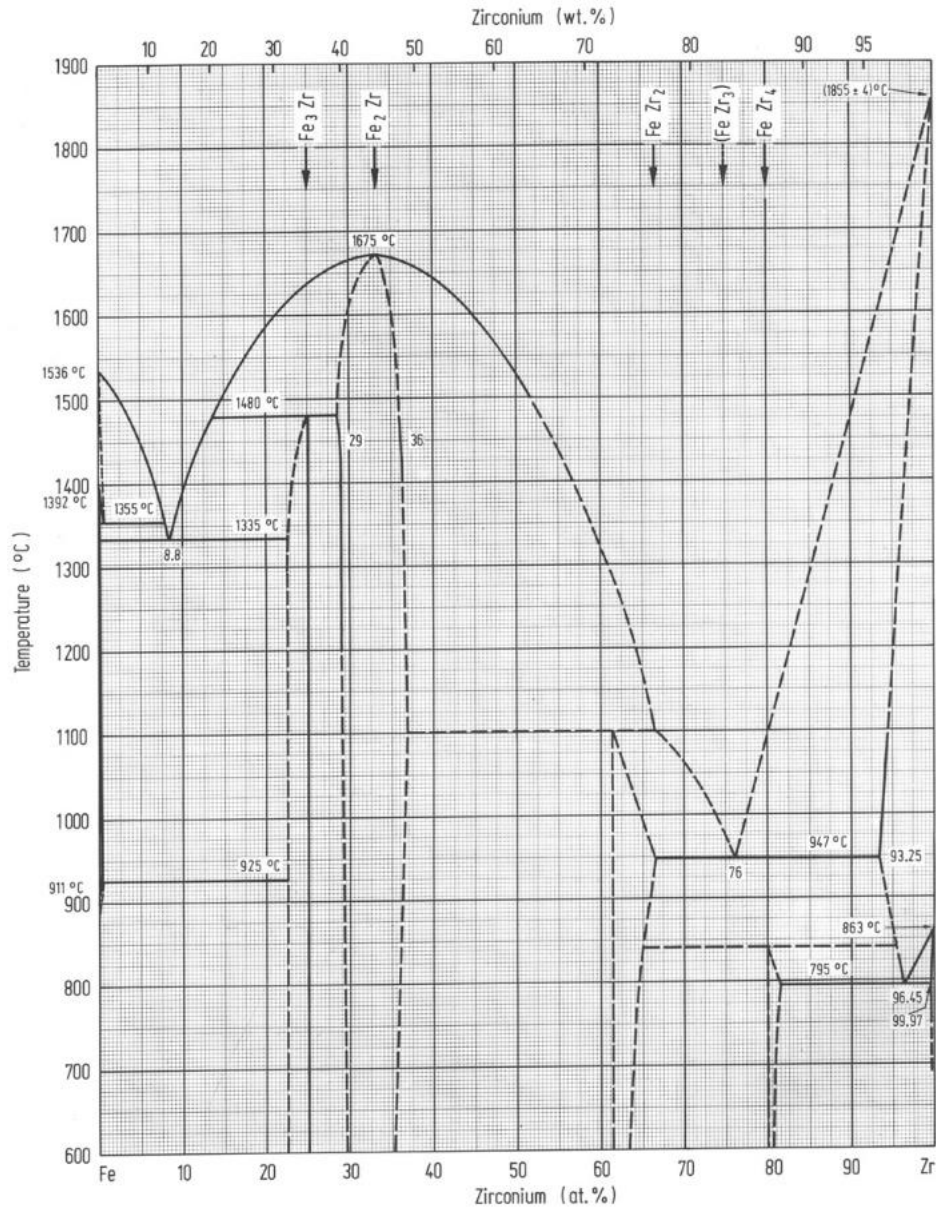


Figure 13. Zr-Fe binary phase diagram [25]. Compared with the Hf-Fe phase diagram shown in Figure 8, the solubility of Zr within Fe is even more limited, suggesting that homogeneously dispersed secondary phases formed with Fe and Zr might not present.

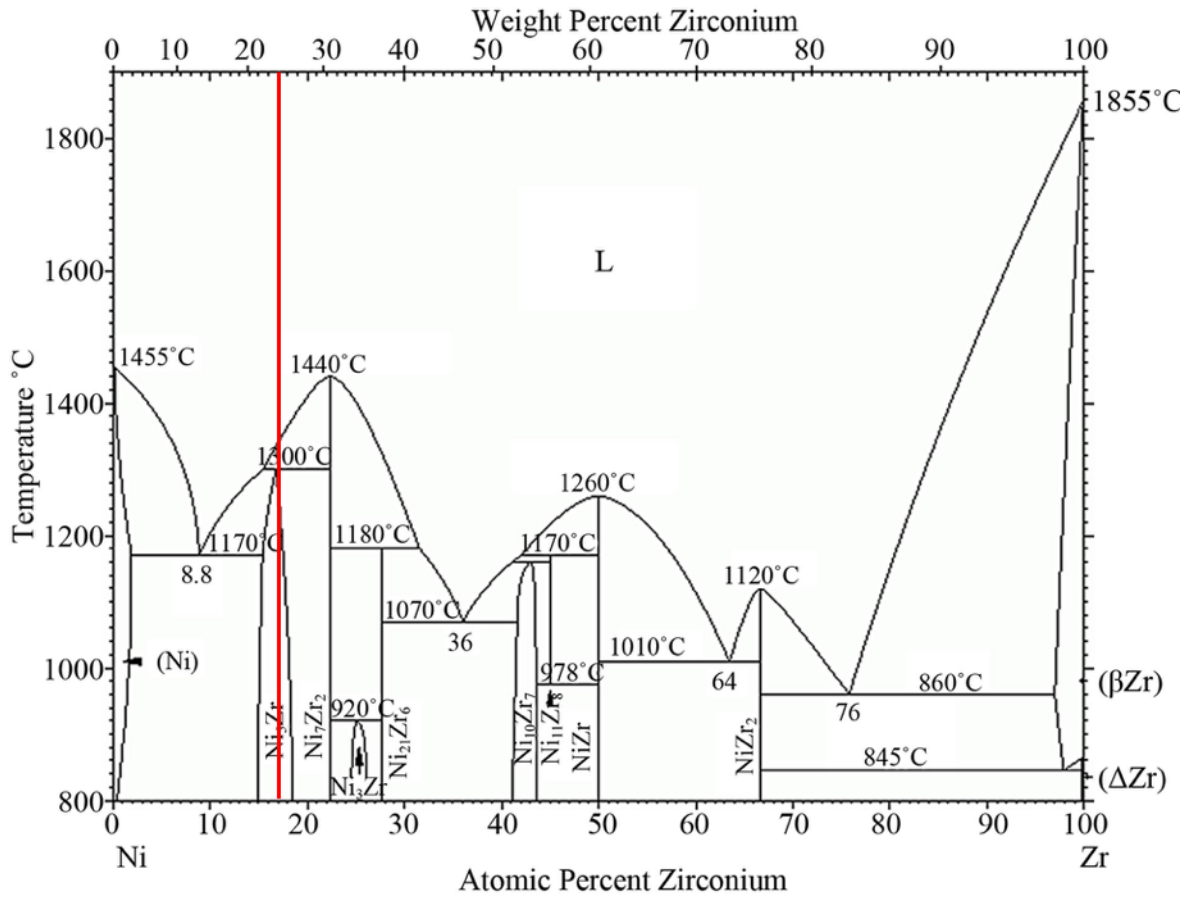


Figure 14. Zr-Ni binary phase diagram [30]. For the composition shown in Table 1, there is ~ 17 wt. % Zr within Ni, indicating there will be a eutectic reaction forming Ni₅Zr intermetallic compound.

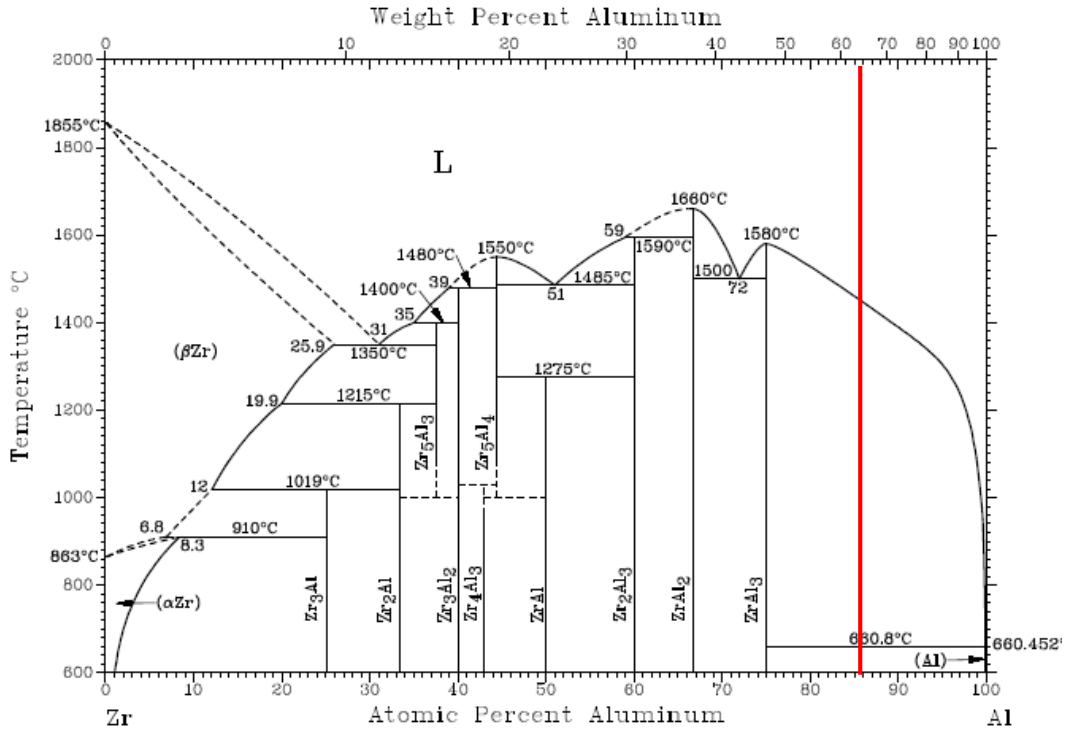


Figure 15. Zr-Al binary phase diagram [30]. For the composition shown in Table 1, there is ~ 25 wt. % Zr within Al, indicating there will be a eutectic reaction forming Al₃Zr intermetallic compound.

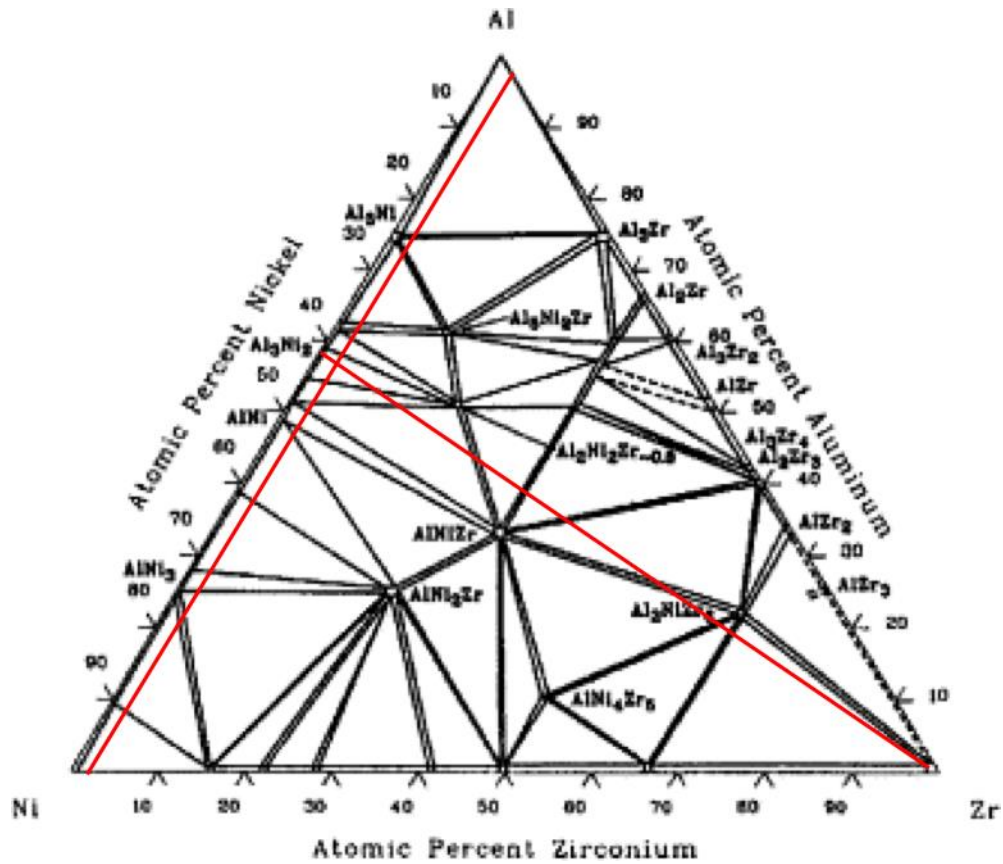


Figure 16. Zr-Ni-Al ternary phase diagram at 800 °C [30]. Based on the respective atomic ratio of the Zr, Ni, and Al within the alloy system, in the ternary phase diagram, there will be Al_3Ni_2 and $\text{Al}_2\text{Ni}_{1.2}\text{Zr}_{0.8}$ presented.

A Calphad calculation based specific on this composition has been done and shown in Figure 17. Notably, at working temperature 700 °C, there will be ~8% of C14-Fe₂Zr exists and ~50% of FCC phase presents. The Calphad predictions are pretty much different with what had been discovered from the phase diagrams presented in the above paragraphs. The first discrepancy is the Fe-Zr phases formed should be FCC-based cubic structures, instead of HCP-based C14-Fe₂Zr. In the Zr-Fe binary phase diagram shown in Figure 13, there is no C14 phase intermetallic compound presented, indicating that either the C14 phase refers to a very different chemical composition that is not related to Zr, or the prediction is totally invalid. The second discrepancy is the very high portion of the FCC phase, which can only refer to the γ -Fe. However, usually for the phase transformation of Fe from BCC to FCC is happened at temperatures above 910 °C, even with high amount of Ni the transformation temperature can be greatly lower, but for the FBB8 working at 700 °C, the majority of the phases presented are still BCC or BCC-based phases (such as B2 phase). The addition of Zr should not be able to cause formation of such a high amount of γ -Fe, therefore, the prediction must be incorrect in some ways.

FBB13 + W alloy

The FBB8 series alloy, or alloy with similar composition, had proved with capability to form both B2-NiAl and Laves phase Fe₂(Mo, W) simultaneously within a martensitic alloy system [24]. Therefore, for the design of the W combined with a ferritic steel, the only problem is how much amount of W should be added. The previous two compositions with Hf and Zr are both having the same problem, which is the lack of enough solubility within Fe. Low solubility ends up with low

fraction of precipitates formed within the matrix, no matter what kind of precipitation it might form, which brings to limited amount of enhancement on the strength. In order to solve this major

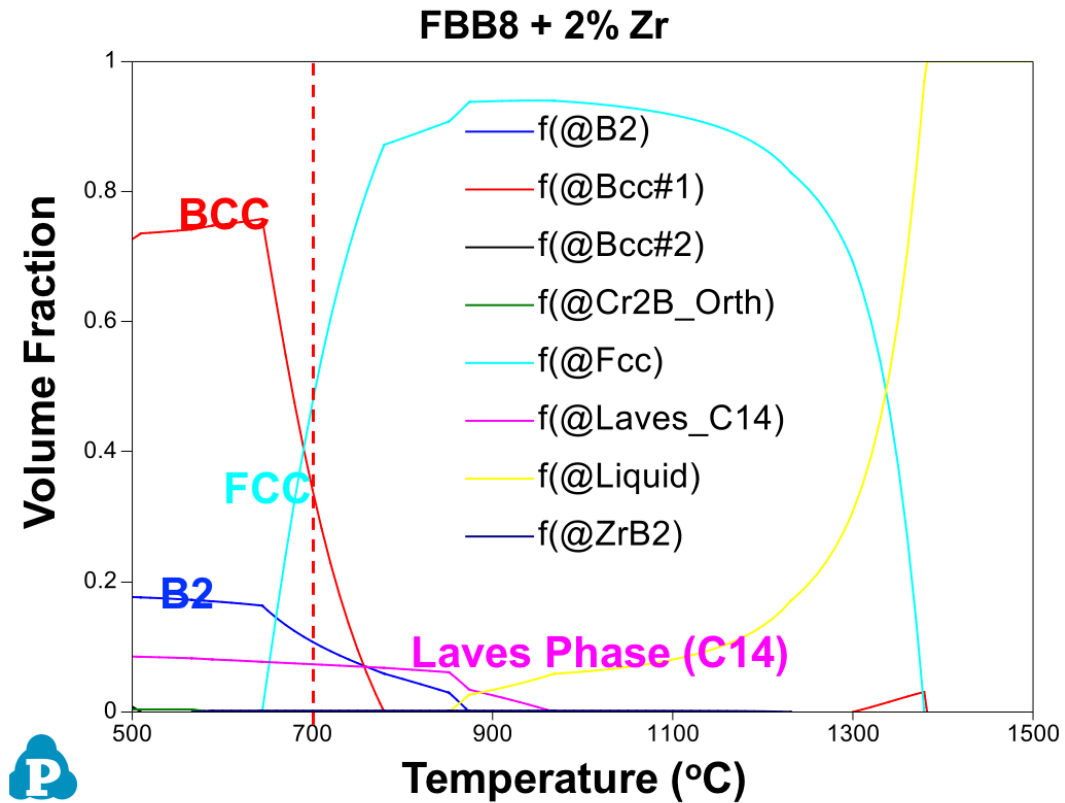


Figure 17. Calphad calculation for the specific composition Fe-6.5Al-10Cr-10Ni-2Zr-3.4Mo-0.025B (wt. %). In the Calphad prediction at 700 °C, there is ~ 8% of C14-Fe₂Zr presented in the alloy system, and ~ 50% FCC phase (should be Fe for such high fraction) present. These predictions do not agree with what are shown in the phase diagrams.

problem, W can be an ideal candidate for such task. Figure 18 shows the W-Fe binary phase diagram [25], W has relatively high solubility in Fe, which is about 3.7 at. % at temperature higher than 1060 °C. When the temperature drops to 800 °C, the solubility reduced to 1.3 at. %, giving a net 2.4 at. % reduction for the formation of λ -Fe₂W precipitation, which is a MnZn₂ type Laves phase (C14) crystal structure. Various studies on the Fe₂W strengthened heat-resistant Fe has been done, and from their discoveries, the Laves phase Fe₂W can be well dispersed within the matrix, or along the grain boundaries, depends on the specific alloy systems and the heat treatment conditions. Most of the Fe₂W strengthened Fe contains C and/or Co, which are not included in the composition proposed in this research, might bring totally different microstructures.

In order to prevent from over-amount of precipitates, the original alloy had changed from FBB8 to FBB13, which only reduces the Ni from 10 wt. % to 3 wt. %, and the B2-NiAl particles from ~16 vol. % to ~7 vol. %. The quantity of the W added to FBB13 is ~3.5 wt. %, basically it is possible to form about 10 vol. % of Laves phase particles, and make the total volume fraction of particles at about 17 vol. %. According to Sun *et al.*'s research [24], with a more balanced B2-NiAl and C14-Fe₂W, it could be able to reach an outstanding strength.

Brief Summary on the Prediction of Precipitations

Based on the above examinations on the phase diagrams for the proposed compositions on this research, Table 2 shows the summarized predicted precipitations. Basically, based on the phase diagrams, only FBB8 + 2 wt.% Hf and FBB8 + 6.5% W alloys have possibilities on forming well-dispersed precipitations with two different phases, and aligned well with the major concept of the

proposed research. FBB8 + 2 wt.% Zr alloy on the other hand, supported by Calphad calculation, indicating that a ~ 8% of C14 might exist in the microstructure. Since the Calphad calculation

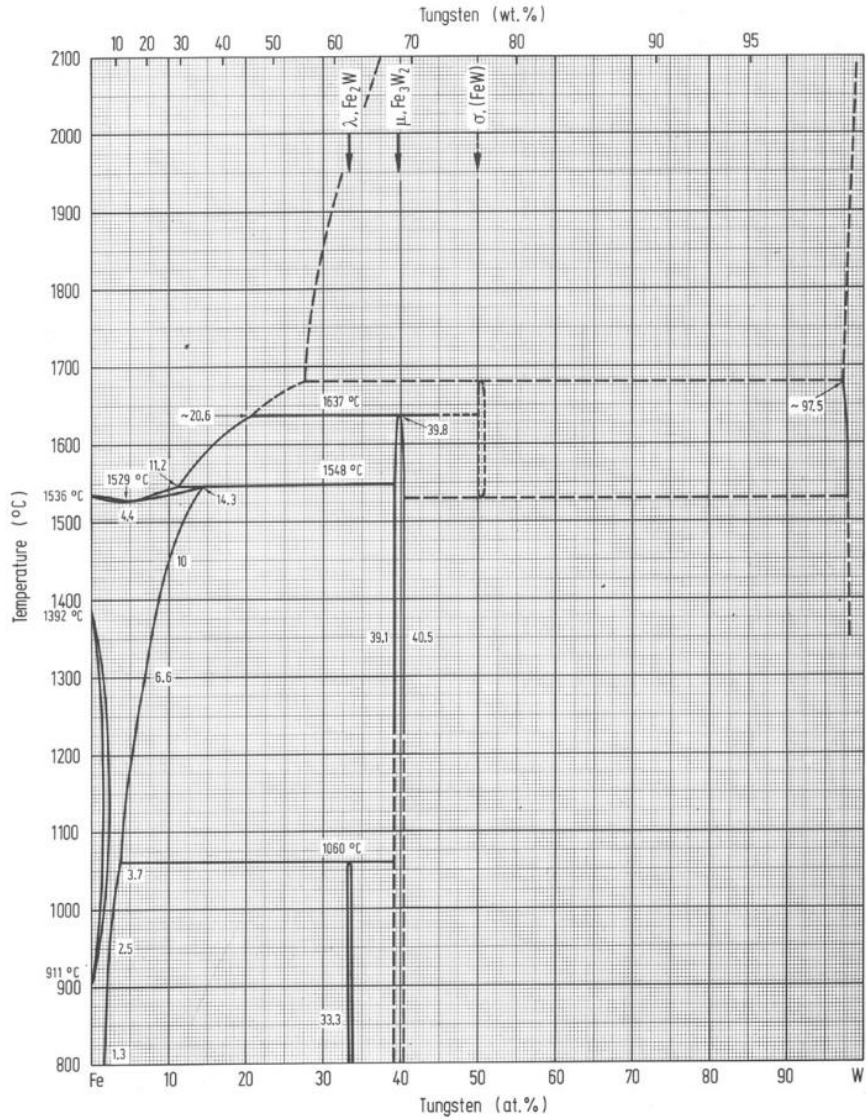


Figure 18. W-Fe binary phase diagram [25]. W has ~ 3.7 at. % (~10 wt.%) solubility in Fe at temperature high than 1060 °C, and drops to ~ 1.3 at. % at 800 °C, making it an ideal candidate for precipitation hardening. The precipitation could be λ -Fe₂W, which is a MnZn₂ type Laves phase (C14) crystal structure.

serves totally different prediction with the phase diagram examinations, a careful microstructure characterization on FBB8 + 2 wt.% Zr alloy might still be conducted, in order to verify which approach (Calphad or phase diagrams) predicts better on the microstructure.

Table 2. Predicted precipitations for the proposed alloy systems, and other possible phases

Alloy	Predicted Precipitations	Other Possible Phases
FBB8 + 2 wt.% Hf	B2-NiAl, C15-Fe ₂ Hf	α -Ni ₃ Hf
FBB8 + 2 wt.% Zr	B2-NiAl	Al ₃ Ni ₂ /Al ₂ Ni _{1.2} Zr _{0.8} , D8a-Fe ₃ Zr/C14-Fe ₂ Zr
FBB13 + 3.5 wt.% W	B2-NiAl, C14-Fe ₂ W	-

CHAPTER THREE

MATERIALS AND METHODS

Followed with the alloy compositions designed in Table 1, the designed alloys are fabricated, heat-treated, microstructural identified, and mechanical tested via various of techniques, in order to generally understand its microstructure and performance. Table 3 lists all the required microstructural, as well as mechanical parameters for understanding the microstructure and performance of alloys. Generally, alloy samples are fabricated by arc-melting method, following with the nominal composition listed in Table 1. Samples specifically for the mechanical tests are machined, and then heat-treated by proper heat-treatment processes, depends on the microstructure they possess, in order to optimize its mechanical performance. Generally, the samples are solution-treated at 1,200 °C for up to 2 days, and then aged for 100 hours in a vacuum environment. All the prepared sample are then measured or tested by techniques described in the following paragraphs. After fabrication, the mechanical testing samples are machined into specific geometry shown in Figure 19. These samples are prepared specifically for tensile tests, including tensile tests and tensile creep tests. Compression samples are fabricated into rod shape and then machined into geometry shown in Figure 20.

Table 3. Nomenclatures for the parameters served in the equations in this research

Parameter	Physical Meaning
L	Inter-particle spacing
r	Precipitation radius
f_v	Precipitation volume fraction
$\dot{\epsilon}_{ss}$	Steady-state creep rate
n	Stress exponent of creep
Q	Creep activation energy

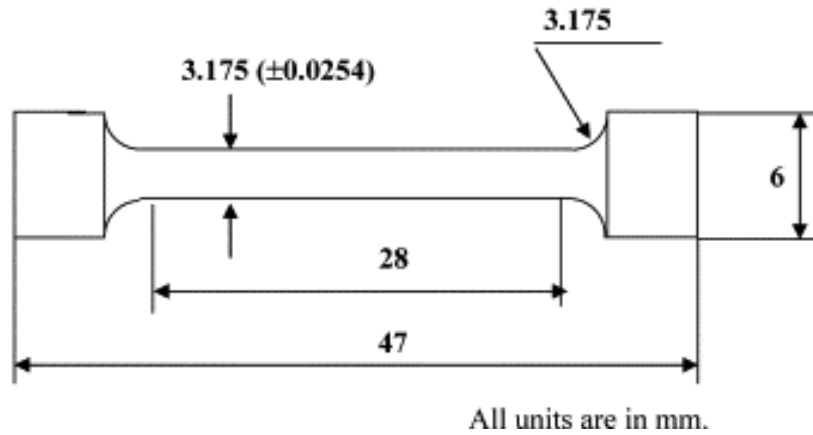


Figure 19. The sample geometry for tensile samples, including samples for creep tests

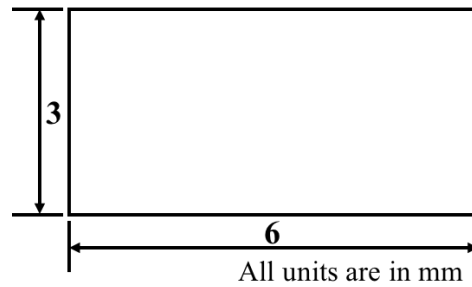


Figure 20. The sample geometry for compression test samples.

Microstructural Characterizations

Microstructural characterization aims to quantitatively gather most of the required microstructural information listed in Table 3. Generally, scanning electron microscopy (SEM), synchrotron/neutron diffraction, and atom probe tomography (APT) techniques are required.

Scanning Electron Microscopy (SEM)

SEM provides a general view on the microstructure and basic microstructural information, such as average precipitate size, precipitate volume fractions, and secondary phase morphology and distribution. Such information helps in modeling and basic understanding on the complexity of the microstructure, which further helps in the following measurement on crystal structures and elemental partitioning.

The SEM sample is examined by SEM with Electron Back-Scatter mode, for better contrast between the matrix and secondary phases. The acquired SEM images are analyzed by image processing software ImageJ, for the determination of the average precipitate sizes and precipitate volume fractions. The conversion of the measured areal fraction of precipitates from the SEM into volume fraction is calculated by:

$$f_v = \frac{4}{3} \pi \left(\frac{f_a}{\pi} \right)^{\frac{3}{2}} \quad (4)$$

Where f_v is the volume fraction and f_a is the areal fraction measured by SEM images. By this conversion, the volume fraction of precipitates could be roughly evaluated from SEM images, and serve as a reference for the measurement from diffraction pattern analysis.

Neutron/Synchrotron Diffraction

Diffraction techniques are required for identify the crystal structures of each phases presented in the alloy. Both transmission electron microscopy (TEM) and neutron/synchrotron X-ray diffraction serve well for providing structural information, but in a different way. TEM is able to provide a local information in the microstructure, such as the specific crystal structure for a nano-sized particle, and neutron/synchrotron X-ray diffraction provides a more general information on the overall crystal structure in the alloy that statistically more reliable. Combined with the SEM information, either approach is able to give the information on the crystal structure required for this research.

The obtained neutron diffraction data is analyzed by the General Structure Analysis System (GSAS), since the obtained neutron diffraction pattern is already an integrated one-dimensional diffraction pattern, it can be analyzed directly by GSAS without a conversion. The obtained synchrotron diffraction data however is a two-dimensional diffraction pattern that requires an integration. Therefore, for synchrotron data the GSAS II software is utilized because it includes the function of integration. The phase identification, lattice parameter determination, as well as volume fraction of each phases, are majorly achieved by GSAS/GSAS II software by performing Rietveld refinement until the least χ^2 value, which is a factor of how match is the microstructural setup with the measured diffraction pattern.

Atom Probe Tomography (APT)

APT is a technique that is able to provide information of the chemical composition on a tiny volume of the microstructure, which for this research, tells us the elemental partitioning of the

additive elements to the alloy systems. The APT task is performed by Cameca Instruments Local Electrode Atom Probe (LEAP) 4000X HR, located in the Oak Ridge National Laboratory. The APT samples are prepared from the the SEM samples, and further prepared by focus ion beam (FIB) technique, in order to capture the specific area of interest. APT on the other hand, is able to provide precise chemical composition for nm scale particles, which might be the major particle sizes for the precipitation.

Mechanical Tests

Mechanical tests are the major method for the evaluation on the performance of the designed alloys. The primary method is the tension/compression tests, since the strength and ductility is major concern for most of the materials. Alloys with outstanding features are then tested at high temperature (700 °C), and further tested by creep test.

Tension/Compression Tests

The major reason to perform a tension/compression test is to obtain the basic mechanical properties: yield strength and ductility, for the assessment of the developed alloys. The tension/compression tests are both performed using MTS testing system. The alloys are tested at two different temperatures: room temperature (~25 °C) and 700 °C, primarily by tensile test if feasible. However, many of the creep resistant materials have almost non-ductility at room temperature, making tensile tests performed at room temperature unable to acquire a full stress strain curve (the samples simply fractured before yielding). Therefore, in order to obtain the room temperature mechanical

properties, compression test will be an alternative method in order to obtain a full stress-strain curve. For both tension and compression tests, the strain rate is restricted at $1 \times 10^{-3}/s$. The sample geometries are as shown in Figure 19 for tension samples and Figure 20 for compression samples.

Creep Tests

The steady-state creep rate of the designed alloys is primarily the goal for creep tests, in order to obtain essential numbers to calculate with the microstructural parameters. The steady-state creep test is performed at 700 °C in two ways, first is a full creep life test performed with 70 MPa applied stress on FBB13 + 3.5 wt.% W alloy, and the obtained creep curve will be utilized in fitting with the model demonstrated later in the next sub-chapter. Second creep test is a stress jump test, in order to obtain as many results from different stresses on one sample. Three stresses are applied in the creep jump test on the FBB13 + 3.5 wt.% W alloy, which are 30 MPa, 37 MPa, and 50 MPa, respectively. The steady-state creep rate can be used for acquiring the stress exponent, as well as the threshold stress. For the creep tests, the sample geometry follows the same geometry as tension test samples, as shown in Figure 19.

Numerical Calculations

Numerical calculations or modeling help in linking the microstructural features with the actual mechanical performances quantitatively. In this research, two specific areas are concerned, which is the yield strength of the alloys, and creep behavior of the FBB13 + 3.5 wt.% W alloy. Both these two mechanical properties can be linked with the observed microstructural information shown in

next chapter. In the following paragraphs, an introduction on the models and equations utilized in this research is presented.

Yield Strength

The crystal structure of the precipitates and the matrix brings different strengthening effects to the alloy system, generally categorized, it can be separated into two baskets: (1) coherent precipitates, and (2) incoherent precipitates. Ideally, when the precipitate is coherent with the matrix, the dislocation does not need to change their route when moving through the precipitates, therefore, this process is called dislocation-shearing, the dislocation cuts through the precipitate. While in the scenario of dislocation-shearing, there are three mechanisms that cause the dislocation-shearing difficult, which are (1) the lattice mismatch between the matrix and the precipitate, (2) the creation of a new interface, and (3) the modulus difference between the matrix and the precipitate. For the lattice mismatch between the matrix and the precipitate, Eq. (5) is the equation illustrating the coherency strengthening from the precipitate [39]:

$$\Delta\sigma_{coherency} = M\chi(\varepsilon G)^{\frac{3}{2}} \left(\frac{rfb}{\Gamma} \right)^{\frac{1}{2}} \quad (5)$$

Where M is the Taylor factor, for a BCC matrix it is 2.9. χ is a constant, in this particular case it is 2.6. G is the shear modulus of the matrix, which is 77 GPa for BCC Fe [41]. b is the burger's vector of the matrix, which is roughly 0.25 nm. Γ is the dislocation line tension, which can be approximated into $\Gamma \approx \frac{Gb^2}{2}$. Microstructural parameters r is the average precipitate size, f is the volume fraction of the precipitate, and ε is the lattice mismatch between the lattice parameter and

the precipitate, which can be defined as $\varepsilon = \frac{a_p - a_m}{a_m}$, where a_p is the lattice parameter of the precipitate and a_m is the lattice parameter of the matrix.

For the creation of a new interface, since the dislocation cuts through the precipitate creates two new interfaces between the precipitate and the matrix, which leads to the order strengthening as shown in Eq. (6) [39]:

$$\Delta\sigma_{order} = 0.81M \frac{\gamma_{APB}}{2b} \left[\left(\frac{3\pi f}{8} \right)^{\frac{1}{2}} - f \right] \quad (6)$$

Where γ_{APB} is the anti-phase boundary energy per unit area of the precipitate. In the case of our alloy system, the coherent precipitate is always the B2-NiAl, its anti-phase boundary energy is ~ 200 mJ/m² [35, 36, 40].

For modulus difference, the energy for dislocation to moving through changes, which leads to the modulus strengthening, as shown in Eq. (7) [43]:

$$\Delta\sigma_{modulus} = 0.0055M(\Delta G)^{\frac{3}{2}} \left(\frac{f}{\Gamma} \right)^{\frac{1}{2}} b \left(\frac{r}{b} \right)^{\frac{3m}{2}-1} \quad (7)$$

Where m is a constant as 0.85 in this particular calculation [24], ΔG is the shear modulus difference between the matrix and the precipitate. In our alloy systems, it is the shear modulus difference between the BCC-Fe (77 GPa [41]) and the B2-NiAl (73 GPa [42]).

The strengthening from the coherent precipitates can be easily summed up from the above three mechanisms, since when the dislocation-shearing scenario happens, all three mechanisms activated simultaneously.

For incoherent precipitates, usually dislocations do not cut through them, since the preferential slip planes for different crystal structures vary quite a lot, the incoherent interface between the precipitates and the matrix plays a role of entrapping the dislocations. Therefore, the general interaction between the dislocation and incoherent precipitate is called bypass, which the dislocation tries to go bypass the precipitate instead of moving through it. The bypass mechanism can be formulated as Eq. (8), which is the famous Orowan equation [44]:

$$\Delta\sigma_{Orowan} = M \frac{0.4Gb}{\pi\sqrt{1-\nu}} \frac{1}{L} \ln\left(\frac{2r_s}{b}\right) \quad (8)$$

Where ν is the Poisson's ratio of the matrix, which is ~ 0.3 . L is the average inter-precipitate spacing, and r_s is the average radius of the cross-section that precipitate cuts the slip plane, which can be calculated by $r_s = (2/3)^{1/2}r$. Both the average inter-precipitate spacing L and the precipitate radius r are to describe only on one type of the precipitate. In a system that includes two or more types of precipitate, these parameters need to be modified.

Figure 21 is a schematic illustrating the assumptions of the alloy system that composes of two different particles, which has a box with its side length as a . Within it there are two kinds of particles, red one has number of n_1 , radius r_1 , and volume fraction V_{f1} , and blue one has number of n_2 , radius r_2 , and volume fraction V_{f2} . Therefore, by definition:

$$V_{f1} = \frac{n_1 \frac{4}{3} \pi r_1^3}{a^3} \quad (9)$$

$$V_{f2} = \frac{n_2 \frac{4}{3} \pi r_2^3}{a^3} \quad (10)$$

In order to obtain the equivalent inter-precipitate spacing \bar{L} , the first step is to obtain the remaining volume of the box, it is:

$$V_{remain} = a^3 - n_1 \frac{4}{3} \pi r_1^3 - n_2 \frac{4}{3} \pi r_2^3 \quad (11)$$

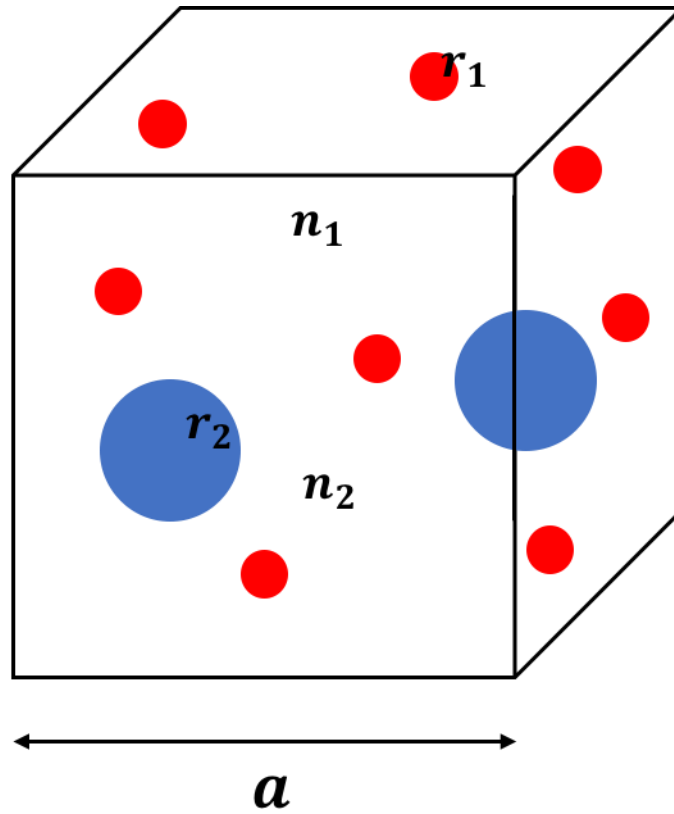


Figure 21. A schematic on the assumption of an alloy system composed of two different kinds of particles, where it assumes that both particles are both spherical, and each of them has their respective numbers, sizes, and volume fractions.

And then, since there are total $n_1 + n_2$ particles inside the box, for each particle, it can be assumed to occupy $V_{remain}/n_1 + n_2$ space within the box, and then the equivalent inter-precipitate spacing \bar{L} can be obtained:

$$\bar{V} = \frac{V_{remain}}{n_1 + n_2} = \frac{a^3 - \frac{4}{3}\pi r_1^3 - n_2 \frac{4}{3}\pi r_2^3}{n_1 + n_2} = \bar{L}^3 \quad (12)$$

For a real alloy system, we do not know how many number of each type of particles is actually within the imaginary box, nor the actual size of the box, therefore the key is to replace the variables a , n_1 , and n_2 with volume fractions and average sizes, which are variables that we can measure, therefore by converting Eq. (9) and (10) into expression in terms of V_f , n , and a^3 , eventually \bar{L} can be obtained as:

$$\bar{L} = \sqrt[3]{\frac{1 - V_{f1} - V_{f2}}{\frac{3}{4\pi} \left(\frac{V_{f1}}{r_1^3} + \frac{V_{f2}}{r_2^3} \right)}} \quad (13)$$

Where the term a^3 cancels out during the derivation, leaves an expression in terms of only V_f and n for the respective particles. The Eq. (13) describes a system with two types of particles, which have their distinct particle size (without a distribution, all the same type of particles has the same size) and volume fraction, as shown in Figure 22(a). In order to further generalize Eq. (13) for a scenario that all these particles have a size distribution, the Eq. (13) should be converted into:

$$\bar{L} = \sqrt[3]{\frac{1 - \sum V_{fi}}{\frac{3}{4\pi} \sum \frac{V_{fi}}{r_i^3}}} \quad (14)$$

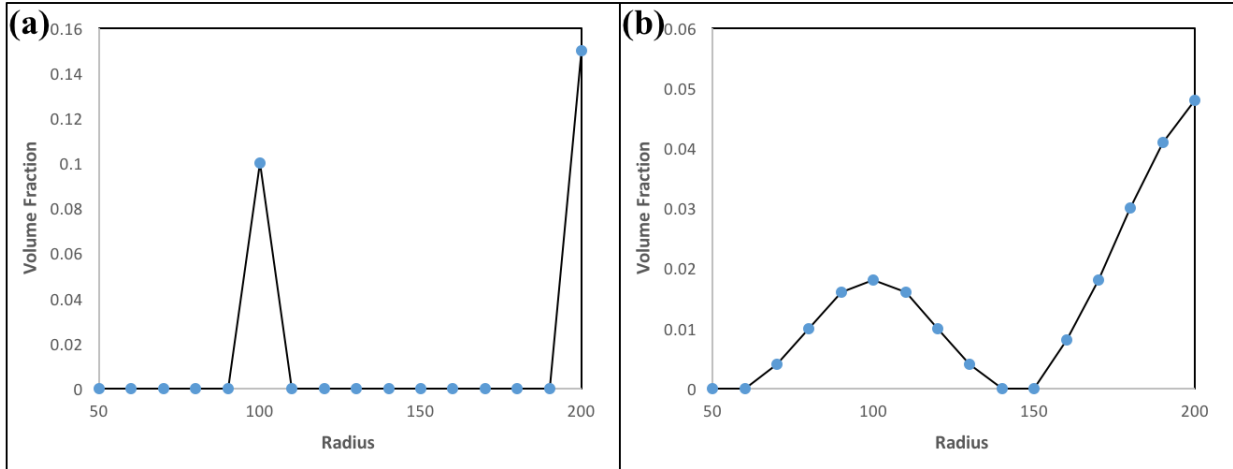


Figure 22. A schematic on the particle sizes between (a) without a distribution, where same type of particles has the same size, and (b) with a distribution, where two different types of particles have various of sizes and corresponding volume fraction.

Where the V_{fi} and r_i indicate the volume fraction and the radius for the i th segment of the distribution, as illustrated in Figure 22(b). For example, in Figure 22(b), every 10 nm can be one segment, and has a corresponding volume fraction.

For the equivalent radius \bar{r} , the concept is to sum up the total volume of the particles first, and then divide the total number of the particles, in order to obtain the average volume for each particle:

$$\bar{V} = \frac{n_1 \frac{4}{3} \pi r_1^3 + n_2 \frac{4}{3} \pi r_2^3}{n_1 + n_2} = \frac{4}{3} \pi \bar{r}^3 \quad (15)$$

The term $\frac{4}{3}\pi$ can be canceled out, and then replace n to an expression in terms of V_f , n , and a^3 , we can then obtain:

$$\bar{r} = \sqrt[3]{\frac{V_{f1} + V_{f2}}{\frac{V_{f1}}{r_1^3} + \frac{V_{f2}}{r_2^3}}} \quad (16)$$

The Eq. (16) is for only two types of particles that each type of particle has the same size. A generalized expression for particles that has a size distribution is:

$$\bar{r} = \sqrt[3]{\frac{\sum V_{fi}}{\sum \frac{V_{fi}}{r_i^3}}} \quad (17)$$

The equivalent inter-precipitate spacing \bar{L} and equivalent radius are then obtained from the above derivations. The purpose of for derivation on these equivalent parameters is to replace the original parameter with a number that fits more with the actual situation.

Usually for a conventional precipitation strengthened alloy, there's only one major precipitate and it is either coherent or incoherent, therefore in order to quantize its strengthening effect, one should only determine either coherent precipitate dominates or incoherent precipitate dominates, and only calculate accordingly. However, in the alloys we've developed, coherent precipitates and incoherent precipitates could be similar in volume fraction or strengthening effect, therefore both of the strengthening will be calculated and evaluated, based on their respective volume fraction and microstructural parameters.

Creep Model

The creep test result analysis can be done in two ways, fitting with empirical model and fitting with physical-based model. For the fitting with empirical model, in this research, the Eq. (18) is used:

$$\dot{\varepsilon} = A \left(\frac{\sigma - \sigma_{th}}{G} \right)^n \exp \left(\frac{-Q}{RT} \right) \quad (18)$$

Where A is an empirical parameter that obtained via data fitting, σ is the applied stress, n is the stress exponent that indicates the dominant creep mechanism, Q is the activation energy that also differs depending on the dominant creep mechanism, R is the gas constant $8.314 \text{ J/K} \cdot \text{mol}$, and T is temperature. The term σ_{th} is the threshold stress, which is the feature of this empirical equation, that only applies for the materials with stress exponent n larger than 5. Usually for creep resistant alloys strengthened by precipitates, the stress exponent is around 5 to 10, therefore, a threshold stress is introduced in order to better comprehend its underlying creep mechanism. For the calculation in this research, we would assume $n = 4$ (assuming the precipitates are the barriers for the dislocation movement so the dislocations go through a dislocation climb process), in order to obtain the threshold stress for further comparisons with other materials.

For the physical-based model, in this research a continuum damage model is utilized, in order to describe the full creep process until the sample fails, as well as predicting the steady-state creep rate. The continuum damage model is developed by C. Shen [45], and in this research the major structure of the model will follow their formulation, with modifications on the dislocation part specifically, in order to reflect the effects of two types of particles. A detailed introduction on C. Shen's model is in Appendix, and in the following paragraphs, the introduction on model will be

emphasize on the dislocation part of the model. In C. Shen' model the strain is caused by growth of cavities, and the growth of cavities are majorly contributed from dislocation-related behaviors and diffusion of atoms. Basically, dislocation-related behaviors are stress-dependent, which means the difference on applied stress affects the contribution of the dislocation-related mechanisms. Diffusion-related mechanisms on the other hand, are temperature-dependent, therefore while in this research the creep tests are conducted on 700 °C only, the contribution from diffusion-related mechanisms will not change too much. For the later data analysis, both the contributions from the and diffusion-related mechanisms will be recorded and discussed, nevertheless, since this research focuses on the two types of precipitates, the dislocation-related mechanisms will be more detailed examined and emphasized.

Usually for a physical-based creep model that describes a precipitate strengthened alloy, it has the form shown as Eq. (19):

$$\dot{\epsilon} = K \left(\frac{D_{SD}}{b^2} \right) \left(\frac{G\Omega}{kT} \right) \left(\frac{\bar{x}_g}{\bar{x}_c} \right) \left(\frac{\sigma}{G} \right)^3 \quad (19)$$

Where K is a constant, D_{SD} is the diffusivity of self-diffusion of the matrix, Ω is atomic volume, \bar{x}_g is the average glide distance that is roughly the precipitate spacing, \bar{x}_c is the average climb distance that is roughly the precipitate radius, therefore the term $\frac{\bar{x}_g}{\bar{x}_c}$ is generally the volume fraction f of the precipitate. This power law function is the basis of many creep models, by alternating the stress exponent, the power law function can be applied to many different creep model that dominated by different mechanisms. However, Weertman [46] first found that for precipitate strengthen materials, a hyperbolic sine equation better describes its overall creep profile. Later Dyson [47]

also developed a constitutional model for the creep of precipitate strengthened alloys that based on a hyperbolic sine equation. Therefore, currently most of the research on the creep of precipitate strengthened alloys are generally follow with the hyperbolic sine equation. In this research and C. Shen's model, Eq. (20) is the equation that primarily utilized in the analysis of the creep data obtained from the creep tests:

$$\dot{\varepsilon} = \begin{cases} \rho A D_V f (1 - f) \left(\sqrt{\frac{\pi}{4f}} - 1 \right) \sinh \left(C \frac{\sigma_{eff} - \sigma_B - \sigma_0}{MkT} b^2 \lambda \right), & \text{if } \sigma_{eff} - \sigma_B - \sigma_0 > 0 \\ 0, & \text{otherwise} \end{cases} \quad (20)$$

Where A and C are constants, ρ is the density of dislocations, which can be measured by TEM or neutron/synchrotron diffraction. D_V is the volume diffusivity of the matrix, k is the Boltzmann constant $1.38 \times 10^{-23} \text{ J/K}$, and λ is the average spacing of the precipitates. In this equation there are three stress terms, which are the effective stress σ_{eff} , back stress σ_B , and stress caused by the interaction of the dislocations σ_0 . The stress caused by the interaction of the dislocations will be calculated as Eq. (21):

$$\sigma_0 = 0.25 M G b \sqrt{\rho} \quad (21)$$

Here the shear modulus is the number at the working temperature, which is 700 °C. Therefore, the number of G at 700 °C for polycrystalline α -Fe is 57.0 GPa [38, 48].

The back stress σ_B depends on the interactions between the dislocation and the precipitates, as discussed in previous chapters, these interactions can be briefly categorized into shearing and climbing, which refer to coherent precipitate and incoherent precipitates, respectively. Two equations describing the back stress contributed from shearing (Eq. (22), [49]) and climbing (Eq. (23), [47, 50, 51]) mechanisms are:

$$\sigma_{shear} = \frac{\gamma_{APB}}{2b} \left[\left(\frac{12\gamma_{APB}fr}{\pi Gb^2} \right)^{\frac{1}{2}} - f \right] \quad (22)$$

$$\sigma_{climb} = \frac{2f}{1+2f} \sigma_{eff} \left[1 - \exp \left(- \frac{1+2f}{2(1-f)} E \frac{\varepsilon^{dislocation}}{\sigma_{eff}} \right) \right] \quad (23)$$

Where E is the elastic modulus, and $\varepsilon^{dislocation}$ is the strain caused specifically by dislocations. Eq. (22) is not dependent on strain, therefore while creep progressing, the back stress from shear mechanism should remain the same. However, during the creep the precipitate size coarsens, r becomes larger, and this causes σ_{shear} varies from time to time. For Eq. (23), since the back stress from climb mechanism is dependent on strain, that is to say when creep progressing and the sample deforms, σ_{climb} also changes. Combined with σ_{eff} which is also a parameter that varies with the neck cross-section, σ_{climb} is a parameter that constantly changes during the whole creep process. Since the major goal of this research is trying to introduce a secondary particle into the alloy system, in order to further strengthen the alloy, it is essential to take the effect of the secondary particle into account. Therefore, the average spacing of precipitates λ in this model will be replaced by the equivalent inter-precipitate spacing \bar{L} , and the net stress term of $\sigma_{eff} - \sigma_B - \sigma_0$ will be further deduced into $\sigma_{eff} - \sigma_{B_1} - \sigma_{B_2} - \sigma_0$, where two different back stresses regarding to two types of precipitates. Both back stresses are calculated from either Eq. (22) or Eq. (23), since microstructural-wisely the two types of precipitates are different, the back stresses of them will be different.

The calculation of back stresses not only depends on the initial microstructural characteristics of the two types of precipitates, but also their instantaneous status. That is to say, the coarsening of

the precipitates also need to be taken into consideration. Generally, the coarsening of precipitates follows the form of Ostwald ripening equation [69-71]:

$$D^3 - D_0^3 = K \exp\left(\frac{-Q}{RT}\right) t \quad (24)$$

Where D is the instantaneous precipitate diameter and D_0 is the initial precipitate diameter. K is a pre-factor for coarsening, and Q is the activation energy for coarsening. The coarsening of the B2-NiAl precipitates within a α -Fe matrix has been well-studied by Sun *et al.*[8], according to his results on various temperatures, the coarsening pre-factor K and activation energy Q can be obtained by fitting, which are $6.57 \times 10^{17} \text{ nm}^3/\text{s}$ and 270 kJ/mol , respectively. For the coarsening of the Laves phases precipitates or other phases, currently there's no coarsening kinetics research on the possible Laves phases precipitates in the community, therefore in this research, the coarsening of Laves phases precipitates will be estimated based on the creep curve fitting.

Evolution of the dislocation density is also a factor that affects the creep rate significantly. In the report of C. Shen [45], they obtained the initial and saturated dislocation densities by estimation and fitting from the creep curve, and assume the evolution of the dislocation density during the creep process as a linear process, which means the dislocation density starts from the initial number and ends at the saturation number linearly. In this research the same approach applied, and the dislocation density dependence of this model will be discussed in detail in next chapter.

The general concept of the calculation is to calculate the instantaneous strain, and strain rate, as well as other parameters that are dynamic in the creep progress. Because of the above parameters are dynamic, they change dependently on the instantaneous status of the creep, in the calculation

a time interval needed to be defined, and then recalculate the status every time interval passed. For example, if the time interval is 1 minute, then the dynamic parameters need to be updated every 1 minute. For a prediction of a one-hour creep, that means it will generate 61 data points for every minute within that one hour.

The prediction from the above model requires sequential calculations, depends on the time interval defined, therefore huge amount of calculations is required. In this research, the calculations are achieved by utilizing the script programmed in Excel VBA, for both convenient to access and easier to plot figures. The script is demonstrated in the Appendix. For most of the calculations, the time interval is defined from 1 minute to 10 minutes, in order to save the calculation resources. General parameters that applied for the calculations are listed in Table 4, most of them are from the experiments in this research, extracted from other research, or obtained by fitting with the prediction and the experimental results.

Table 4. General parameters for creep calculations

Parameter	Physical Meaning	Number	Source
<i>A</i>	Creep strain rate coefficient	0.03	Fitted
<i>C</i>	Creep strain rate coefficient	1.2	Fitted
<i>DDi</i>	Initial Dislocation Density	6.5×10^{12}	Assumed
<i>DDf</i>	Final Dislocation Density	4.76×10^{13}	Assumed
<i>APB</i>	Anti-phase Boundary Energy	200 mJ/m^2	[35, 36, 40]
<i>Dv</i>	Volume Diffusivity of the Matrix	$6.69 \times 10^{18} \text{ m}^2/\text{s}$	[37]
<i>M</i>	Taylor Factor	2.9	Typical for BCC metal
<i>bv</i>	Burger's Vector	$0.25 \times 10^{-10} \text{ m}$	For ferrite matrix
<i>SM</i>	Shear Modulus	57 GPa	[38, 48]
<i>YM</i>	Young's Modulus	148.2 GPa	Converted from shear modulus

CHAPTER FOUR

MICROSTRUCTURE

Scanning Electron Microscopy (SEM)

Figure 23(a) (b) (c) are the SEM images of the FBB8 + 2 wt.% Hf, FBB8 + 2 wt.% Zr, and FBB13 + 3.5 wt.% W alloys, presenting an overview of the microstructure for respective alloys. The general feature of the microstructure of these three alloys is the large white agglomerates that distributed along the grain boundaries and within grains as a micron-sized irregular shaped agglomerate. Since these white agglomerates or particles are not presented in the original FBB8, suggesting that they are possibly Hf/Zr/W contained intermetallic compounds. A closer look on the microstructure of FBB8 + 2 wt.% Hf and FBB8 + 2 wt.% Zr alloys (Figure 23(d) (e)) presents black dots homogenously dispersed all over the whole microstructure, which are the B2 phase precipitates, same as presented in the original FBB8 alloy [7-10]. These precipitates are ~ 100 - 130 nm in diameter, and mostly spherical-shaped, suggesting a high coherency between the precipitates and its α phase matrix. The statistic measurement based on the SEM images shows that these B2 precipitates are ~14 - 18% volume fraction for both FBB8 + 2 wt.% Hf and FBB8 + 2 wt.% Zr systems, which is very similar with their FBB8 origin. In Figure 23(a), it is noteworthy that within the FBB8 + 2 wt.% Hf alloy, there are irregularly-shaped, white particles homogeneously dispersed within the matrix, with ~1 μm width and 1-10 μm length, which is not presented within the FBB8 + 2 wt.% Zr alloy.

Figure 23(f) shows a closer look on the microstructure of FBB13 + 3.5 wt.% W alloy. There are not as many black dots as shown in the microstructure of FBB8 + 2 wt.% Hf and FBB8 + 2 wt.% Zr alloys, FBB13 + 3.5 wt.% W alloy has relatively small amount and size of precipitates within

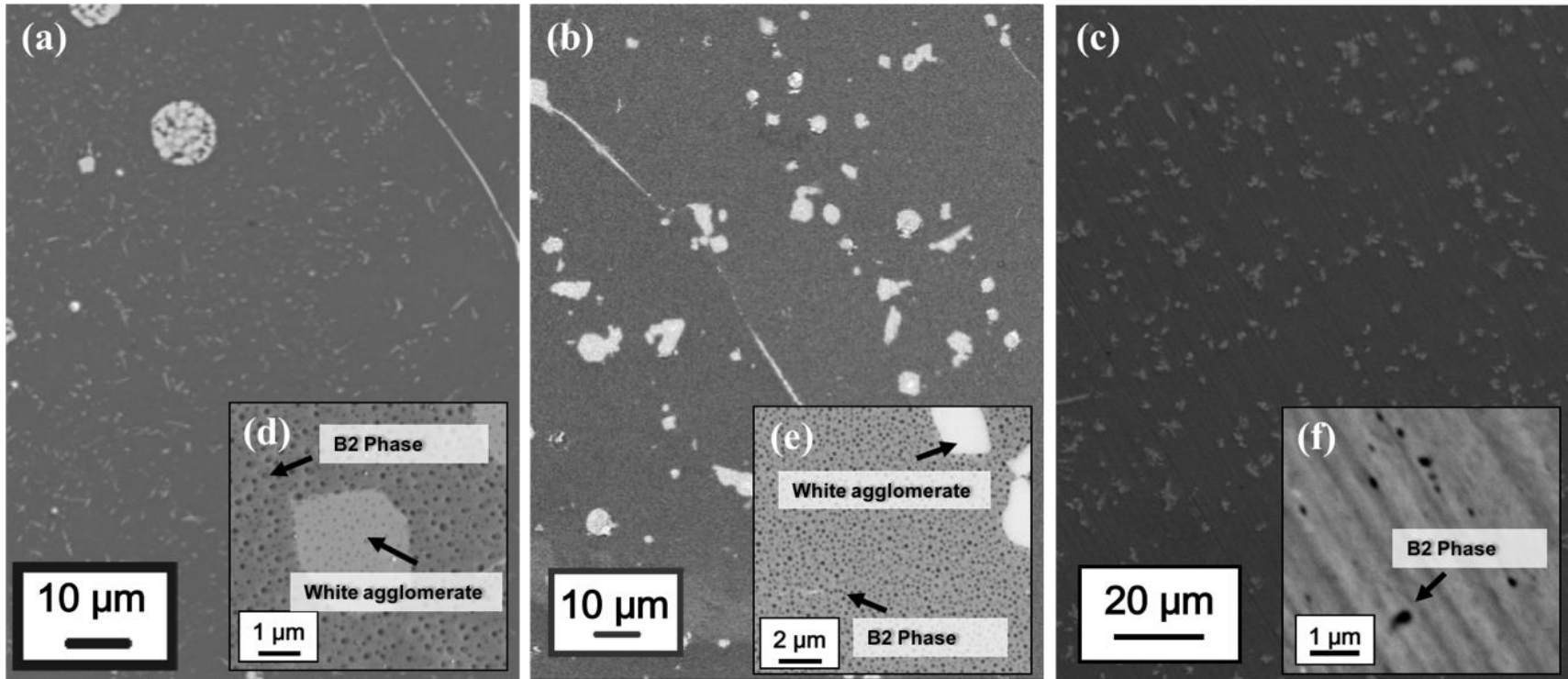


Figure 23. SEM images for a general and detailed view of the microstructure of (a) (d) FBB8 + 2 wt.% Hf, (b) (e) FBB8 + 2 wt.% Zr, and (c) (f) FBB13 + 3.5 wt.% W alloys. Three distinct areas can be identified within the microstructures, which are the matrix, the B2 phase particles, and white agglomerates.

its matrix. The black particles, which are B2 precipitates, have average size of ~80 nm, and the white irregular-shaped particles, which are W contained intermetallic, have average size of ~1.9 μm . The volume fractions of the B2 phase within FBB13 + 3.5 wt.% W is less than 1%, which is hugely lower than within FBB8 + 2 wt.% Hf and FBB8 + 2 wt.% Zr alloys. For the W contained intermetallic particles, the volume fraction is ~ 1%. These SEM-based numbers are summarized within Table 5 and will be applied for the calculations on the mechanical properties shown in the following paragraphs.

Figure 24 shows a closer look on the actual morphology of the white agglomerate within the FBB8 + 2 wt.% Zr alloy, and it shows that numerous of spherical white particles segregate together, with particles ~10 - 100 nm. These white particles segregate as a larger agglomerate, and eventually deposit along grain boundaries, or randomly within grains.

Table 5. Diameters and volume fractions for particles observed using SEM technique

	FBB8 + 2 wt.% Hf		FBB8 + 2 wt.% Zr		FBB13 + 3.5 wt.% W	
	Diameter (nm)	Volume fraction (%)	Diameter (nm)	Volume fraction (%)	Diameter (nm)	Volume fraction (%)
B2-NiAl	90	14	122	16	80	<1
White Particles	1400	0.4	-	-	1914	1

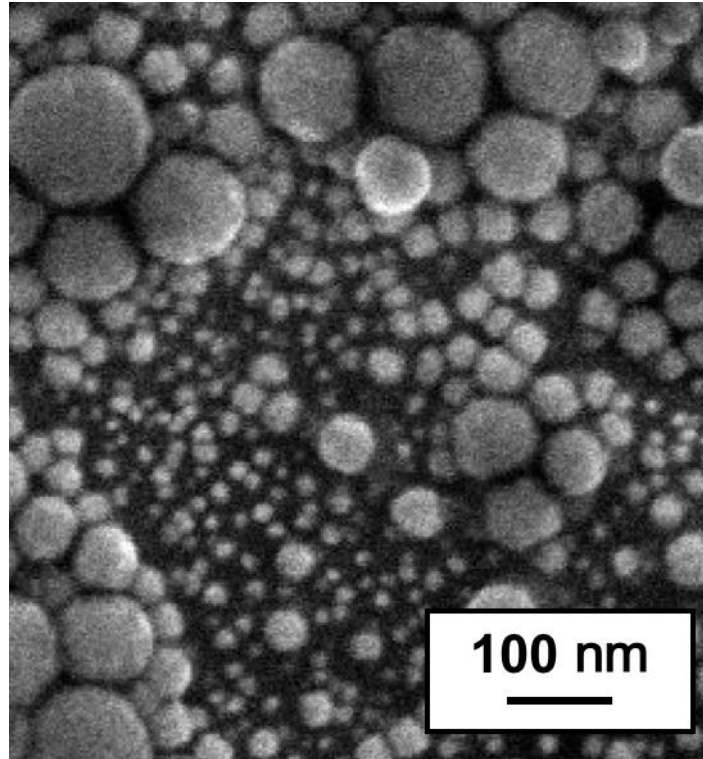


Figure 24. A closer view on the white agglomerate on FBB8 + 2 wt.% Zr exposes that the white agglomerate is composed of numerous white particles.

Atom Probe Tomography (APT)

Figure 25 shows the APT measurements on the FBB8 + 2 wt.% Hf, FBB8 + 2 wt.% Zr, and FBB13 + 3.5 wt.% W alloys, and Table 6 is a summary of the concentrations of each element extracted from the APT measurements. Each area represented the matrix, B2 phase precipitates, and white particles is selected and measured. The results show clearly that the white particles are enriched by the inputted Hf/Zr/W elements. Common assumption on the stoichiometry on the white agglomerate in the respective alloy, based on Fe-Hf/Zr binary phase diagrams, should be Fe_2Hf for FBB8 + 2 wt.% Hf alloy, $\text{Fe}_{23}\text{Zr}_6$ for FBB8 + 2 wt.% Zr alloy, and Fe_2W for FBB13 + 3.5 wt.% W alloy, according to the enriched Fe and Hf/Zr/W contents. For the FBB8 + 2 wt.% Hf alloy system, the ratio of the Fe/Hf is 3.85, much higher than the Fe/Hf ratio for Fe_2Hf . And for the FBB8 + 2 wt.% Zr alloy systems, the ratio of the Fe/Zr is 2.69, which is oppositely lower than the Fe/Zr ratio for $\text{Fe}_{23}\text{Zr}_6$. For the FBB13 + 3.5 wt.% W alloy system however, the results show that not only the white particles are enriched by W, but also enriched by Mo. Previous research had shown that within the ferritic system, W and Mo easily form Laves phase intermetallic compounds [68]. The ratio of Fe/(W, Mo) is only 1.45, lower than the Fe/(W, Mo) ratio of the $\text{Fe}_2\text{W}/\text{Fe}_2\text{Mo}$. For FBB8 + 2 wt.% Hf and FBB8 + 2 wt.% Zr alloy systems, these unexpected results suggest that the Hf/Zr enriched intermetallics are probably not the only species in the white agglomerate regimes, since in Figure 24 there's actually Fe matrix interweaved with the white agglomerates, suggesting that the Fe concentration within the white agglomerate is excessive than the actual intermetallic stoichiometry. On the other hand, in the FBB8 + 2 wt.% Hf and FBB8 + 2 wt.% Zr

alloys, the black dots remain almost 1:1 ratio of Ni and Al, represents B2-NiAl stoichiometry, suggesting that adding Hf/Zr into the alloy systems does not cause the formation of L2₁ phase

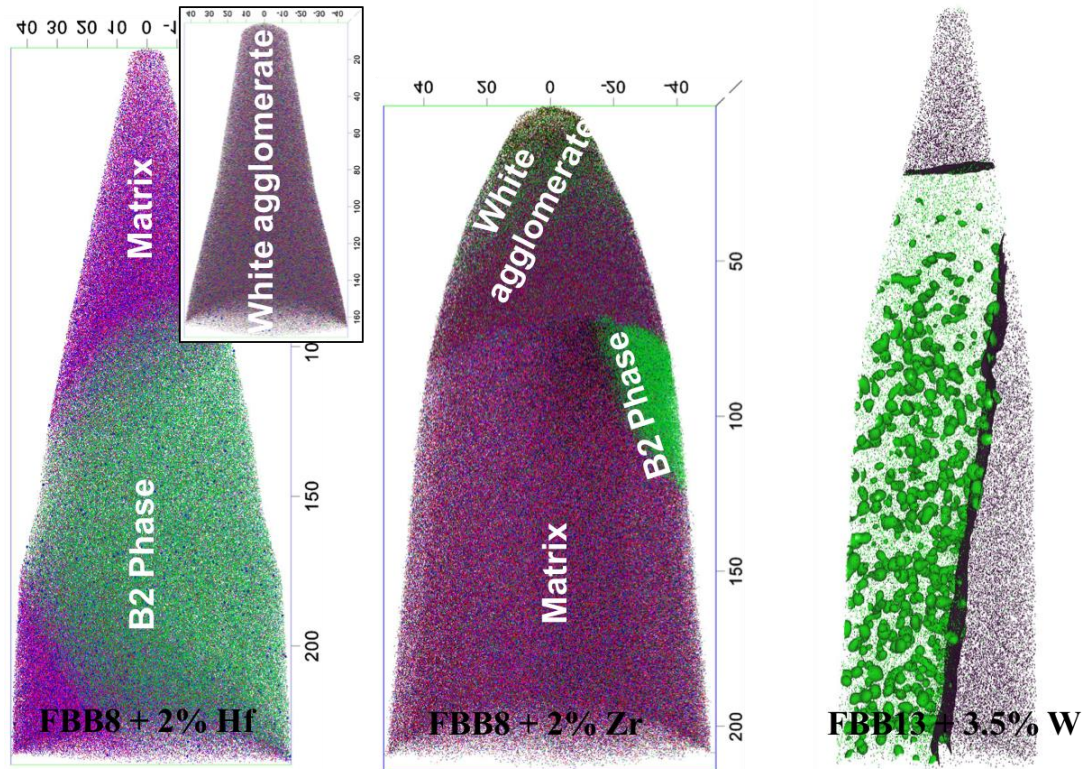


Figure 25. APT measurements on the different areas within FBB8 + 2 wt.% Hf, FBB8 + 2 wt.% Zr, and FBB13 + 3.5 wt.% W alloys. The areas are identified and selected under SEM, and later prepared into APT samples by FIB. For FBB13 + 3.5 wt.% W alloy, one can notice that there's many tiny B2 phase particles distributed within the matrix, which are ~5 nm in diameter.

Table 6. Elemental distributions on each phases within FBB8 + 2 wt.% Hf and FBB8 + 2 wt.% Zr alloys

	FBB8 + 2% Hf			FBB8 + 2% Zr			FBB13 + 3.5% W		
	White agglomerate (at. %)	B2 (at. %)	Matrix (at. %)	White agglomerate (at. %)	B2 (at. %)	Matrix (at. %)	White particle (at. %)	B2 (at. %)	Matrix (at. %)
Fe	56.33%	8.37%	77.29%	52.32%	8.82%	77.10%	46.43%	33.05%	67.03%
Hf	14.95%	0.01%	-	-	-	-	-	-	-
W	-	-	-	-	-	-	13.26%	0.57%	0.38%
Al	7.00%	44.04%	6.56%	10.38%	45.32%	6.87%	4.52%	34.75%	15.04%
Ni	10.02%	47.33%	1.93%	10.02%	45.59%	2.02%	0.59%	23.65%	1.88%
Cr	3.56%	0.23%	12.34%	3.30%	0.25%	12.47%	10.97%	4.56%	9.54%
Mo	3.15%	0.01%	1.73%	0.94%	0.01%	1.54%	18.73%	1.14%	0.99%
B	-	-	-	0.06%	-	-	0.07%	-	-
Zr	4.73%	0.00%	-	19.45%	0.01%	0.00%	-	-	-

within the existing B2 precipitates. In FBB13 + 3.5 wt.% W however, the ratio of Al/Ni is almost 1.5, which could be a systematic discrepancy due to the much additional Al compared to Ni within the alloy system. For the α -Fe matrix, in FBB8 + 2 wt.% Hf and FBB8 + 2 wt.% Zr alloys, it is majorly enriched by Fe and Cr, which are over 70 at. % and ~12 at%, respectively. Al in the matrix also contributes ~6 at. %, which refers to the excessive amount of Al shown in Table 6, where the Al is actually ~3 at. % more than Ni. However, for FBB13 + 3.5 wt.% W, the excessive amount of Al compared to Ni is about 13 at. %, which could refer to the greatly reduced amount of Ni in the composition of FBB13 + 3.5 wt.% W, as shown in Table 6. The same phenomenon can also be observed within the B2 precipitates in FBB13 + 3.5 wt.% W alloy, where the amount of Al is about 11 at. % more than the amount of Ni. The reduced amount of Ni causes basically two results: First, the volume fraction of the B2-NiAl precipitates is much less in FBB13 + 3.5 wt.% W than in other two alloys. Second, the excessive amount of Al atoms remains in the lattice of the α -Fe matrix, which might bring slightly enhancement from the solid-solution strengthening mechanism. Another interesting observation for the FBB13 + 3.5 wt.% W alloy is that, the size of the B2-NiAl precipitates are varies, while some of the B2 precipitates have diameter ~80 nm, many of the B2 precipitates are actually remain an extremely small size (~5 nm) and well dispersed within the matrix.

Neutron/Synchrotron Diffraction

The neutron diffraction is majorly for the phase characterization of FBB8 + 2 wt.% Hf and FBB8 + 2 wt.% Zr alloys, and the synchrotron diffraction is for FBB13 + 3.5 wt.% W alloy. Figure 26(a) shows the full neutron diffraction patterns for both FBB8 + 2 wt.% Hf and FBB8 + 2 wt.% Zr

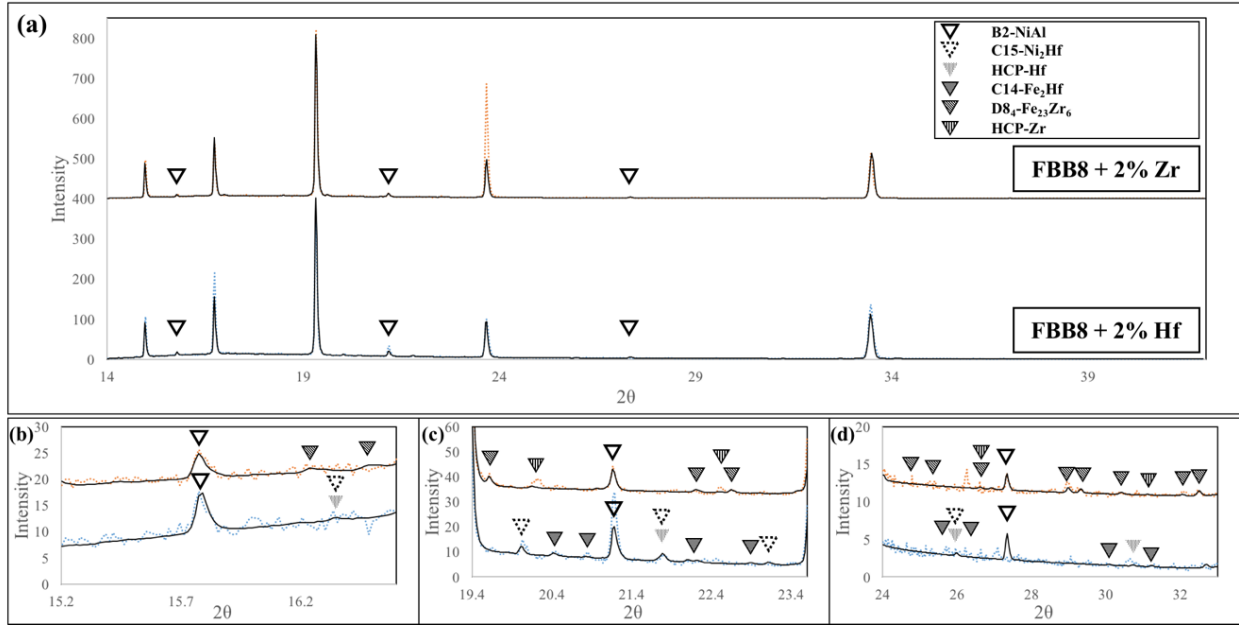


Figure 26. The neutron diffraction pattern for FBB8 + 2 wt.% Hf and FBB8 + 2 wt.% Zr at room temperature, where (a) the whole diffraction pattern, (b) the diffraction pattern from the 2θ of 15.2° to 16.6° , (c) the diffraction pattern from the 2θ of 19.4° to 23.6° , and (d) the diffraction pattern from the 2θ of 24° to 33° . The dashed line is the actual data collected from the diffraction experiment, and the solid line is the fitting. Major peaks with high intensities are overlap of the BCC and B2 peaks, which are the matrix (α -Fe) and the major strengtheners (B2-NiAl) of the alloys. Minor peaks are identified and labeled for the crystal structure of the white agglomerates in the alloys, which are C15-Ni₂Hf, HCP-Hf, and C14-Fe₂Hf in the FBB8 + 2 wt.% Hf alloy, and D₈₄-Fe₂₃Zr₆ and HCP-Zr in the FBB8 + 2 wt.% Zr alloy.

alloys at room temperature, Figure 26(b) (c) (d) are the minor peaks within the pattern shown in Figure 26(a), and Table 7 summarizes information that extracted from the ND pattern analysis. The major phases that can be identified from Figure 26(a) are the BCC phase (α -Fe) and B2 phase (B2-NiAl). Major peaks with high intensities are actually an overlap of BCC and B2 peaks, because of the high coherency between the matrix and the B2 precipitates. From the lattice parameters in Table 7, the lattice mismatch between the matrix and the B2 phase precipitates is only 0.08% for FBB8 + 2 wt.% Hf alloy, and 0.002% for FBB8 + 2 wt.% Zr alloy. One thing needs to be noted is that there are many small peaks that cannot be clearly identified from the peak fitting, suggesting that the white agglomerate could be a segregation of many different intermetallics that composed of different crystal structures, rather than one simple intermetallic compound. Based on the minor peaks identifications, the white agglomerates within FBB8 + 2 wt.% Hf alloy could be a combination of C15-Ni₂Hf, HCP-Hf, and C14-Fe₂Hf, and for FBB8 + 2 wt.% Zr alloy, the white agglomerates could be a combination of D8₄-Fe₂₃Zr₆ and HCP-Zr. Within the white agglomerate in FBB8 + 2 wt.% Hf alloy, HCP-Hf is the most abundant species, and the volume fraction of the C14-Fe₂Hf is about 1.5 times of the C15-Ni₂Hf. And within the white agglomerate in FBB8 + 2 wt.% Zr alloy, HCP-Zr is the most abundant, and the volume fraction of the D8₄-Fe₂₃Zr₆ is only ~1/10 of the HCP-Zr.

Figure 27 shows a synchrotron diffraction pattern for FBB13 + 3.5 wt.% W, and since the synchrotron measurement is done in transmission mode, the diffraction angle is much narrower than the neutron diffraction measurement, which is in reflection mode like conventional X-ray

diffraction. In Figure 27, a clear diffraction pattern for the α -Fe matrix can be easily observed, but other than the matrix, all the peaks for other phases are not very clear and well-defined, even for

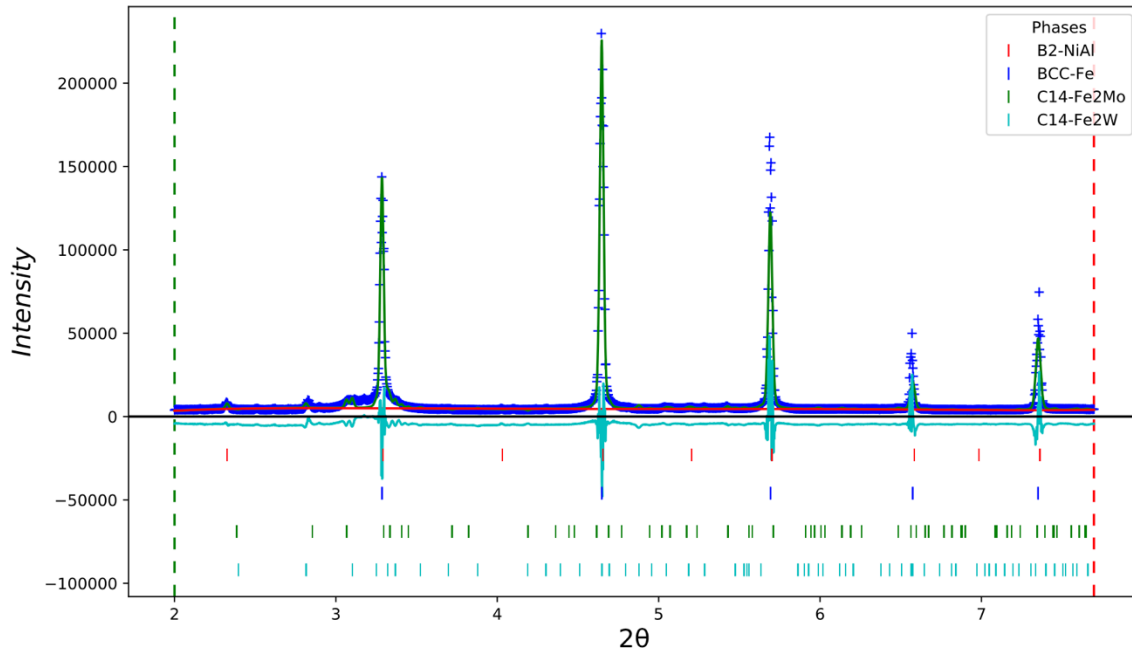


Figure 27. The synchrotron XRD pattern of FBB13 + 3.5 wt.% W alloy. Due to transmission measurement setup the 2θ range is only to $\sim 8^\circ$, however it is already enough for phase characterization. The major phases that can be identified are α -Fe, B2-NiAl, C14-Fe₂W, and C14-Fe₂Mo.

Table 7. Phases characterized from the fitting of diffraction patterns and their respective lattice constants and volume fractions

Alloy	Phase	Lattice Constant (Å)		Phase fraction (%)
		a	c	
FBB8 + 2 wt.% Hf	α -Fe	2.8873		76.62
	B2-NiAl	2.8896		21.88
	C15-Ni ₂ Hf	6.9103		0.16
	HCP-Hf	3.1729	5.1166	1.10
	C14-Fe ₂ Hf	4.9852	8.1119	0.24
FBB8 + 2 wt.% Zr	α -Fe	2.88532		84.92
	B2-NiAl	2.88527		14.28
	D8 ₄ -Fe ₂₃ Zr ₆	11.7157		0.06
	HCP-Zr	3.2436	5.1419	0.74
FBB13 + 3.5 wt.% W	α -Fe	2.8930		83.28
	B2-NiAl	2.8871		13.46
	C14-Fe ₂ W	4.8873	7.5384	1.71
	C14-Fe ₂ Mo	4.7703	7.6978	1.54

the B2 phase peaks. There are 4 major phases that can be identified by the synchrotron diffraction pattern analysis, which are α -Fe, B2-NiAl, C14-Fe₂W, and C14-Fe₂Mo. Surprisingly, although within the FBB13 + 3.5 wt.% W alloy system the amount of Ni has been greatly reduced compared to FBB8 alloys, the volume fraction of B2 phase still has 13%, only slightly lower than it presented in the FBB8 + 2 wt.% Zr alloy. On the contrary, the amount of C14-Fe₂W and C14-Fe₂Mo is not as much as designed, they have ~1.7 vol.% for C14-Fe₂W and ~1.5 vol.% for C14-Fe₂Mo, respectively. That is to say, the total amount of incoherent precipitates is roughly only 3.2 vol.%, which might not be able to bring great enhancement on the strength as well as creep resistance. The lattice mismatch between the α -Fe and B2-NiAl is 0.2%, which doubles the misfit compare to the misfit on FBB8 + 2 wt.% Hf alloy, and 100 times compared to the misfit on FBB8 + 2 wt.% Zr alloy. Usually the larger the lattice misfit, the smaller the particle size is [31], therefore among these all alloys FBB13 + 3.5 wt.% W has the smallest B2 precipitate, FBB8 + 2 wt.% Hf the second, and FBB8 + 2 wt.% Zr has the largest B2 precipitate, which briefly agrees with what had found in SEM images.

Discussion on Microstructures

What are those white particles/agglomerates, and why are them there within the microstructure of these three alloys? In the FBB8 + 2 wt.% Hf alloy system, 2 wt. % of Hf in the FBB8 system is only about 0.6 at. %, which is only slightly above the maximized solubility of Hf within α -Fe (0.51 at. % at ~1330 °C), therefore, it is possible that during the solution-treatment, most of Hf dissolved within the matrix and precipitated as particles in the aging process afterward, and the Hf atoms that are beyond the solubility deposit along the grain boundaries. Taking a closer look at the

elemental distribution shown in Table 6, it can be found that the Ni concentration within the white agglomerate regime is actually 4.3% higher than the Al concentration, making the Ni/Al ratio almost 3:2, which is not consistent with the 1:1 B2-NiAl Ni/Al ratio. The excessive Ni leads to an assumption that there might be intermetallic compounds majorly composed of Ni and Hf within that regime. The ratio of the Hf/Ni in this regime is $\sim 1-1.4$, indicating an excessive amount of Hf left, which can also be intermetallic compounds with other elements or just purely HCP-Hf. Figure 26(b) (c) (d) shows a detail comparison on the minor peaks in the FBB8 + 2 wt.% Hf ND pattern to the intermetallic compounds of Ni₂Hf, Fe₂Hf, and also Hf, though none of them perfectly match all the minor peaks with the ND pattern, these three intermetallic compounds show much higher matching compare to other possible phases. According to the GSAS fitting parameters, the concentration of these three phases are 0.16 vol.% for C15-Ni₂Hf, 0.24 vol.% for C14-Fe₂Hf, and 1.1 vol.% for HCP-Hf, respectively. HCP-Hf has the highest concentration compared to the rest two intermetallic compounds, showing that in fact, Hf does not mix well with other elements during the fabrication and the heat-treatment process.

In the situation of FBB8 + 2 wt.% Zr alloy, it has similar but more extreme scenario compared to the FBB8 + 2 wt.% Hf, since the solubility of Zr within Fe is extremely low. The ND pattern analysis showed that the minor peaks fit relatively well with D8₄-Fe₂₃Zr₆ and HCP-Zr respectively, instead of C14-Fe₂Zr. Analogous to the FBB8 + 2 wt.% Hf alloy, the fitting parameter from GSAS fitting shows that HCP-Zr has the concentration (0.74 vol.%) about one order higher than D8₄-Fe₂₃Zr₆ (0.06 vol.%), indicating the most of the white agglomerates could be majorly composed of the Zr residue, instead of Fe-Zr intermetallics. In the summary of the elemental distribution

shown in Table 6, the Al and Ni contents are almost identical in the white agglomerate regime, further support the above comprehension since there's no excessive amount of Ni or Al for the formation of other intermetallics. From current understanding of the Fe-Zr binary system [25], the appearance of $\text{Fe}_{23}\text{Zr}_6$ is not to be surprised, which is the most common intermetallic compound on the Fe side of phase diagram. Taking consideration of the extremely low solubility of the Zr in α -Fe, there's no doubt that most of the white agglomerates found in the microstructure of the FBB8 + 2 wt.% Zr alloy are located majorly to the grain boundaries. Moreover, unlike the FBB8 + 2 wt.% Hf alloy, there's no tiny white precipitates presented within the grains of the FBB8 + 2 wt.% Zr alloy. All the white agglomerates within the grains of the FBB8 + 2 wt.% Zr are micron-sized, and the distribution is more concentrated, suggesting that there's nearly no precipitation process happened during the aging process for the FBB8 + 2 wt.% Zr alloy.

Figure 28 shows a schematic illustrating the formation mechanisms for the microstructure of the FBB8 + 2 wt.% Hf and FBB8 + 2 wt.% Zr alloys. Since Hf and Zr has much higher melting temperatures compared to the Fe matrix, when cooling down, the intermetallics containing Hf/Zr are expected to solidify prior to the matrix. These Hf/Zr containing intermetallics form because of the Hf/Zr atoms are not solvable within the Fe, therefore when the α -Fe matrix solidifies, the Hf/Zr either segregated as large agglomerates, or being deposited at grain boundaries. In other words, these Hf/Zr containing intermetallics are being pushed out of the α -Fe grains, or being enveloped when the α -Fe grains solidify. For FBB8 + 2 wt.% Zr alloy, almost all the Zr atoms are already allocated to these Zr enriched agglomerates, due to lack of solubility within α -Fe matrix. However, for FBB8 + 2 wt.% Hf alloy, some of the Hf atoms are actually encaged within the α -Fe lattice

because Hf has small amount of solubility in the α -Fe. Afterward when the alloys go through the aging process, the Hf atoms, as well as B2-NiAl, start to precipitate out from the matrix and forming fine, homogenously distributed particles dispersed within the matrix. These Hf containing

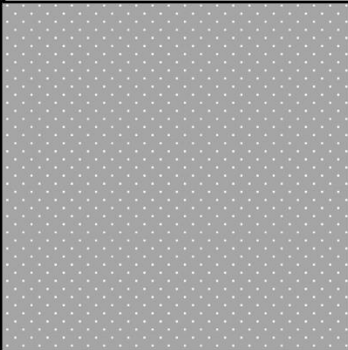
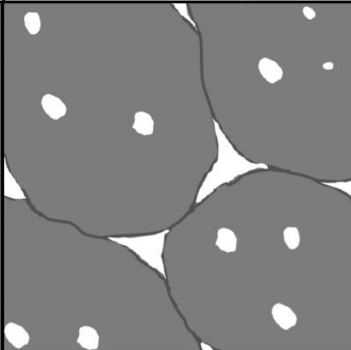
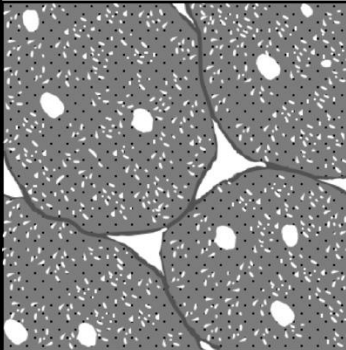
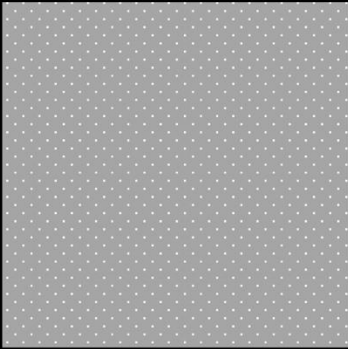
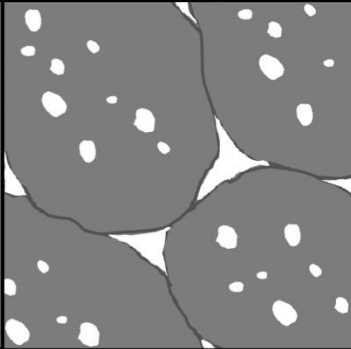
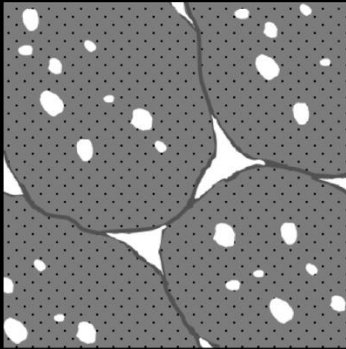
	Hf/Zr intermetallics solidified as clusters	The α -Fe matrix solidified, and insoluble Hf/Zr intermetallics deposit at grain boundaries (or enveloped within grains)	During the aging process, the supersaturated Hf precipitates out from the α -Fe matrix
FBB8 + 2% Hf alloy			
FBB8 + 2% Zr alloy			

Figure 28. Schematic illustrating the formation of the microstructure of the FBB8 + 2 wt.% Hf and FBB8 + 2 wt.% Zr alloys. Since the majority of the Hf, Zr, and their respective intermetallic compounds are insoluble within the α -Fe matrix. During the solidification of the matrix these insoluble clusters are deposited at grain boundaries, and/or enveloped within grains as a large agglomerate.

particles could actually be a strengthener as B2-NiAl is. However, limited quantity of the particles due to lack of enough solubility, as well as serious coarsening due to its nature of incoherency to the α -Fe matrix, these features sentence FBB8 + 2 wt.% Hf alloy incapable of being greatly strengthen the original FBB8. As a result, both addition of Hf and Zr do not help in improving the strength of the FBB8 alloy, neither are they forming the desirable $L2_1$ phase, nor are they forming other intermetallic particles that are adequate to be a strengthener.

For FBB13 + 3.5 wt.% W alloy however, the C14-Fe₂W/Fe₂Mo is precipitate that is designed to exist within the microstructure based on the phase diagram shown in Chapter 2. On the contrary, the B2-NiAl presents in an alternative way, where most of the B2-NiAl are only ~5 nm, and only limited amount of B2-NiAl coarsens to over 80 nm, which is not presented within the microstructure of FBB8 + 2 wt.% Hf and FBB8 + 2 wt.% Zr alloys. FBB13 + 3.5 wt.% W alloy has only 3 wt.% of Ni in its alloy composition, much lower than 10 wt.% Ni designed for FBB8 + 2 wt.% Hf and FBB8 + 2 wt.% Zr alloys. Therefore, lack of Ni causes the overall volume fraction of B2-NiAl in FBB13 + 3.5 wt.% W alloy less than the other two alloys, as well as difficulties in coarsening. For the 100 hours aging period, almost every single B2-NiAl within FBB8 + 2 wt.% Hf and FBB8 + 2 wt.% Zr alloys coarsens to ~100 nm in diameter, however, for the B2-NiAl precipitate within the FBB13 + 3.5 wt.% W alloy system, it is much more difficult to coarsen, due to lack of resources and perhaps wider range for diffusion. Therefore, it is observable that there are limited amount of ~80 nm scale B2-NiAl particles within the microstructure of FBB13 + 3.5 wt.% W alloy (< 1%), and the ~5 nm size B2-NiAl particles are ~13%, homogenously distributed within the matrix. The size difference for the B2-NiAl within FBB13 + 3.5 wt.% W alloy and the

other two alloys brings a critical conclusion, that the B2-NiAl within FBB13 + 3.5 wt.% W alloy strengthens the alloy by dislocation-shearing mechanism, and the B2-NiAl within the other two alloys strengthens by dislocation-climbing mechanism.

As shown in the microstructure of all three alloy systems, the volume fraction and the particle (precipitate) size is mutually dependent, while the volume fraction of the intermetallic phase goes up, its precipitate size grows larger as well. It is difficult to control the precipitate size within a certain value, therefore causing higher volume fraction ends up with larger number of particles, which is the original goal of this research. Instead, if the volume fraction goes too high, the precipitate size goes extremely large as well, and the inter-particle spacing goes larger, with the reduce of the strengthening. This effect is especially prominent to the incoherent particles, since comparing to the coherent particles, incoherent particles usually have much higher coarsening rate due to their incoherent interface with the matrix. As a result, the best strategy to introduce incoherent particles into an alloy system as a strengthener should be including many types of precipitates, with low volume fraction for each of them, in order to limit their coarsening rate and maximizing the total number of these particles.

Overall, from the microstructural characterization, it looks like only FBB8 + 2 wt.% Hf and FBB13 + 3.5 wt.% W alloys have apparent changes from the original FBB8 alloy in the aspect of microstructure. FBB8 + 2 wt.% Zr alloy has well dispersed B2-NiAl precipitates, however the Zr additions do not homogeneously dispersed into its matrix. Instead, these Zr contained intermetallic compounds dispose majorly along the grain boundary or segregated as a large agglomerate, either way do not help in enhancement on the overall strength. Therefore, for the later mechanical tests,

the focus will be on the FBB8 + 2 wt.% Hf and FBB13 + 3.5 wt.% W alloys, rather than all three of the proposed alloys. Among these three alloys, FBB8 + 2 wt.% Zr alloy has the highest volume fraction for precipitates, and both FBB8 + 2 wt.% Hf and FBB13 + 3.5 wt.% W alloy has lower volume fraction (B2 + Laves phases particles, ~14%). Mechanical test results will be shown and discussed with the parameters shown in Table 8 later, in order to connect the microstructure with the mechanical properties.

Table 8. Microstructural parameters combined with both SEM and diffraction analysis

Alloy	Phase	Volume fraction (%)	Diameter (nm)
FBB8 + 2 wt.% Hf	α -Fe	75.6	-
	B2-NiAl	14	90
	Others	0.4	1400
FBB8 + 2 wt.% Zr	α -Fe	84	-
	B2-NiAl	16	122
	Others	-	-
FBB13 + 3.5 wt.% W	α -Fe	86	-
	B2-NiAl	13	5
	Laves Phases	1	1914

CHAPTER FIVE

STRENGTH TESTS AND CALCULATIONS

Compression Tests at Room Temperature

Figure 29 shows the room temperature compression test result for FBB8 + 2 wt.% Hf, FBB8 + 2 wt.% Zr, and FBB13 + 3.5 wt.% W alloys. From the total volume fraction of precipitates observed from the microstructural characterization within the previous chapter, it is predicted that FBB8 + 2 wt.% Hf could have the best strength among these three alloys, due to a relatively smaller precipitate size, and the FBB13 + 3.5 wt.% W alloy could have the worst strength, because of much lower precipitate volume fraction. The compression test result shows that FBB13 + 3.5 wt.% W alloy does have the worst strength, with only ~690 MPa. FBB8 + 2 wt.% Hf has strength ~1050 MPa, which is almost 360 MPa higher than FBB13 + 3.5 wt.% W alloy. Surprisingly, FBB8 + 2 wt.% Zr has the highest strength among these three alloys, which is ~1240 MPa, and nearly the same elongation compared to the FBB8 + 2 wt.% Hf alloy. The volume fraction of the B₂-NiAl precipitates within FBB8 + 2 wt.% Zr alloy is 2% higher than within FBB8 + 2 wt.% Hf alloy, however its precipitate diameter is ~36% larger than the B₂-NiAl within FBB8 + 2 wt.% Hf alloy, that is to say, the inter-particle spacing is also ~30% larger, which might cause a higher loss on the strength. On the contrary, the compressive yield strength of FBB8 + 2 wt.% Zr alloy is ~190 MPa higher than the strength of FBB8 + 2 wt.% Hf alloy. The reason will be discussed and discovered in the later paragraphs.

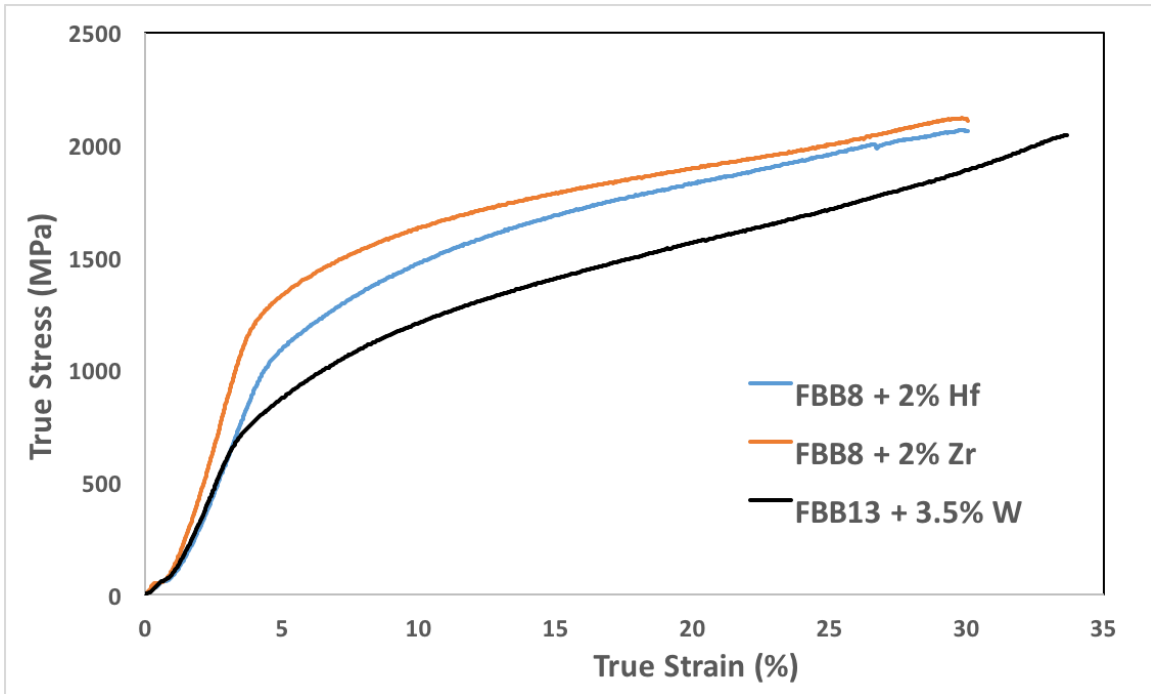


Figure 29. The compression test for FBB8 + 2 wt.% Hf, FBB8 + 2 wt.% Zr, and FBB13 + 3.5 wt.% W alloys, performed at room temperature. The FBB13 + 3.5 wt.% W alloy has relatively lower yield strength compared to the other two alloys, but slightly better ductility. Surprisingly, FBB8 + 2 wt.% Hf alloy has lower yield strength than the FBB8 + 2 wt.% Zr alloy.

Tension Tests at 700 °C

Tension tests are performed on FBB8 + 2 wt.% Hf and FBB13 + 3.5 wt.% W alloys only, because of both have the well dispersed secondary precipitates, which is able to bring additional strengthening rather than the existing B2-NiAl precipitates. The true stress-true strain curve is shown in Figure 30, and the numbers of yield strength, ductility, as well as toughness are summarized in Table 9. Not to surprise that FBB13 + 3.5 wt.% W alloy has a lower yield strength but better ductility at 700 °C. Its 700 °C strength is roughly 45 MPa lower than FBB8 + 2 wt.% Hf alloy, but ductility is 6% larger. Toughness-wisely FBB8 + 2 wt.% Hf and FBB13 + 3.5 wt.% W alloys do not have much difference, both of them has roughly $2.5 \times 10^7 \text{ J/m}^3$ toughness, and FBB13 + 3.5 wt.% W is slightly higher. Since for FBB13 + 3.5 wt.% W, the overall volume fraction of the precipitates is less than within FBB8 + 2 wt.% Hf alloy, it is difficult to conclude that the increase on such a small amount of toughness is contributed from the trade-off of losing strength or replacing the coherent precipitate with incoherent precipitate. The differences between the strength and ductility of FBB8 + 2 wt.% Hf and FBB13 + 3.5 wt.% W alloy is more close to a fair trade-off, since the overall toughness does not increase significantly.

Table 9. Mechanical properties obtained from the 700 °C tension tests

	Yield Strength (MPa)	Ductility (%)	Toughness (J/m³)
FBB8 + 2 wt.% Hf	200	20	2.80E+07

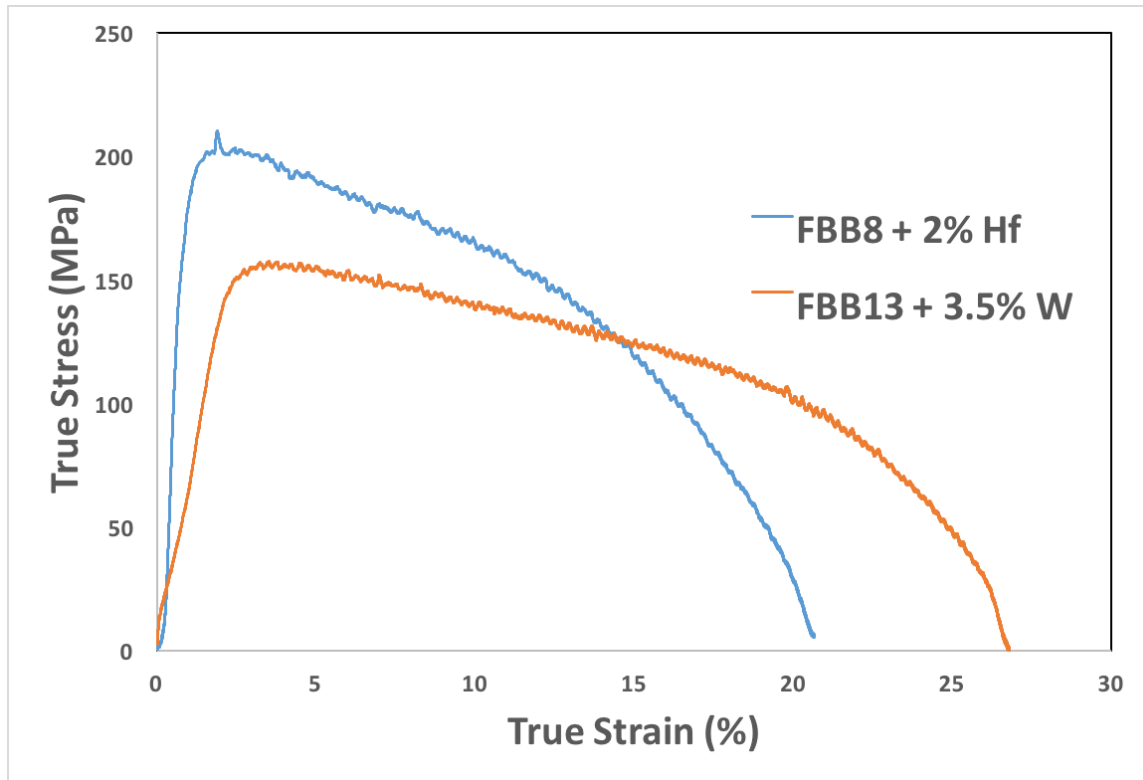


Figure 30. The tensile test for FBB8 + 2 wt.% Hf and FBB13 + 3.5 wt.% W alloys, performed at 700 °C. The FBB13 + 3.5 wt.% W alloy has relatively lower yield strength compared to FBB8 + 2 wt.% Hf alloy, but much greater elongation (or ductility) at 700 °C.

Calculation for Strength

Strengths of the FBB8 + 2 wt.% Hf, FBB8 + 2 wt.% Zr, and FBB13 + 3.5 wt.% W alloys are summarized in Table 10. The strengths contributed from various mechanisms are listed, and the basic assumptions for the calculations are (1) generally the B2-NiAl precipitate is coherent to the α -Fe matrix, therefore calculations are based on the shearing mechanisms, and (2) the Laves phases precipitates are incoherent to the α -Fe matrix, and the calculations are based on the climbing mechanism. For the assumption (1), since within FBB13 + 3.5 wt.% W alloy the size of B2-NiAl precipitates are small, therefore assuming them as coherent particle does not have problems. On the contrary for FBB8 + 2 wt.% Hf and FBB8 + 2 wt.% Zr alloys, the size of B2-NiAl precipitates is already large enough to possess incoherent interface between the precipitate and the matrix, therefore, the calculation for FBB8 + 2 wt.% Hf and FBB8 + 2 wt.% Zr, B2-NiAl precipitates are counted as incoherent particles.

From Table 10 it is shown that FBB8 + 2 wt.% Hf has the best strength among the three alloys, majorly due to its highest volume fraction for the B2-NiAl precipitates. The overall volume fractions for precipitates within the FBB8 + 2 wt.% Zr and FBB13 + 3.5 wt.% W alloys however, are roughly the same (~16%), but their respective calculated strength are different, because of the majority of the B2-NiAl precipitates within FBB13 + 3.5 wt.% W alloys are coherent particles, with much smaller size and therefore strengthen the alloy a little bit less. The 1% of incoherent particles within FBB13 + 3.5 wt.% W alloy provides only 18.6 MPa strength increment in the current microstructure configuration, majorly due to its huge size (1.9 μm). Large size particles

are not able to build a dense wall to impede the dislocations from free moving, as a result, the overall strengthening from the incoherent particles for FBB13 + 3.5 wt.% W alloys is weak,

Table 10. Contributions of different mechanisms in strength increment

	Coherent			Incoherent	Net Increment
	Coherency	Order	Modulus	Orowan	
FBB8 + 2 wt.% Hf	0	0	0	971.47	971.47
FBB8 + 2 wt.% Zr	0	0	0	860.29	860.29
FBB13 + 3.5 wt.% W	87.32	613.90	26.31	18.63	746.16

because of the combination of low volume fraction and large particle size. Sun *et al.*'s research [24] on materials with also coherent B2 precipitate and incoherent Laves phase precipitates, the calculation on strengthening also shows that the contribution from order strengthening is almost 10 times larger than other mechanisms. That is to say, the major advantage for the coherent B2-NiAl precipitate on strengthening is the difficulty in formation of new faces, instead of the lattice mismatch or modulus mismatch between the precipitate and the matrix. On the other hand, in Sun *et al.*'s research [24], the Laves phase has 6.8 vol.% with ~18 nm diameter, and is able to provide ~200 MPa strength increment as incoherent particles. However, in the microstructure of FBB13 + 3.5 wt.% W alloy the Laves phase particles are neither small nor many, as a result provide only 18.6 MPa as strength increment.

Discussion on Strength

The mechanical tests on 700 °C show that replacing the coherent precipitates by incoherent precipitates does not lead to significant enhancement on toughness. The FBB13 + 3.5 wt.% W alloy has slightly better toughness, by trading off the strength. The overall volume fraction of the FBB13 + 3.5 wt.% W alloy is roughly 14 vol.%, slightly less than FBB8 + 2 wt.% Hf alloy (~ 15 vol.%), therefore if we consider all these precipitates are incoherent, their overall strength increments for both alloys should be similar. However, in the comparison between the two alloys, the strength of the FBB13 + 3.5 wt.% W alloy is only 75% of the strength of the FBB8 + 2 wt.% Hf alloy. This huge discrepancy is majorly due to the extremely small size of the B2-NiAl within the FBB13 + 3.5 wt.% W alloy, which is supposed to be coherent. The loss of the strength is compensated by only 6% of toughness, the trade-off is not really cost-effective. From what had shown in the last section on microstructural characterization, the 1 vol.% of incoherent Laves phase Fe₂W/Fe₂Mo particles within FBB13 + 3.5 wt.% W alloy might not be able to provide enough strengthening, due to its huge particle size (1.9 μm) and wide inter-particle spacing. Therefore, the only effective amount of precipitate within FBB13 + 3.5 wt.% W alloy might only 13 vol.%, and these 13 vol.% of particles strengthen the alloy by the mechanism of dislocation shearing, instead of dislocation-climbing as shown in FBB8 + 2 wt.% Hf alloy.

CHAPTER SIX

CREEP TESTS AND CALCULATIONS

Tensile Creep Tests at 700 °C

Figure 31 shows creep curve for the full-life creep test on FBB13 + 3.5 wt.% W alloy at 700 °C, with applied stress 70 MPa. Figure 32 shows the creep curve for the stress jump test on FBB13 + 3.5 wt.% W alloy at 700 °C, with applied stresses 30 MPa, 37 MPa, and 50 MPa, respectively. The steady-state creep rate is summarized in Table 11, and the threshold stress is calculated by the slope of the plot $\ln\dot{\epsilon}$ vs. $\ln(\sigma - \sigma_{th})$, with $n = 4$ [22] (Figure 33). The threshold stress 16.38 MPa is very small compared to many other FBB series materials such as FBB8 + 2% Ti alloy (186 MPa), suggesting that its precipitates do not contribute enough creep resistance at working temperature 700 °C. Figure 31 shows a clear three stages creep curve, with the sample failed within 6 hours, suggesting that 70 MPa is too high for a normal creep. Compared with the tension tests performed at 700 °C, 70 Mpa is almost half of the yield strength at 700 °C, which might be an over-stress for a conventional creep test (usually with stress ~0.1 - 0.2 yield strength), in Figure 32, the stress jump test for all three stresses reach the steady state, and therefore their steady-state creep rate can be obtained. For 30 MPa it takes roughly 12 hours to reach steady-state, 37 MPa takes roughly 8 hours, and for 50 MPa it only takes less than 3 hours. In Figure 33 however, the data point of 30 MPa shows slightly off from the fitting line (the dotted line), indicating that the creep at 30 MPa might actually be dominant by other creep mechanism, instead of the climbing mechanism.

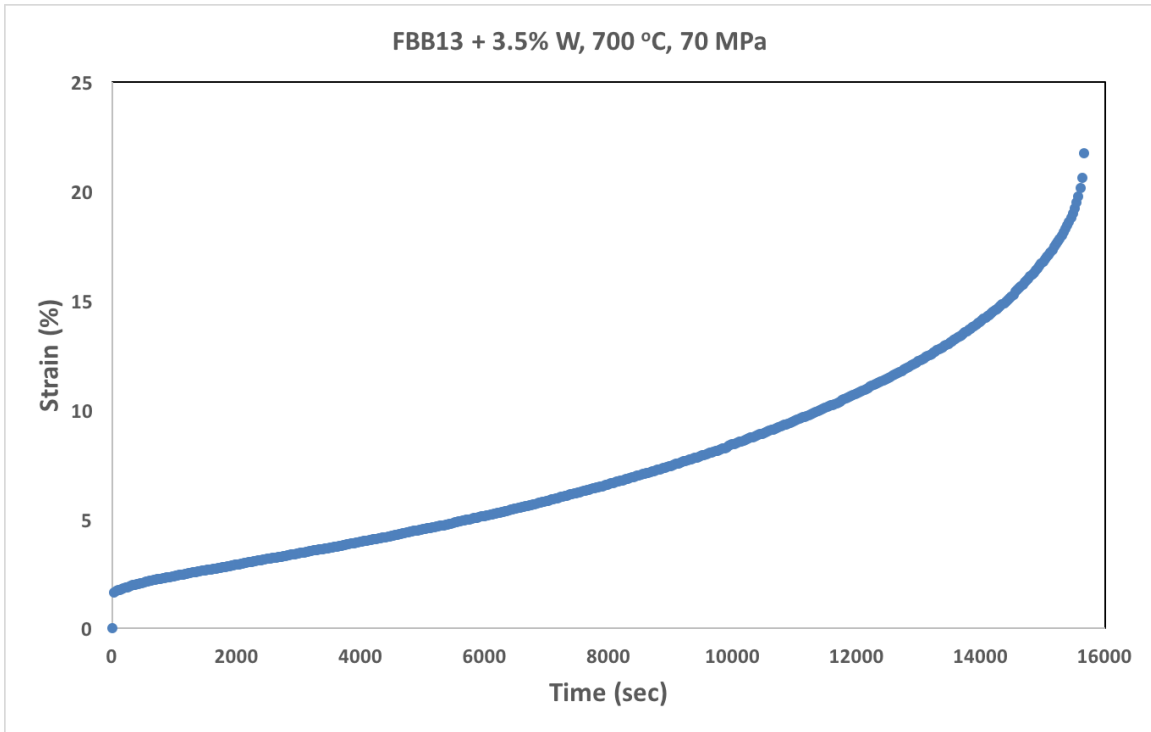


Figure 31. Creep curve for FBB13 + 3.5 wt.% W alloy, tested with applied stress 70 MPa, at 700 °C. The creep curve shows clear three creep stages, takes roughly 1000 seconds to steady-state, and another 5000 seconds to the third stage of creep where the creep rate starts to increase over time.

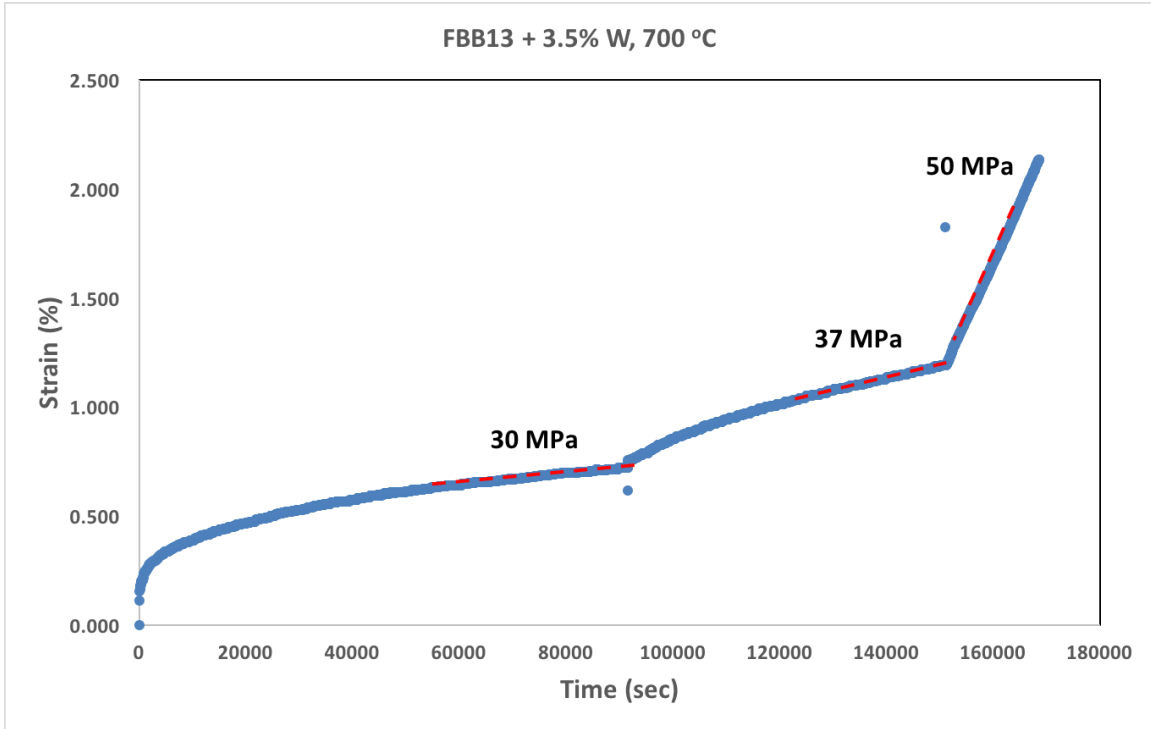


Figure 32. The creep curve for creep jump test on FBB13 + 3.5 wt.% W alloy, tested with applied stress 30 MPa, 37 MPa, and 50 MPa at 700 °C.

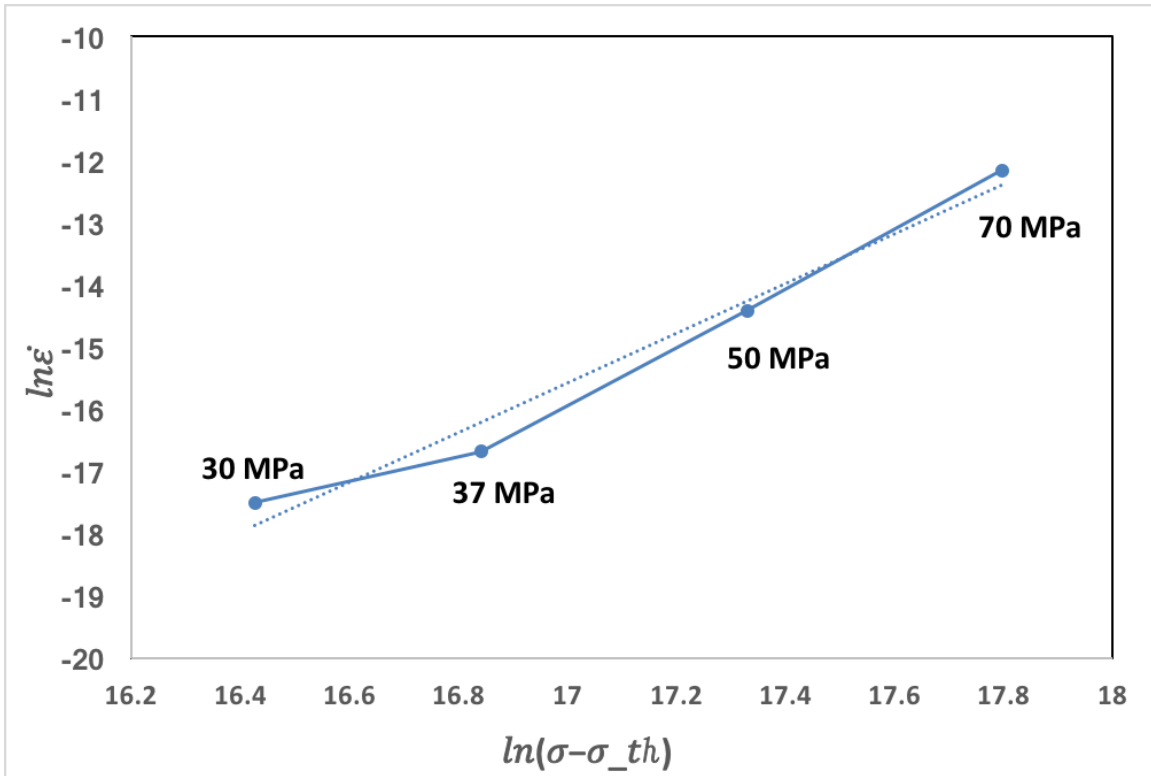


Figure 33. The plot of $\ln \dot{\epsilon}$ vs. $\ln(\sigma - \sigma_{th})$, where the $n = 4$ is assigned for the fitting of the threshold stress σ_{th} . The σ_{th} is 16.38 MPa. The point of 30 MPa is actually not follow well with neither the fitting line nor the straight line formed by the other three data points, indicating another creep mechanism might be dominating the creep at 30 MPa.

Table 11. Applied stress and the corresponding creep rate for FBB13 + 3.5 wt.% W alloy creep at 700 °C

Applied Stress (MPa)	Creep Rate (/s)
70	5.24892E-06
50	5.51684E-07
37	5.72001E-08
30	2.5025E-08

Modeling for Creep

Figure 34 shows the fitting of the creep curve for FBB13 + 3.5 wt.% W alloy, tested with applied stress 70 MPa at 700 °C, with the prediction from the model, and the fitting parameters are already summarized in Table 4. As shown in Figure 34, the prediction curve cannot fit well with the experimental data. Due to the extremely small particle size of B2-NiAl, the shearing mechanism is supposed to be the major strengthening mechanism for the back stress, however, the calculated shearing back stress in the model is simply too high, which does not fit with the actual situation. The major reason that shearing mechanism equation does not fit is because the Eq. (22) does not scale with creep strain, which most of other equations in this model do. As a consequence, for example, for B2-NiAl with diameter of 5 nm, the shearing mechanism simply provide more than 80 MPa back stress, which has already higher than the apply stress 70 MPa, making the dislocation component of strain rate as 0 from the very beginning. Therefore, although the B2-NiAl is no doubt

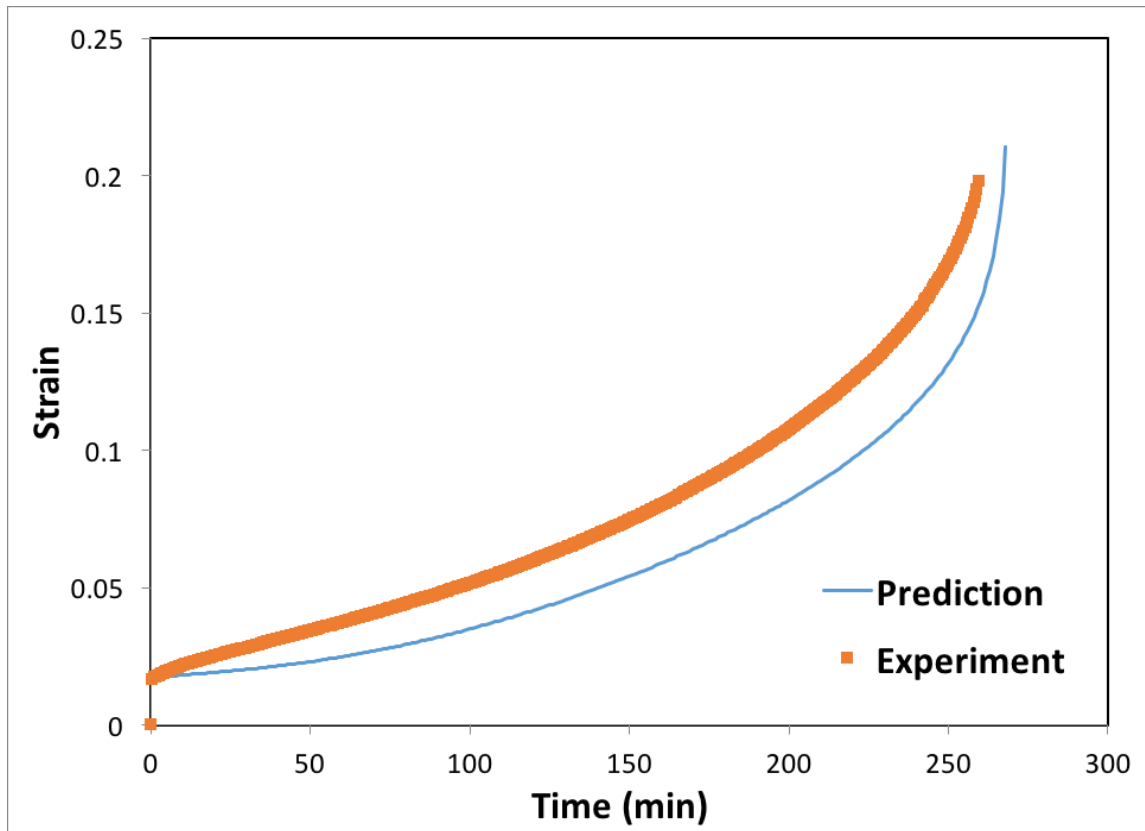


Figure 34. The comparison between the creep curve for FBB13 + 3.5 wt.% W alloy, tested with applied stress 70 MPa at 700 °C, with the prediction from the model. Due to the nano-sized B2-NiAl precipitates, the inter-particle spacing is extremely small, largely slowing down the creep rate.

a coherent particle, currently the model regards it as incoherent particle, calculating its back stress with the Orowan bowing mechanism.

In Figure 35 the major discrepancies between the prediction curve and the experimental curve is the relatively long and stable steady-state stage, where in the experimental data the steady-state stage lasts much shorter. Also, it can be clearly seen that the prediction on the strain rate on primary creep starts slower than the actual data. This extremely low primary stage creep rate, and longer steady-state stage, are majorly due to the extremely small B2-NiAl particle size, as well as smaller inter-particles spacing. As a result, the beginning of the creep the dislocation need to go through a much dense barricade, which result as a much higher strength, therefore ends up as a much slower creep rate. Figure 36 shows the stresses evolution during the creep process. Within the whole process the effective stress keeps higher than the latter two stresses, makes the whole creep process always affected by the dislocation-precipitate interaction, proved that at 700 °C, 70 MPa, the dislocation climb is the dominant mechanism. The back stresses, primarily contributed from the climbing mechanism, has the three stages over time similar to the creep strain itself, basically due to the climbing mechanism scales with the creep strain, as shown in Eq. (23). In fact, in this model the effective stress, and back stress, are both function of the creep strain, therefore, curves of effective stress, and back stress share the similar for as the creep strain vs. time curve, where there are clear three stages, and the secondary stage is the slowest one. The total stress however, does not behave like a creep curve, instead has a U-shape indicating that during the secondary stage of the creep, the total stress is the minimum, leads to the slowest creep strain rate, as shown in Figure

35. In this configuration however, the dislocation stress is higher than both back stresses for respective precipitates (B2 and Laves phase). Since the initial creep strain rate ($\sim 1 \times 10^{-5}/s$) is

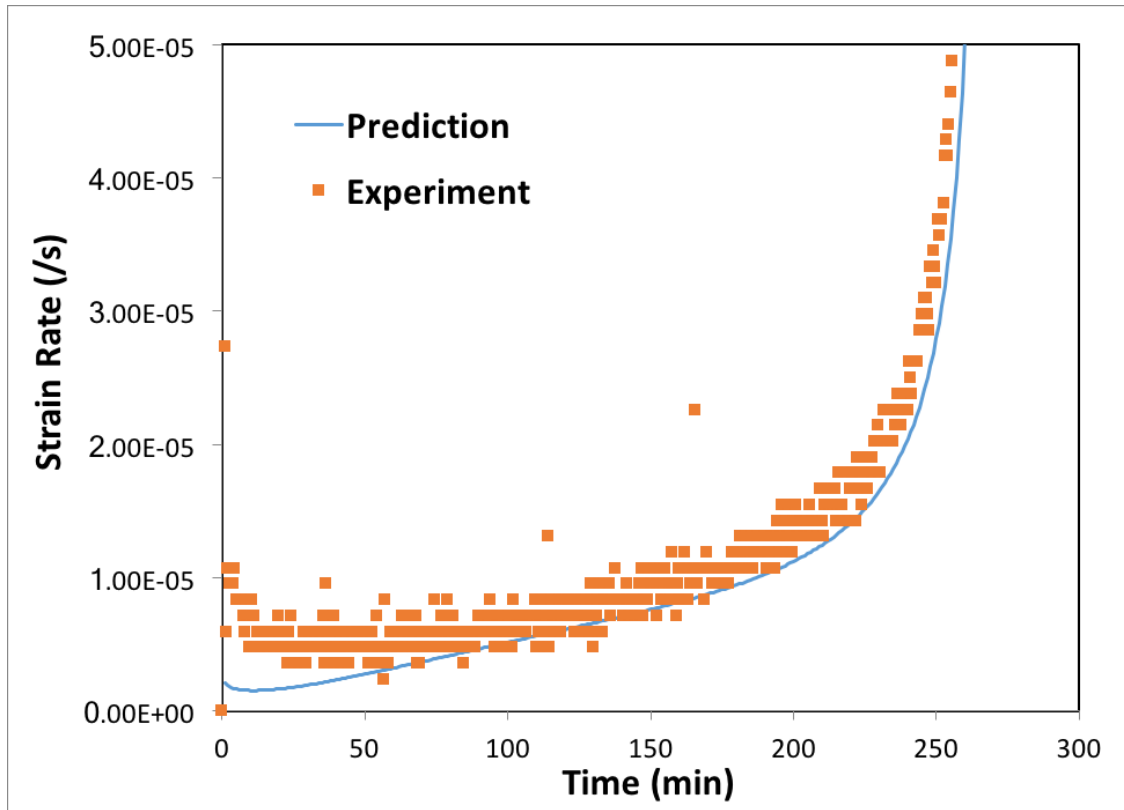


Figure 35. The comparison between the creep rate for FBB13 + 3.5 wt.% W alloy, tested with applied stress 70 MPa at 700 °C, with the prediction from the model. The prediction on the primary stage (the first 5 minutes where the creep rate hasn't drop to the lowest point) is roughly 2 times slower than the experimental data, which is due to the extremely small inter-particle spacing.

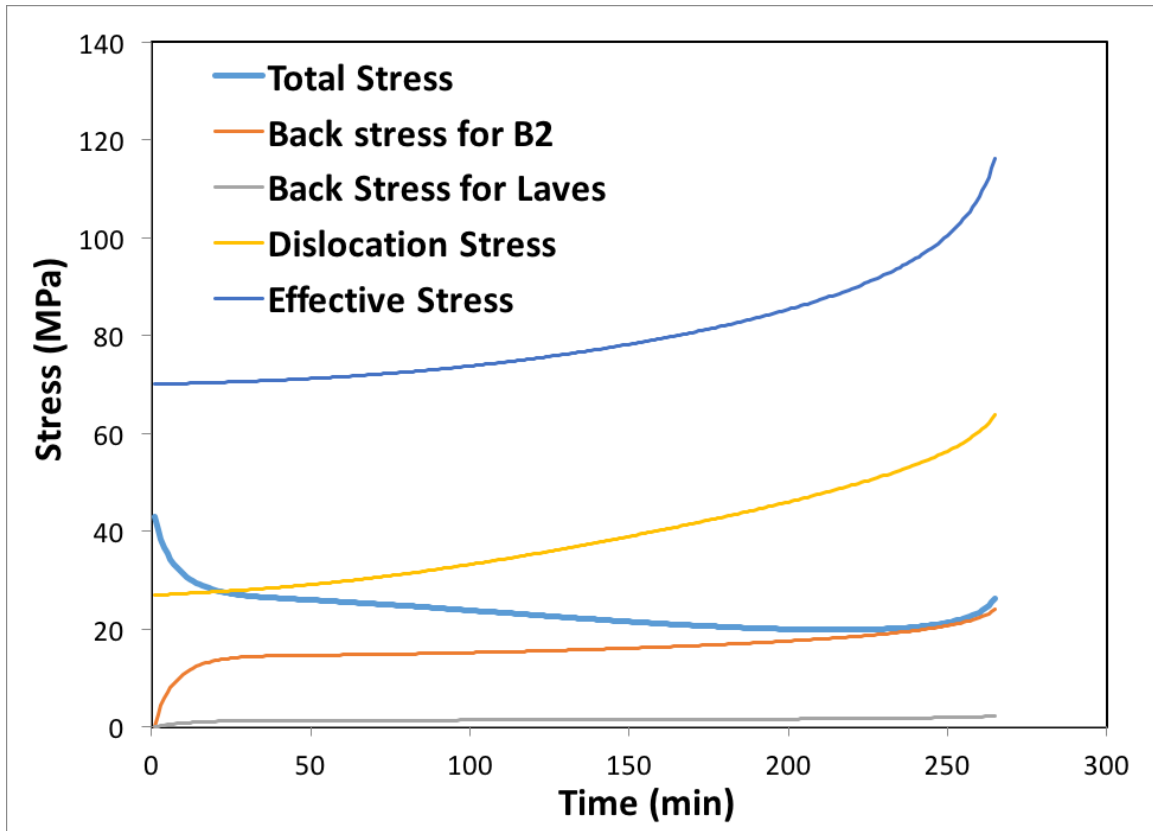


Figure 36. The three stresses related to the dislocation-precipitate interaction in the calculation of the creep. For the creep test at 70 MPa, the effective stress is always higher than the sum of the rest of two stresses, therefore the dislocation-precipitate mechanism has always activated during the whole creep process. Back stresses for precipitates contribute depending on their respective volume fraction, where B2-NiAl contribute the most amount three kinds of particles.

a function of fitting parameter A and the estimated initial dislocation density, the lower the initial dislocation density is, the smaller the fitting parameter A becomes. In the fitting process it is shown that if fitting parameter A is smaller than 0.01, the predictions on lower stresses (50 MPa, 37 MPa, and 30 MPa) using the same configuration deviates more from the experimental data. The overall fitting parameter for the current configuration is listed in Table 4.

Figure 37 shows the creep rate components for 70 MPa, 50 MPa, 37 MPa, and 30 MPa. As shown in Figure 37(a) (b), at 70 MPa and 50 MPa, the dislocation component is much higher than the diffusion component, therefore the creep rate of dislocation component is dominating the whole creep rate. However, start from 37 MPa, as shown in Figure 37(c), the dislocation component cannot last for the whole process, and then the slowest creep rate becomes the creep rate of the diffusion component. The reason why the dislocation component suddenly stops is because after certain amount of time, the effective stress can no longer be higher than the sum of other stresses, therefore the dislocation creep rate equals to zero, as shown in the Eq. (20). Figure 37(d) demonstrates why the experimental creep rate for 30 MPa does not fit with the linear approximation of the other three data points, because at 30 MPa, the creep rate has been dominated by the diffusion mechanism. However, at 37 MPa the creep rate is supposed to be dominated dislocation mechanism, but the modeling result show the opposite. Current results are already the best fit, and it still cannot make the creep rate at 37 MPa a proper combination of both mechanisms. Perhaps it indicates that current fitting can still be improved, or the model itself has a shortcoming when two of the components contribute similar amount of creep rate.

Figure 38 shows the particle size evolution for both B2-NiAl and Laves phase precipitates in the modeling of 70 MPa, where the Laves phase coarsening parameters are evaluated and the B2-NiAl

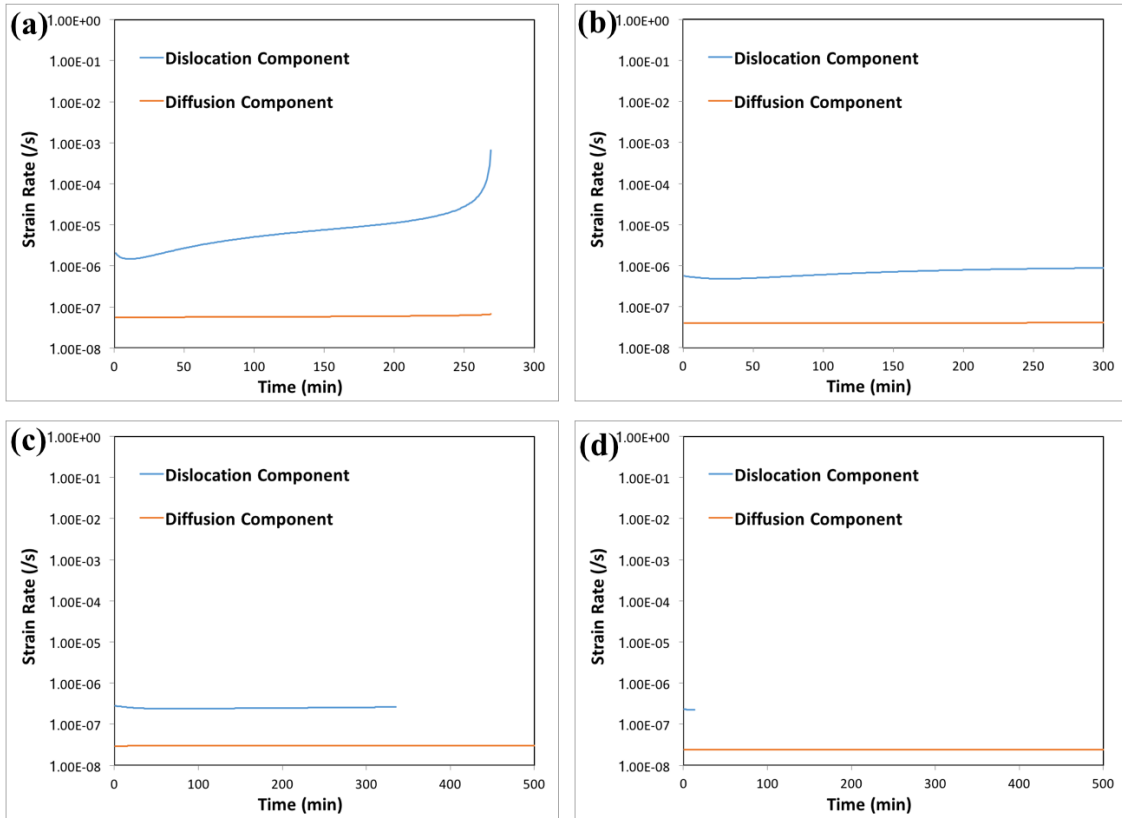


Figure 37. The respective creep rate components for all 4 creep tests on (a) 70 MPa, (b) 50 MPa, (c) 37 MPa, and (d) 30 MPa. The dislocation component keeps dropping until 37 MPa, it suddenly disappeared, majorly due to the effective stress starts to be lower than the sum of back stresses and dislocation stress. At 30 MPa this same situation happens much faster than at 37 MPa.

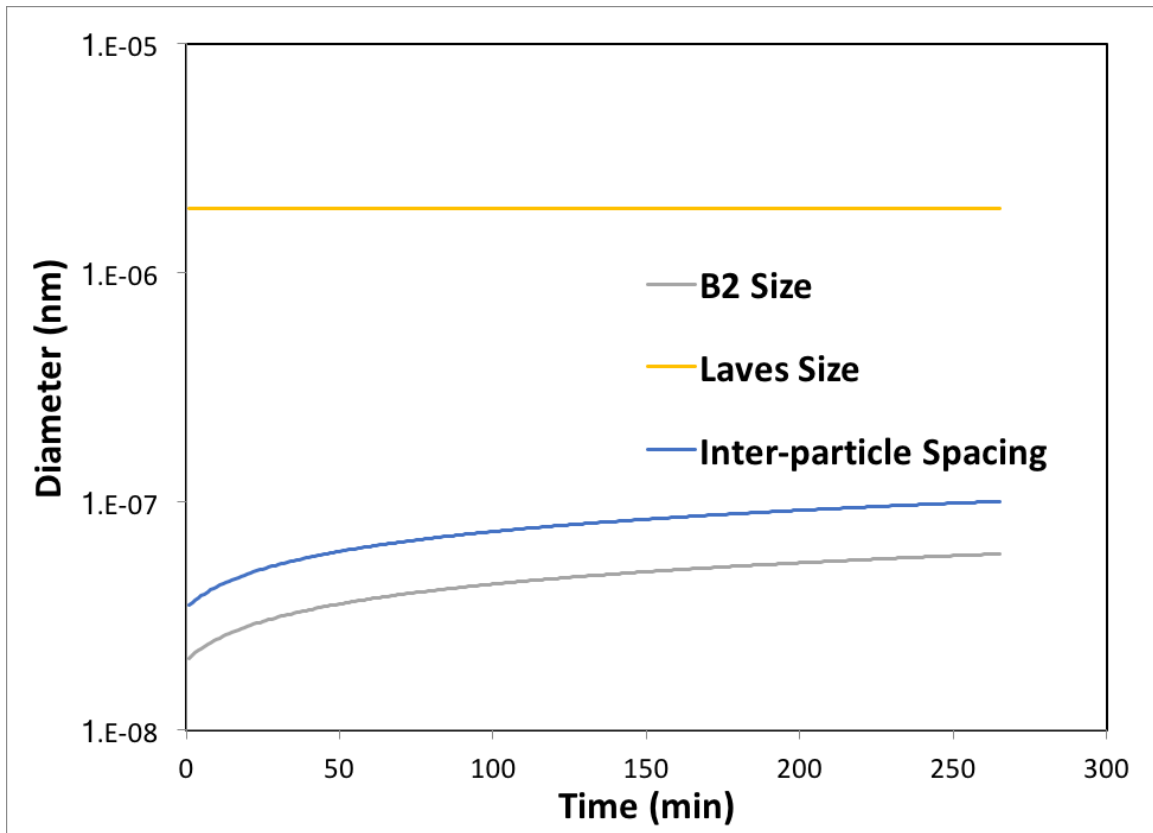


Figure 38. The coarsening of both B2 phase precipitate and Laves phase precipitate, where the Laves phase precipitate coarsening kinetic parameters are estimated. The coarsening B2-NiAl is much faster Laves phase precipitate, where within 250 mins, the size doubles.

coarsening parameter is based on Sun *et al.*'s data [8]. The Laves phase is pretty stable during the modeling process, and the B2-NiAl coarsens a lot, within 250 minutes the size has already doubled. Since the low volume fraction as well as relatively large particle size, the coarsening of Laves phase particle cannot cause any meaningful effect to the inter-particle spacing. As a result, the inter-particle spacing majorly follows closely with the size of the B2-NiAl.

Figure 39 shows the comparison between the experimental data and the calculation with model includes diffusional mechanisms. As shown in the last paragraph, the diffusional mechanisms provide roughly $2 \times 10^{-8}/s$ strain rate as the baseline of the total creep strain rate, that is to say, even the dislocation related mechanisms are not activated, it still creeps with the rate of $2 \times 10^{-8}/s$. Generally, the diffusional creep strain rate steadily increases over time, because it also scales with creep strain. Figure 39 also shows that apparently since for the diffusional mechanisms the applied stress is not a factor to affect the creep rate, changing the applied stress from 30 MPa to 37 MPa cannot double the creep rate as observed from the experimental data. That is to say, when the transition from dislocation mechanisms to the diffusional mechanisms happens, their joint effect cannot be described simply as this model did. The steady-state creep rate for 50 MPa fits pretty well, but the steady-state creep rate for 70 MPa is 1/3 of the experimental result. Since for these two applied stresses, the dislocation component is dominating, it suggests that for higher stresses the resistance is higher in calculation than in reality. As shown in previous paragraph, the major reasons could be the extremely small inter-particle spacing, as well as inaccurate back stress for the coherent particles. Since the particle coarsens during the process, at

higher stresses the deformation rate is much higher than the coarsening rate, therefore in the calculation it cannot be matched and deviates more and more as the applied stress goes higher and

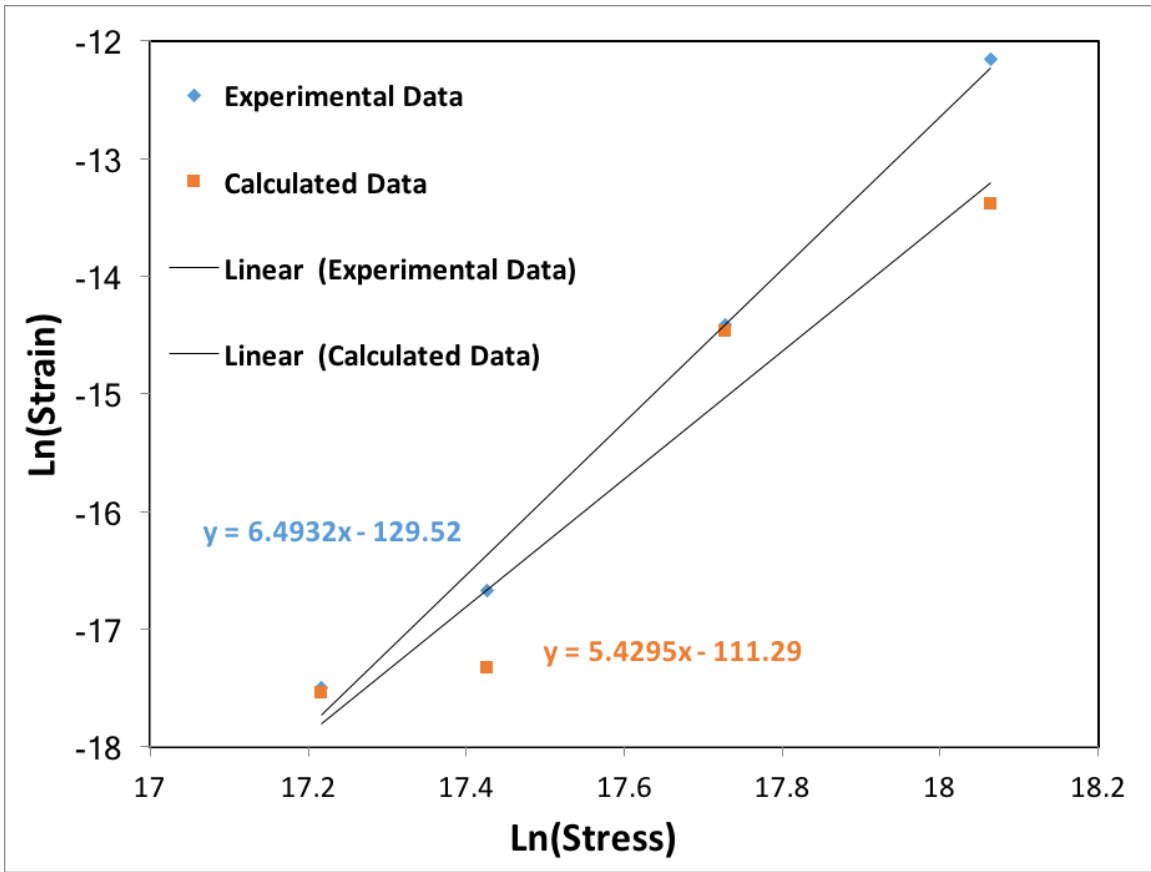


Figure 39. The comparison between the experimental data and calculated data for both four applied stresses. The data points at 30 MPa fits the most, majorly due to at 30 MPa, almost the whole creep process is dominated by diffusional creep, but this diffusional creep rate cannot be doubled when the applied stress goes to 37 MPa. Data point at 50 MPa also fit relatively well, but at 70 MPa the discrepancy on creep rate is roughly 2 times.

higher. In order to solve this issue, either an appropriate shearing mechanism equation should be employed, which is better scaled with the creep strain, or another fitting process assisted with CS techniques needs to be done, in order to find out the best fitting parameters in a much wider range of parameters.

Discussion on Creep

The creep of FBB13 + 3.5 wt.% W alloy shows a banal creep property, both in experiments and in calculations, majorly due to lack of larger and more stable particles. The major strengthener B2-NiAl in this alloy system is too small, too easy to cut it through, therefore it cannot provide enough strength to the alloy. In order to improve the creep resistance of the FBB13 + 3.5 wt.% W alloy, it is better to increase the amount of Ni and slightly decrease the amount of W added in the alloy system, in order to increase the volume fraction and particle size of the B2-NiAl, and reduce the coarsening rate of the Laves phase particles. For the modeling of the creep of FBB13 + 3.5 wt.% W alloy, apparently a proper equation for shearing mechanism is required for coherent particles. Another issue for current model is the capability of the fitting process, it requires a better fitting code in order to search the best fitting in a much wider range. Current fitting needs to consider (1) the initial strain rate, which is related to the parameter A and the initial dislocation density, (2) the parameter C , which is related to the inter-particle spacing and the total stress, and (3) the dislocation density evolution. In the optimization process it is found that the ratio of C to A needs to be at least 60, in order to obtain creep rate that fits better with the experimental results at different applied stresses. On the other hand, the value of A cannot be too small, otherwise it needs to be compensated with higher initial dislocation density, in order to fit well with the initial creep strain

rate. Also the range of the dislocation density evolution is limited, otherwise the total stress could become negative if the dislocation density goes too high. With the above limitation, the acceptable parameters are not much, and the current best fit cannot fit better than the results shown above, indicating either this is already the best result, or there's other possible combination of parameters that requires a better method to discover.

CHAPTER SEVEN

CONCLUSIONS AND RECOMMENDATIONS

Novel ferritic alloys FBB8 + 2 wt.% Hf, FBB8 + 2 wt.% Zr, and FBB13 + 3.5 wt.% W alloys are developed and investigated, in order to introduce additional particles to further strengthen the current alloy FBB8. The results show that although they possess two or more kinds of precipitates, the major strengthener is still B2-NiAl, other types of particles either have too low volume fraction, or are too large to provide enough strengthening effect. Results reveal that volume fraction of secondary phases is a factor that is proportional to the particle size. That is to say, if the volume fraction of certain phase goes higher, its particle size goes larger too. Therefore, in order to obtain the optimized strengthening effect, the amount of the additive elements needed to be carefully adjusted, in order to reach a balance between volume fraction and particle size.

The calculation for the strength of the alloys supports the microstructural discoveries from the FBB8 + 2 wt.% Hf, FBB8 + 2 wt.% Zr, and FBB13 + 3.5 wt.% W alloys, where the FBB13 + 3.5 wt.% W alloy has the worst strength among these three alloys. The FBB8 + 2 wt.% Zr alloy however, has the best strength, which is different with the calculation results. The reason of the discrepancy might due to the error of the measurement on the actual number of the volume fraction and/or particle size.

The creep results as well as the modeling for the FBB13 + 3.5 wt.% W alloy shows that the extremely small B2-NiAl particles leads to the major discrepancy of the experimental data and the modeling results, where the actual creep rate is much faster than the modeling results. The major reason for such an inaccurate prediction majorly lies on the fact of utilizing wrong strengthening mechanism, where for extremely small and coherent particles, the shearing mechanism should be

employed instead of Orowan bowing mechanism. However, current shearing mechanism lacks an equation scaling with creep strain, which instead causes the initial back stress much higher than it supposes to be. In order to improve the fitting of the model and the experimental data, either an appropriate equation describing the shearing mechanism is required, or a better fitting method should be developed.

For the future development of current work, first of all an optimization on FBB13 + 3.5 wt.% W alloy could be done by carefully adjusting the amount of Ni, Al, and W, in order to balance the precipitate size and volume fraction. From current composition, the Ni content can be doubled or even more, in order to obtain B2-NiAl with average particle size ~ 80 nm. For the incoherent particles since their nature of fast coarsening rate, their respective volume fraction is the major factor to control in order to maintain a proper particle size. Therefore, the W content can be halved or even more from current composition. Also, following the above concept, further strengthening of FBB8 series alloy need to consider adding more types of precipitates, since each of incoherent phase cannot have high volume fraction, it can be replaced by a summation of several different incoherent phases.

For the development of the current model, a better fitting process can be developed, in order to search for the best fitting parameters in a much wider range. Such an approach requires techniques from computer science profession, however, is possible to achieve and is able to provide more detail verification on numerical results.

LIST OF REFERENCES

- [1] Meetham, G. W. High-temperature materials- a general review. *Journal of Material Science*, 26 (1991), 853-860.
- [2] Voorde, M. H. Van de. High-temperature materials and industrial applications. *Bull. Soc. Cat. Cien.*, 11 (1991), 199-226.
- [3] J. Skrzypek, A.W. Ganczarski, F. Rustichelli, H. Egner. *Advanced Materials and Structures for Extreme Operating Conditions*. Springer-Verlag Berlin Heidelberg, 2008.
- [4] Strengthening of metal alloys. In Mouritz, A. P., ed., *Introduction to Aerospace Materials*. Woodhead Publishing Limited., 2012.
- [5] Gladman, T. Precipitation hardening in metals. *Materials Science and Technology*, 15 (1999), 30-36.
- [6] Wouters, O. Dislocations and Precipitation Hardening. In *Plasticity in Aluminum Alloys at Various Length Scales*. University of Groningen, 2006.
- [7] Z. Sun, C.H. Liebscher, S. Huang, Z. Teng, G. Song, G. Wang, M. Asta, M. Rawlings, M.E. Fine, P.K. Liaw. New design aspects of creep-resistant NiAl-strengthened ferritic alloys. *Scripta Materialia*, 68 (2013), 384-388.
- [8] Z. Sun, G. Song, J. Ilavsky, G. Ghosh, P. K. Liaw. Nano-sized precipitate stability and its controlling factors in a NiAl-strengthened ferritic alloy. *Scientific Report*, 5 (2015), 16081.
- [9] Z. Sun, G. Song, J. Ilavsky, P. K. Liaw. Duplex Precipitates and Their Effects on the Room-temperature Fracture Behaviour of a NiAl- Strengthened Ferritic Alloy. *Materials Research Letters*, 3 (2015), 128-134.

- [10] Z. Sun, G. Song, T. A. Sisneros, B. Clausen, C. Pu, L. Li, Y. Gao, P. K. Liaw. Load partitioning between the bcc-iron matrix and NiAl-type precipitates in a ferritic alloy on multiple length scales. *Scientific Report*, 6 (2016), 23137.
- [11] G. Song, Z. Sun, L. Li, X. Xu, M. Rawlings, C. H. Liebscher, B. Clausen, J. Poplawsky, D. N. Leonard, S. Huang, Z. Teng, C. T. Liu, M. D. Asta, Y. Gao, D. C. Dunand, G. Ghosh, M. Chen, M. E. Fine, P. K. Liaw. Ferritic Alloys with Extreme Creep Resistance via Coherent Hierarchical Precipitates. *Scientific Report*, 5 (2015), 16327.
- [12] G. Song, Z. Sun, J. D. Poplawsky, Y. Gao, P. K. Liaw. Microstructural evolution of single Ni₂TiAl or hierarchical NiAl/Ni₂TiAl precipitates in Fe-Ni-Al-Cr-Ti ferritic alloys during thermal treatment for elevated-temperature applications. *Acta Materialia*, 127 (2017), 1-16.
- [13] G. Song, Z. Sun, L. Li, B. Clausen, S. Y. Zhang, Y. Gao, P. K. Liaw. High Temperature Deformation Mechanism in Hierarchical and Single Precipitate Strengthened Ferritic Alloys by In Situ Neutron Diffraction Studies. *Scientific Report*, 7 (2017), 45965.
- [14] G. Song, Z. Sun, B. Clausen, P. K. Liaw. Microstructural characteristics of a Ni₂TiAl-precipitate-strengthened ferritic alloy. *Journal of Alloys and Compounds*, 693 (2017), 921-928.
- [15] G. Song, Z. Sun, J. D. Poplawsky, X. Xu, M. Chen, P. K. Liaw. Primary and secondary precipitates in a hierarchical-precipitate-strengthened ferritic alloy. *Journal of Alloys and Compounds*, 706 (2017), 584-588.

- [16] S. I. Baik, S. Y. Wang, P. K. Liaw, D. C. Dunand. Increasing the creep resistance of Fe-Ni-Al-Cr superalloys via Ti additions by optimizing the B2/L21 ratio in composite nano-precipitates. *Acta Materialia*, 157 (2018), 142-154.
- [17] J. Jung, G. Ghosh, D. Isheim, G. B. Olson. Precipitation of Heusler Phase (Ni₂TiAl) from B2-TiNi in Ni-Ti-Al and Ni-Ti-Al-X (X = Hf, Zr) Alloys. *Metallurgical and Materials Transactions A*, 34A (2003), 1221-1235.
- [18] J. Jung, G. Ghosh, G. B. Olson. A comparative study of precipitation behavior of Heusler phase (Ni₂TiAl) from B2-TiNi in Ni-Ti-Al and Ni-Ti-Al-X (X = Hf, Pd, Pt, Zr) alloys. *Acta Materialia*, 51 (2003), 6341-6357.
- [19] L. Sheng, F. Yang, T. Xi, Y. Zheng, J. Guo. Microstructure and room temperature mechanical properties of NiAl-Cr(Mo)-(Hf, Dy) hypoeutectic alloy prepared by injection casting. *Trans. Nonferrous Met. Soc. China*, 23 (2013), 983-990.
- [20] C. Cui, J. Guo, Y. Qi, H. Ye. Effect of Hf on Microstructure and High-Temperature Strength of a Cast NiAl/Cr(Mo) Alloy. *Materials Transactions*, 42, 8 (2001), 1700-1704.
- [21] Y. X. Chen, C. Y. Cui, Z. Q. Liu, L. L. He, J. T. Guo, D. X. Li. Microstructure and phase stability studies on Heusler phase Ni₂AlHf and G-phase Ni₁₆Hf₆Si₇ in directionally solidified NiAl-Cr(Mo) eutectic alloyed with Hf. *Journal of Materials Research*, 15, 6 (2011), 1261-1270.

- [22] S. I. Baik, M. J. S. Rawlings, D. C. Dunand. Effect of hafnium micro-addition on precipitate microstructure and creep properties of a Fe-Ni-Al-Cr-Ti ferritic superalloy. *Acta Materialia*, 153 (2018), 126-135.
- [23] N. E. Prasad, R. J. H. Wanhill, ed. *Aerospace Materials and Material Technologies*. Springer Singapore, 2017.
- [24] L. Sun, T. H. Simm, T. L. Martin, S. McAdam, D. R. Galvin, K. M. Perkins, P. A. J. Bagot, M. P. Moody, S. W. Ooi, P. Hill, M. J. Rawson, and H. K. D. H. Bhadeshia. A novel ultra-high strength maraging steel with balanced ductility and creep resistance achieved by nanoscale δ -NiAl and Laves phase precipitates. *Acta Materialia*, 149 (2018), 285-301.
- [25] Goldbeck, O. Kubaschewski von. *IRON—Binary Phase Diagrams*. Springer-Verlag Berlin Heidelberg, 1982.
- [26] S. Kobayashi, and T. Hibiru. Formation of the Fe₂Hf Laves Phase Along the Eutectoid-type Reaction Path of δ -Fe \rightarrow γ -Fe+Fe₂Hf in an Fe-9Cr Based Alloy. *ISIJ International*, 55 (2015), 293-299.
- [27] S. Kobayashi, K. Kimura, and K. Tsuzaki. Interphase precipitation of Fe₂Hf Laves phase in a Fe₉Cr/Fe₉CrHf diffusion couple. *Intermetallics*, 46 (2014), 80-84.
- [28] K. J. Lee, P. Nash. The Al-Hf-Ni System (Aluminum-Hafnium-Nickel). *Journal of Phase Equilibria*, 12 (1991), 94-104.
- [29] D. P. Abraham, J. W. Richardson Jr., S. M. McDeavitt. Formation of the Fe₂₃Zr₆ phase in an Fe-Zr alloy. *Scripta Materialia*, 37, 2 (1997), 239-244.

- [30] P. Nash, Y. Y. Pan. The Al-Ni-Zr System (Aluminum-Nickel-Zirconium). *Journal of Phase Equilibria*, 12 (1991), 105-113.
- [31] A. M. Wusatowska-Sarnek, H. Miura, T. Sakai. Coherency strains influence on martensitic transformation of γ -Fe particles in compressed Cu-Fe alloy single crystals. *Journal of Materials Science*, 34 (1999), 5477-5487.
- [32] V. Rigaud, D. Daloz, G. Lesoult. Influence of Ti and Zr additions on solidification of Fe base intermetallics precipitating Laves phase. *International Journal of Cast Metals Research*, 22 (2009), 47-50.
- [33] S. Onurlu, A. Tekin. Effect of heat treatment on the insoluble intermetallic phases present in an AA 6063 alloy. *Journal of Materials Science*, 29 (1994), 1652-1655.
- [34] J. Fu, D. Yang, K. Wang. Correlation between the Liquid Fraction, Microstructure and Tensile Behaviors of 7075 Aluminum Alloy Processed by Recrystallization and Partial Remelting (RAP). *Metals*, 8 (2018), 508.
- [35] Z.B. Jiao, J.H. Luan, Z.W. Zhang, M.K. Miller, C.T. Liu. High-strength steels hardened mainly by nanoscale NiAl precipitates. *Scripta Materialia*, 87 (2014), 45-48.
- [36] E. Povoden-Karadeniz, E. Kozeschnik. Simulation of Precipitation Kinetics and Precipitation Strengthening of B2-precipitates in Martensitic PH 13–8 Mo Steel. *ISIJ International*, 52, 4 (2012), 610-615.
- [37] J. Kucera, K. Stransk. Diffusion in Iron, Iron Solid Solutions and Steels. *Material Science and Engineering*, 52 (1982), 1-38.

- [38] G. Ghosh, G. B. Olson. The isotropic shear modulus of multicomponent Fe-base solid solutions. *Acta Materialia*, 50 (2002), 2655-2675.
- [39] Ardell, A.J. Precipitation hardening. *Metallurgical Transactions A*, 16, 12 (1985), 2131-2165.
- [40] R.G. Campany, M.H. Loretto, and R.E. Smallman. The determination of the $1/2 \langle 111 \rangle \{ 110 \}$ antiphase boundary energy of NiAl. *Journal of Microscopy*, 98, 2 (1973), 174-179.
- [41] A. Deschamps, M. Militzer, and W.J. Poole. Precipitation Kinetics and Strengthening of a Fe-0.8wt%Cu Alloy. *ISIJ International*, 41 (2001), 196-205.
- [42] R.D. Noebe, R.R. Bowman, and M.V. Nathal. Physical and mechanical properties of the B2 compound NiAl. *International Materials Reviews*, 38, 4 (1993), 193-232.
- [43] K.C. Russell, and L.M. Brown. A dispersion strengthening model based on differing elastic moduli applied to the iron-copper system. *Acta Metallurgica*, 20, 7 (1972), 969-974.
- [44] K. Ma, H. Wen, T. Hu, T.D. Topping, D. Isheim, D.N. Seidman, E.J. Lavernia, and J.M. Schoenung. Mechanical behavior and strengthening mechanisms in ultrafine grain precipitation-strengthened aluminum alloy. *Acta Materialia*, 62 (2014), 141-155.
- [45] C. Shen, V. Gupta, S. Huang, M. Soare, P. Zhao, and Y. Wang. *Modeling Long-term Creep Performance for Welded Nickel-base Superalloy Structures for Power Generation Systems*. GE Global Research, 2017.

- [46] Weertman, J. Steady-State Creep through Dislocation Climb. *Journal of Applied Physics*, 28, 3 (1957), 362-364.
- [47] Dyson, B.F. Microstructure based creep constitutive model for precipitation strengthened alloys theory and application. *Materials Science and Technology*, 25, 2 (2009), 213-220.
- [48] J.A. Rayne, and B.S. Chandrasekhar. Elastic constants of iron from 4.2 to 300°K. *Physical Review*, 122 (1961), 1714-1716.
- [49] Reed, R.C. *The Superalloys, Fundamentals and Applications*. Cambridge University Press, 2006.
- [50] Dyson, B.F. Creep and fracture of metals : mechanisms and mechanics. *Revue de Physique Appliquee*, 23 (1988), 605-613.
- [51] M. McLean, and B.F. Dyson. Modeling the effects of damage and microstructural evolution on the creep behavior of engineering alloys. *Journal of Engineering Materials and Technology*, 122, 3 (2000), 273-278.
- [52] Smith, M.T. *High-Temperature Aluminum Alloys*. Pacific Northwest National Laboratory, 2012.
- [53] V.C. Igwemezie, C.C. Ugwuegbu, and U. Mark. Physical Metallurgy of Modern Creep-Resistant Steel for Steam Power Plants: Microstructure and Phase Transformations. *Journal of Metallurgy* (2017), 5468292.
- [54] 12-Superalloys for gas turbine engines. In Mouritz, A.P., ed., *Introduction to Aerospace Materials*. Woodhead Publishing, 2012.

- [55] Stainless Steel at MetalMiner (<https://agmetalminer.com/metal-prices/stainless-steel/>)
- [56] Nickel Alloy at MetalMiner (<https://agmetalminer.com/metal-prices/nickel-alloy/>)
- [57] N.Q. Vo, C.H. Liebscher, M.J. Rawlings, M. Asta, and D.C. Dunand. Creep properties and microstructure of a precipitation-strengthened ferritic Fe–Al–Ni–Cr alloy. *Acta Materialia*, 71 (2014), 89-99.
- [58] Z.K. Teng, M.K. Miller, G. Ghosh, C.T. Liu, S. Huang, K.F. Russell, M.E. Fine, and P.K. Liaw. Characterization of nanoscale NiAl-type precipitates in a ferritic steel by electron microscopy and atom probe tomography. *Scripta Materialia*, 63 (2010), 61-64.
- [59] Z.K. Teng, C.T. Liu, G. Ghosh, P.K. Liaw, and M.E. Fine. Effects of Al on the microstructure and ductility of NiAl-strengthened ferritic steels at room temperature. *Intermetallics*, 18, 8 (2010), 1437-1443.
- [60] Z.K. Teng, F. Zhang, M.K. Miller, C.T. Liu, S. Huang, Y.T. Chou, R.H. Tien, Y.A. Chang, and P.K. Liaw. New NiAl-strengthened ferritic steels with balanced creep resistance and ductility designed by coupling thermodynamic calculations with focused experiments. *Intermetallics*, 29 (2012), 110-115.
- [61] Z.K. Teng, C.T. Liu, M.K. Miller, G. Ghosh, E.A. Kenik, S. Huang, and P.K. Liaw. Room temperature ductility of NiAl-strengthened ferritic steels: Effects of precipitate microstructure. *Materials Science and Engineering: A*, 541 (2012), 22-27.
- [62] Z.K. Teng, F. Zhang, M.K. Miller, C.T. Liu, S. Huang, Y.T. Chou, R.H. Tien, Y.A. Chang, and P.K. Liaw. Thermodynamic modeling and experimental validation of the Fe-Al-Ni-Cr-Mo alloy system. *Materials Letters*, 71 (2012), 36-40.

- [63] Z.K. Teng, G. Ghosh, M.K. Miller, S. Huang, B. Clausen, D.W. Brown, and P.K. Liaw. Neutron study and modeling of the lattice parameters in a NiAl-precipitate strengthened ferritic steel. *Acta Materialia*, 60, 13-14 (2012), 5362-5369.
- [64] Z.K. Teng, F. Zhang, M.K. Miller, C.T. Liu, S. Huang, Y. Chou, R. Tien, Y.A. Chang, P.K. Liaw. New Ferritic Steels with Combined Optimal Creep Resistance and Ductility by Coupling Thermodynamic Calculations with Focused Experiments. *Intermetallics*, 29, 10 (2012).
- [65] S. Huang, Y. Gao, K. An, L. Zheng, W. Wu, Z.K. Teng, and P.K. Liaw. Deformation mechanisms in a precipitation-strengthened ferritic superalloy revealed by in situ neutron diffraction studies at elevated temperatures. *Acta Materialia*, 83 (2015), 137-148.
- [66] S. Huang, D.W. Brown, B. Clausen, Z.K. Teng, Y. Gao, and P.K. Liaw. In situ neutron-diffraction studies on the creep behavior of a ferritic superalloy. *Metallurgical and Materials Transactions A*, 43, 5 (2012), 1497-1508.
- [67] S. Huang, G. Ghosh, X. Li, J. Ilavsky, Z.K. Teng, and P.K. Liaw. Effect of Al on the NiAl-Type B2 Precipitates in Ferritic Superalloys. *Metallurgical and Materials Transactions A*, 43, 10 (2012), 3423–3427.
- [68] W. Yan, W. Wang, Y. Shan, K. Yang, W. Sha. *9-12Cr Heat-Resistant Steels*. Springer International Publishing, 2015.

- [69] M.A. Muñoz-Morris, N. Calderon, and D.G. Morris. Coarsening kinetics of metastable nanoprecipitates in a Fe–Ni–Al alloy. *Journal of Materials Science*, 43, 10 (2008), 3674–3682.
- [70] H. Calderon, M. Fine, and J. Weertman. Coarsening and morphology of β' particles in Fe-Ni-Al-Mo ferritic alloys. *Metallurgical Transactions A*, 19, 5 (1988), 1135-1146.
- [71] H. Calderon, J. Weertman, M. Fine. Effect of cyclic plastic deformation on elevated temperature Ostwald ripening of an alloy with coherent precipitates. *Scripta Metallurgica*, 18 (1984), 587.
- [72] H.J. Frost, M.F. Ashby. *Deformation-mechanism maps: the plasticity and creep of metals and ceramics*. Pergamon Press, 1982.

APPENDIX

Introduction

The constitutive creep model was developed by C. Shen et al. in GE Global Research, in order to model the creep deformation of Ni-based superalloy NIMONIC 105 [45]. Please refer the report for the most detailed introduction of this model, here a brief introduction on the model and how does it work will be addressed, as well as all the parameters that has been employed. The model itself is a damage model, which means the deformation is influenced by the evolution of cavities/sample damage. Within this model there are majorly two basic mechanisms that are included, which are dislocation-related mechanism (which is stress dependent) and diffusion-related (which is temperature dependent), and both mechanisms contribute to the deformation of the sample itself, as well as the cavity growth. The general concept of this model is to re-calculate rate equations (including strain rates and damage evolution rates from every mechanisms) and microstructural parameters such as particle size, dislocation density...etc. for every time interval. The simultaneous rate times the time interval result in the simultaneous strain or damage, and then the accumulated strain and damage in a specific time can be obtained. In this research, the time interval is 60 seconds, which means all the parameters like strain rate, particle size, dislocation density...etc. will be updated every 60 seconds, and for every 60 seconds a latest parameter will be updated. Later in the next paragraph the equations that are employed will be introduced.

Equations

As mentioned above, this model includes both dislocation-related mechanism and diffusion-related mechanism, that is to say, the creep strain is contributed by both dislocation component and diffusion component. Therefore, it can be described as:

$$\varepsilon_{creep} = \varepsilon_{disloc} + \varepsilon_{diffusion} \quad (25)$$

The dislocation component is determined by the dislocation-related strain rate, which is proposed by Dyson et al. as a hyperbolic sine form, shown as:

$$\dot{\varepsilon} = \begin{cases} \rho A D_V f (1 - f) \left(\sqrt{\frac{\pi}{4f}} - 1 \right) \sinh \left(C \frac{\sigma_{eff} - \sigma_B - \sigma_0}{MkT} b^2 \lambda \right), & \text{if } \sigma_{eff} - \sigma_B - \sigma_0 > 0 \\ 0, & \text{otherwise} \end{cases} \quad (26)$$

Where A and C are constants, ρ is the density of dislocations, which can be measured by TEM or neutron/synchrotron diffraction. D_V is the volume diffusivity of the matrix, k is the Boltzmann constant $1.38 \times 10^{-23} \text{ J/K}$, and λ is the average inter-particle spacing. In this equation there are three stress terms, which are the effective stress σ_{eff} , back stress σ_B , and stress caused by the interaction of the dislocations σ_0 . The effective stress is described as:

$$\sigma_{eff} = \sigma_{app} \frac{1 + \varepsilon_{creep}}{1 - \omega} \quad (27)$$

Where σ_{app} is the applied stress, and ω is damage parameter, which is an expression of the overall damage of the sample. The back stress σ_B is an expression of the stress contributed by precipitates, which could be either from a shearing mechanism or a climbing mechanism, depending on which one is weaker, therefore:

$$\sigma_B = \min(\sigma_{shear}, \sigma_{climb}) \quad (28)$$

And:

$$\sigma_{shear} = \frac{\gamma_{APB}}{2b} \left[\left(\frac{12\gamma_{APB}fr}{\pi Gb^2} \right)^{\frac{1}{2}} - f \right] \quad (29)$$

$$\sigma_{climb} = \frac{2f}{1+2f} \sigma_{eff} \left[1 - \exp \left(- \frac{1+2f}{2(1-f)} E \frac{\varepsilon_{disloc}}{\sigma_{eff}} \right) \right] \quad (30)$$

Where f is the volume fraction of the precipitate, r is the radius of the precipitate, γ_{APB} is the anti-phase boundary energy of the precipitate, and E is the elastic modulus. The stress caused by the interaction of the dislocations σ_0 is described as:

$$\sigma_0 = 0.25Mgb\sqrt{\rho} \quad (31)$$

Where ρ is dislocation density, and the dislocation density can be assumed by:

$$\rho = \rho_i + \rho_f \frac{\varepsilon_{creep}}{\varepsilon_{crit}} \quad (32)$$

Where ρ_i and ρ_f refers to the initial and the final dislocation densities respectively, and the ε_{crit} is the critical strain, which is 0.2 in this research, since the creep test on FBB13 + 3.5 wt.% W alloy at 70 MPa is fractured at ~0.2 strain.

The dislocation also contributes to the growth of cavities in a simple way, which is described as:

$$\dot{\omega}_{disloc} = D\dot{\varepsilon}_{disloc} \quad (33)$$

Where the cavity growth rate contributed from the dislocation has a simple linear dependence on dislocation creep strain rate.

For the diffusion component, the diffusion creep strain rate can be contributed from four sources, two of them are direct deformation on the sample, which are lattice diffusion and grain boundary

diffusion, and two of them are related to the cavities, which are grain boundary diffusion and surface diffusion. The lattice diffusion rate contributed directly to the deformation can be described as:

$$\dot{\epsilon}_{lattice_diff} = \xi\beta\sigma_{app}(1 + \epsilon_{creep}) \quad (34)$$

And the grain boundary diffusion rate contributed directly to the deformation can be described as:

$$\dot{\epsilon}_{boundary_diff} = 3\pi\xi\left(\frac{l}{d}\right)^3\sigma_{app}(1 + \epsilon_{creep}) \quad (35)$$

Where $\beta = \frac{3D_V}{D_B\delta_B}\frac{l^3}{d^2}$, $\xi = F\frac{D_B\delta_B}{d^3}\left(\frac{l}{d}\right)^3$, l is the void size and d is grain size.

For the diffusion contributes to cavity growth via grain boundary diffusion and surface diffusion, the strain rate can be described as:

$$\dot{\epsilon}_{cav_boundary_diff} = \xi\frac{l}{d}\frac{\sigma_{app}}{\ln(1/\omega_{boundary_diff})} \quad (36)$$

And:

$$\dot{\epsilon}_{cav_surface_diff} = \xi\alpha\frac{\sqrt{\omega_{surface_diff}}\sigma_{app}^2}{(1 - \omega_{surface_diff})^3} \quad (37)$$

Where $\alpha = \frac{D_S\delta_S}{D_B\delta_B}\frac{1}{\sqrt{2}}\frac{l^2}{d\gamma}$, and γ is surface energy.

The damage/cavity grows via two different sources, dislocation and diffusion, the damage contributed from dislocation has shown in Eq. (33). The damage contributed from diffusion are majorly from grain boundary diffusion and surface diffusion, which had shown in Eq. (36) and Eq. (37) as $\omega_{boundary_diff}$ and $\omega_{surface_diff}$. The rate for the damage growth are described as:

$$\dot{\omega}_{boundary_diff} = \frac{\xi}{2} \frac{\sigma_{app}(1 + \varepsilon_{creep})}{\sqrt{\omega_{boundary_diff}} \ln(1/\omega_{boundary_diff})} \quad (38)$$

And:

$$\dot{\omega}_{surface_diff} = \frac{\xi \alpha d}{4 \gamma} \frac{\sqrt{\omega_{surface_diff}} [\sigma_{app}(1 + \varepsilon_{creep})]^3}{(1 - \omega_{surface_diff})^3} \quad (39)$$

And the total damage is $\omega = \omega_{disloc} + \omega_{diff}$.

As described earlier, the instantaneous strain ε and damage ω are calculated from the strain rate $\dot{\varepsilon}$ and damage/cavity growth rate $\dot{\omega}$, and the accumulated strain and damage are the summation of the instantaneous strain and damage for each time node. As a result, many of the rate equation have the dependence on their accumulated value, and the whole simulation is basically a repeated calculation on the instantaneous rate and accumulated value, until certain circumstance has achieved. Figure 40 shows a flow chart illustrating the general concept of the model, and Table 12 shows all the parameters and the correspond values employed within this research.

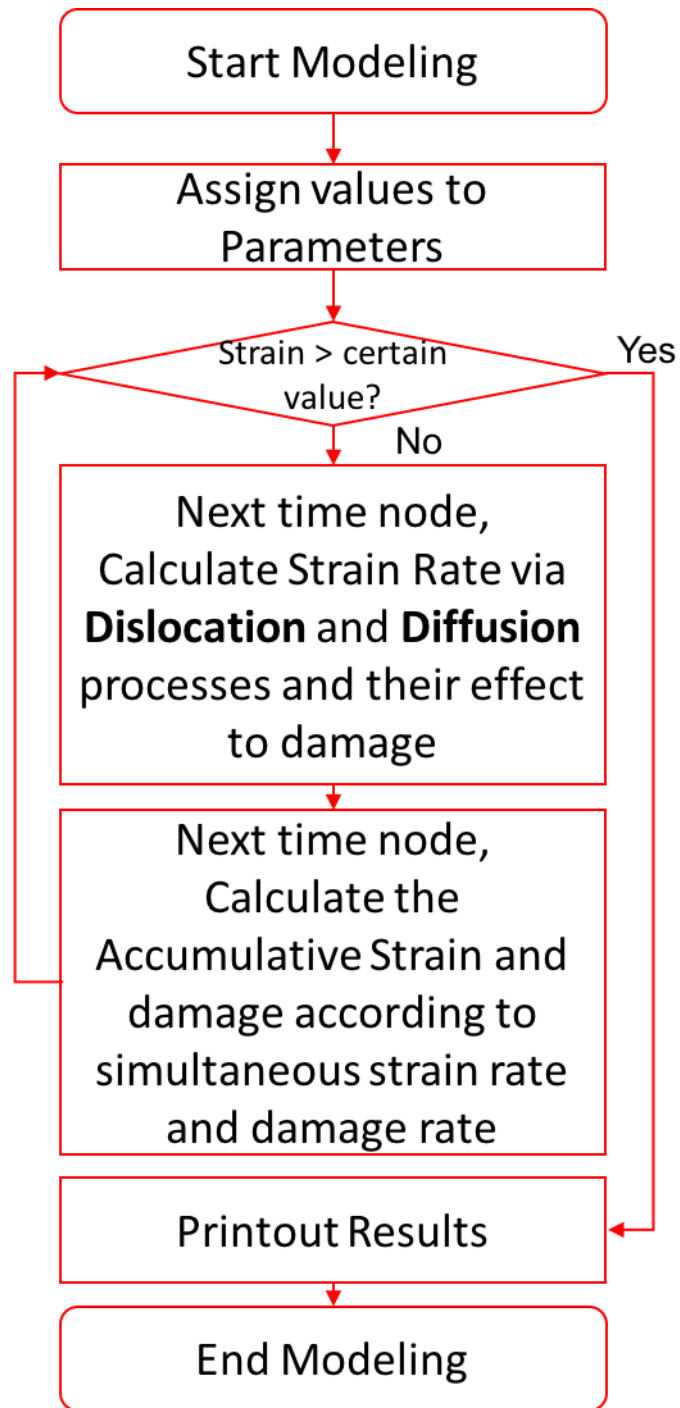


Figure 40. Flow chart of the constitutive creep model.

Table 12. Parameters and their values for FBB13 + 3.5 wt.% W alloy

Parameter	Symbol	Value	Source
Average grain size	d	0.0002 m	Measured
Void diameter/grain diameter ratio	$\frac{l}{d}$	0.1	Estimated
Taylor factor	M	2.9	Typical for BCC metal
Surface energy	γ	2 J/m^2	Estimated
Anti-phase boundary energy	γ_{APB}	0.2 J/m^2	[35, 36, 40]
Shear modulus	G	57 GPa	[38, 48]
Young's modulus	E	148.2 GPa	Converted from shear modulus
Poisson's ratio	ν	0.3	Estimated
Burger's vector	b	2.5 nm	For ferrite matrix
Bulk diffusion coefficient	D_v	$2 \times 10^{-4} \exp\left(\frac{-251 \text{ kJ}}{RT \text{ mol}}\right) m^2/s$	[72]
Grain boundary diffusion coefficient	D_b	$1.1 \times 10^{-11} \exp\left(\frac{-174 \text{ kJ}}{RT \text{ mol}}\right) m^2/s$	[72]
Creep strain rate coefficient	A	0.03	Fitted
Creep strain rate parameter	C	1.2	Fitted
Damage evolution parameter	D	2	Fitted
Creep diffusion parameter	F	0.4	Fitted

Script

The script for the modeling using Excel VBA is presented in the following paragraph:

Option Explicit

Sub creep_rate()

'TF = Taylor Factor

'SE = Surface energy

'APBE = Anti-phase boundary energy

'ave_gs = Average grain size

'VD = Void diameter

'SM = Shear modulus

'YM = Young's modulus

'DD = Dislocation density

'PVF = Precipitate volume fraction

'PS = Precipitate average size

'Psp = Inter-precipitate spacing

'PR = Poisson ratio

'BV = Burger's vector

'Sigma_app = Applied stress (MPa)

'Sigma_eff = Effective stress (MPa)

'UTS = ultimate tensile strength (MPa)

Dim TF, SE, APBE, ave_gs, VD, SM, YM, DDf, DDi, PVF_0, PVF_1, PVF_2, PSf_0, PSf_1, PSf_2, Psi_0, Psi_1, Psi_2, Psp, PR, BV, A, B, C, D, F, Xi, alpha, ave_dia_void, Pi, shear, climb
As Double

Dim Sigma_app, Sigma_eff, sigma_b_0, sigma_b_1, sigma_b_2, sigma_0, UTS, E_creep_r, E_creep, E_disl_r, E_disl, E_diff_r, E_diff, E_bd_r, E_sd_r, E_vo_r, E_bo_r As Double

Dim omega, omega_diff, omega_diff_r, omega_disl, omega_disl_r, omega_bd, omega_bd_r, omega_sd, omega_sd_r As Double

Dim Ds, delta_s, Db, delta_b, Dv As Double

Dim E_creep_p(1 To 5000), E_creep_r_p(1 To 5000), E_disl_r_p(1 To 5000), E_diff_r_p(1 To 5000), omega_p(1 To 5000), stress_eff_p(1 To 5000), stress_p(1 To 5000), stress_b0_p(1 To 5000), stress_b1_p(1 To 5000), stress_b2_p(1 To 5000), stress_disl_p(1 To 5000), size_0_p(1 To 5000), size_1_p(1 To 5000), size_2_p(1 To 5000), Psp_p(1 To 5000) As Double

Dim i, t As Double

Dim temp As Double

TF = 2.9

SE = 2

APBE = 0.2

ave_gs = 0.0002

ave_dia_void = 2E-05

$$VD = 1E-08$$

$$SM = 57000000000\#$$

$$YM = SM * 2 * (1 + 0.3)$$

$$DDi = 6800000000000\#$$

$$PVF_0 = 0.13$$

$$PVF_1 = 0$$

$$PVF_2 = 0.01$$

$$PR = 0.3$$

$$BV = 2.5E-10$$

$$A = 0.03$$

$$C = 1.2$$

$$D = 2$$

$$F = 0.4$$

$$t = 0$$

$$Pi = 3.1415926$$

'Diffusion coefficients=====

$$Dv = 0.0002 * \text{Exp}(-251000 / (8.314 * 973))$$

$$Db = 1.1E-12 * \text{Exp}(-174000 / (8.314 * 973))$$

$$\text{delta}_b = 1E-09$$

$$Ds = Db$$

delta_s = 1E-09

'=====

UTS = 10000000000#

Sigma_app = 70000000#

alpha = Ds * delta_s / (Db * delta_b) * (1 / (2 ^ 0.5)) * (ave_dia_void ^ 2) / (ave_gs * SE)

Xi = F * 4 * Db * delta_b / (ave_gs ^ 3) * ((ave_dia_void / ave_gs) ^ 3)

omega_bd = 0.001

omega_sd = 0

omega = 0.001

E_creep = 0

E_disl = 0

E_diff = 0

'Calculating evolution=====

'Do While Sigma_eff <= UTS And E_creep_r < 10 ^ -4

Do While Sigma_eff <= UTS And E_creep < 0.2

t = t + 60

'Dynamic Dislocation Density_v1=====

DDf = DDi + 6 * 6800000000000# * (E_creep / 0.2)

Psi_0 = 2E-08 * 1000000000#

PSf_0 = ((Psi_0 ^ 3 + 3.84E+15 * Exp(-270000 / (8.314 * 973)) * t) ^ (1 / 3)) * 1E-09

Psi_1 = 1E-07 * 1000000000#

$$PSf_1 = ((Psi_1 \wedge 3 + 3.84E+15 * \text{Exp}(-270000 / (8.314 * 973)) * t) \wedge (1 / 3)) * 1E-09$$

$$Psi_2 = 1.9E-06 * 1000000000\#$$

$$PSf_2 = ((Psi_2 \wedge 3 + 3E+16 * \text{Exp}(-240000 / (8.314 * 973)) * t) \wedge (1 / 3)) * 1E-09$$

$$Psp = 2 * ((1 - PVF_0 - PVF_1 - PVF_2) / ((PVF_0 / ((PSf_0 / 2) \wedge 3)) + (PVF_1 / ((PSf_1 / 2) \wedge 3) + PVF_2 / ((PSf_2 / 2) \wedge 3))) \wedge (1 / 3))$$

$$\text{size_0_p}(t / 60) = PSf_0$$

$$\text{size_1_p}(t / 60) = PSf_1$$

$$\text{size_2_p}(t / 60) = PSf_2$$

$$Psp_p(t / 60) = Psp$$

'=====

'Dislocation part=====

$$\text{sigma_0} = 0.25 * TF * SM * BV * (DDf \wedge 0.5)$$

$$\text{stress_disl_p}(t / 60) = \text{sigma_0}$$

$$\text{Sigma_eff} = \text{Sigma_app} / (1 - \text{omega}) * (1 + E_creep)$$

$$\text{sigma_b_0} = 2 * PVF_0 / (1 + 2 * PVF_0) * \text{Sigma_eff} * (1 - \text{Exp}(-(1 + 2 * PVF_0) / (2 * (1 - PVF_0))) * YM * E_disl / \text{Sigma_eff}))$$

$$\text{sigma_b_1} = 2 * PVF_1 / (1 + 2 * PVF_1) * \text{Sigma_eff} * (1 - \text{Exp}(-(1 + 2 * PVF_1) / (2 * (1 - PVF_1))) * YM * E_disl / \text{Sigma_eff}))$$

$$\text{sigma_b_2} = 2 * PVF_2 / (1 + 2 * PVF_2) * \text{Sigma_eff} * (1 - \text{Exp}(-(1 + 2 * PVF_2) / (2 * (1 - PVF_2))) * YM * E_disl / \text{Sigma_eff}))$$

$$\text{stress_b1_p}(t / 60) = \text{sigma_b_1}$$

$$\text{stress_b2_p}(t / 60) = \text{sigma_b_2}$$

$$\text{stress_b0_p}(t / 60) = \text{sigma_b_0}$$

$$\text{stress_eff_p}(t / 60) = \text{Sigma_eff}$$

If Sigma_eff - sigma_b_0 - sigma_b_1 - sigma_b_2 - sigma_0 > 0 Then

$$\begin{aligned} E_disl_r = & \text{DDf} * \text{A} * \text{Dv} * (\text{PVF}_0 + \text{PVF}_1 + \text{PVF}_2) * (1 - \text{PVF}_0 - \text{PVF}_1 - \text{PVF}_2) * (((\text{Pi} / \\ & 4 / (\text{PVF}_0 + \text{PVF}_1 + \text{PVF}_2)) ^ 0.5) - 1) * ((\text{Exp}(\text{C} * ((\text{Sigma_eff} - \text{sigma_b_0} - \text{sigma_b_1} - \\ & \text{sigma_b_2} - \text{sigma}_0) / (\text{TF} * 1.38\text{E-}23 * 973)) * (\text{BV} ^ 2) * \text{Psp})) + \text{Exp}(-\text{C} * ((\text{Sigma_eff} - \\ & \text{sigma_b_0} - \text{sigma_b_1} - \text{sigma_b_2} - \text{sigma}_0) / (\text{TF} * 1.38\text{E-}23 * 973)) * (\text{BV} ^ 2) * \text{Psp})) / 2 \end{aligned}$$

Else

$$E_disl_r = 0$$

End If

$$\text{stress_p}(t / 60) = \text{Sigma_eff} - \text{sigma_b_0} - \text{sigma_b_1} - \text{sigma_b_2} - \text{sigma}_0$$

$$E_disl = E_disl + E_disl_r * 60$$

$$E_disl_r_p(t / 60) = E_disl_r$$

'Diffusion part'=====

$$E_bo_r = 3 * \text{Pi} * \text{Xi} * ((\text{ave_dia_void} / \text{ave_gs}) ^ 3) * \text{Sigma_app} * (1 + E_creep)$$

$$\begin{aligned} E_vo_r = & \text{Xi} * 3 * \text{Dv} / (\text{Db} * \text{delta_b}) * ((\text{ave_dia_void} ^ 3) / (\text{ave_gs} ^ 2)) * \text{Sigma_app} * (1 + \\ & E_creep) \end{aligned}$$

'Cavity part'=====

$$\text{omega_disl} = \text{omega_disl} + \text{D} * E_disl_r * 60$$

If omega_disl >= 0.99 Then

$\omega_{disl} = 0.99$

End If

$\omega_{bd_r} = \frac{\xi}{2} * \sigma_{app} * (1 + E_{creep}) / (((\omega_{bd})^{0.5}) * \text{Log}(1 / \omega_{bd}))$

$\omega_{bd} = \omega_{bd} + \omega_{bd_r} * 60$

If $\omega_{bd} \geq 0.99$ Then

$\omega_{bd} = 0.99$

End If

$\omega_{sd_r} = \frac{\xi * \alpha}{4} * \frac{ave_{gs}}{SE} * ((\omega_{sd})^{0.5}) * ((\sigma_{app} * (1 + E_{creep}))^{3}) / ((1 - \omega_{sd})^{3})$

$\omega_{sd} = \omega_{sd} + \omega_{sd_r} * 60$

If $\omega_{sd} \geq 0.99$ Then

$\omega_{sd} = 0.99$

End If

$\omega_{diff} = \omega_{bd} + \omega_{sd}$

$\omega = \omega_{diff} + \omega_{disl}$

$\omega_p(t / 60) = \omega$

$E_{bd_r} = \xi * (\frac{ave_{dia_void}}{ave_{gs}}) * \sigma_{app} / (\text{Log}(1 / \omega_{bd}))$

$E_{sd_r} = \xi * \alpha * (\omega_{sd}^{0.5}) * (\sigma_{app}^2) / ((1 - \omega_{sd})^3)$

$E_{diff_r} = E_{bo_r} + E_{vo_r} + E_{bd_r} + E_{sd_r}$

$E_{diff} = E_{diff} + E_{diff_r} * 60$

$E_{diff_r_p}(t / 60) = E_{diff_r}$

$E_{\text{creep}} = E_{\text{disl}} + E_{\text{diff}}$

$E_{\text{creep}_p}(t / 60) = E_{\text{creep}}$

If $t / 60 - 1 = 0$ Then

$E_{\text{creep}_r} = E_{\text{creep}} / 60$

Else

$E_{\text{creep}_r} = (E_{\text{creep}} - E_{\text{creep}_p}(t / 60 - 1)) / 60$

End If

$E_{\text{creep}_r_p}(t / 60) = E_{\text{creep}_r}$

Loop

ActiveWorkbook.Worksheets("Results").Select

ActiveSheet.Cells(1, 1).Value = "No."

ActiveSheet.Cells(1, 2).Value = "Strain"

ActiveSheet.Cells(1, 3).Value = "Strain rate"

ActiveSheet.Cells(1, 4).Value = "Dislocation component"

ActiveSheet.Cells(1, 5).Value = "Diffusion component"

ActiveSheet.Cells(1, 6).Value = "damage variable"

ActiveSheet.Cells(1, 7).Value = "Total Stress"

ActiveSheet.Cells(1, 8).Value = "Back Stress 10 nm B2"

ActiveSheet.Cells(1, 9).Value = "Back Stress 100 nm B2"

ActiveSheet.Cells(1, 10).Value = "Back Stress Laves"

ActiveSheet.Cells(1, 11).Value = "Disl. Stress"

ActiveSheet.Cells(1, 12).Value = "Effective Stress"

ActiveSheet.Cells(1, 13).Value = "B2 Size 1"

ActiveSheet.Cells(1, 14).Value = "B2 Size 2"

ActiveSheet.Cells(1, 15).Value = "Laves Size"

ActiveSheet.Cells(1, 16).Value = "Inter-particle Spacing"

For i = 1 To 5000 Step 1

ActiveSheet.Cells(i + 1, 1).Value = i

ActiveSheet.Cells(i + 1, 2).Value = E_creep_p(i) + 0.017214

ActiveSheet.Cells(i + 1, 3).Value = E_creep_r_p(i)

ActiveSheet.Cells(i + 1, 4).Value = E_disl_r_p(i)

ActiveSheet.Cells(i + 1, 5).Value = E_diff_r_p(i)

ActiveSheet.Cells(i + 1, 6).Value = omega_p(i)

ActiveSheet.Cells(i + 1, 7).Value = stress_p(i)

ActiveSheet.Cells(i + 1, 8).Value = stress_b0_p(i)

ActiveSheet.Cells(i + 1, 9).Value = stress_b1_p(i)

ActiveSheet.Cells(i + 1, 10).Value = stress_b2_p(i)

ActiveSheet.Cells(i + 1, 11).Value = stress_disl_p(i)

ActiveSheet.Cells(i + 1, 12).Value = stress_eff_p(i)

ActiveSheet.Cells(i + 1, 13).Value = size_0_p(i)

ActiveSheet.Cells(i + 1, 14).Value = size_1_p(i)

ActiveSheet.Cells(i + 1, 15).Value = size_2_p(i)

```
ActiveSheet.Cells(i + 1, 16).Value = Psp_p(i)
```

```
Next
```

```
End Sub
```

VITA

Shao-Yu Wang was born and grew up at Taipei, Taiwan (R.O.C) on September 10, 1985. He graduated with a B.S. degree and M.S. degree from the Department of Geosciences at National Taiwan University, Taipei in 2008 and 2011. Later He worked for Taiwan Power Company until May 2013, and then joined the Department of Materials Science and Engineering at The University of Tennessee, Knoxville to start his Ph.D. study on August, 2014. In August 2019, he graduated from the University of Tennessee with Doctor of Philosophy degree in Materials Science & Engineering (concentrated in Metallurgy).